



Finlayson, Ewan David (2007) *Polarisation effects in gallium arsenide optical waveguides*. PhD thesis.

<http://theses.gla.ac.uk/5856/>

Copyright and moral rights for this thesis are retained by the author

A copy can be downloaded for personal non-commercial research or study, without prior permission or charge

This thesis cannot be reproduced or quoted extensively from without first obtaining permission in writing from the Author

The content must not be changed in any way or sold commercially in any format or medium without the formal permission of the Author

When referring to this work, full bibliographic details including the author, title, awarding institution and date of the thesis must be given

# **Polarisation Effects in Gallium Arsenide Optical Waveguides**

**Ewan David Finlayson**  
**March 2007**

A thesis submitted to the Faculty of Engineering of the University of Glasgow for the degree of Doctor of Philosophy.

This thesis is provided in confidence for the purpose of examination for the degree of Doctor of Philosophy. It is not for further disclosure without the written permission of QinetiQ Ltd.

© Ewan David Finlayson, 2007.

## Abstract

This thesis describes an investigation of polarisation conversion effects in gallium arsenide optical waveguides. The research was carried out with the aims of predicting, preventing and harnessing such effects.

Experimental results are presented to demonstrate changes in the polarisation state of light propagating in passive deep-etched waveguides. The results are described by established modelling techniques. The effect due to process-dependent features of waveguide cross-section geometry, in particular asymmetry resulting from non-vertical etching, is investigated. The polarisation angles of hybrid waveguide modes are measured, and a novel technique is presented for the measurement of the difference between the effective indices of orthogonally polarised modes. The measurements obtained are used to analyse the evolution of elliptical polarisation states during propagation, and to provide an account of the physical origin of the polarisation conversion. Details of the nature of the optical modes predicted by rigorous numerical method simulations are demonstrated by the experimental results, while quantitative agreement between the simulated and measured data is shown. A simplified account of the behaviour is provided using a coupled-mode formulation. The influence of the linear electrooptic effect in modifying the polarisation conversion behaviour is explored experimentally, and is described using established theory. Quantitative benchmarks for the passive and electrooptic cases are provided by the experiments.

Waveguide designs are obtained which prevent unintended polarisation conversion in the presence of identified causes, while maintaining the main waveguide parameters of material composition, optical mode size and shape, electrooptic performance, and fabrication process. The polarisation behaviour in waveguides fabricated to these designs is evaluated, and the expected performance benefits are confirmed.

A novel waveguide device which provides electrooptic control and switching of the optical polarisation state is presented. The device is capable of converting any input polarisation state into an arbitrary output state using the linear electrooptic effect. A working design is obtained and the fabrication of devices is described. Experimental results are presented which demonstrate the concept. The design is compared to alternatives presented in the literature and advantages are identified, including favourable performance parameters, ease of fabrication using a standard process, and the potential for integration with other waveguide components. Further developments of the polarisation controller device are proposed, including the realisation of the potential for switching speeds at frequencies of tens of GHz.

## Acknowledgements

I would like to thank John Heaton for many tutorials and discussions, for supervising the early part of this work, and for the use of his computer programmes. I also thank Richard De La Rue and Michael Kane for supervising my work and providing much advice and encouragement.

A number of colleagues at Malvern contributed to this work with their efforts and experience. I am grateful to Denis Soley of the semiconductor growth team for his work in growing the aluminium gallium arsenide epitaxial wafers described in this thesis. Brian Smith, Julia Guest, Alan Hydes, Keith Hilton, Helen Johnson, Peter Wilding and Alison Munday, colleagues from the III-V semiconductor processing facility at Malvern, are thanked for the high quality processing of those wafers, and I gratefully acknowledge Andrew Simons for the SIMS characterisation of the wafers, and the detailed account of his technique.

I thank past and present colleagues David Wight, Edward Chidley, Philip Calcott, David Hayes, Geoffrey Ball, Mike Jenkins, Armando Loni, Brian Lowans, Alan Wilkinson and Rebecca Wilson for many useful discussions and encouragement.

A collaboration with the research group at City University led by Prof. Aziz Rahman and including Salah Obayya was relevant to this work. Their waveguide modelling results and discussions provided an understanding of some of the issues explored in this thesis, for which I am grateful.

I acknowledge the financial support of the Defence Evaluation and Research Agency and subsequently of QinetiQ Ltd.

I thank my parents for their encouragement.



## List of Published Work

- [1] E. D. Finlayson, J. M. Heaton, B. M. A. Rahman and S. S. A. Obayya, "Polarization Conversion in Passive Deep-Etched GaAs/AlGaAs Waveguides," *J. Lightwave Technol.*, vol. 24, no. 3, pp. 1425-1432, 2006.
- [2] "Electro-optic Polarisation Controller", United Kingdom Patent Application, No. 0617899.0, September 2006 (awaiting publication).

## **Content of the Thesis**

Chapter one is an introduction to the thesis. It contains a brief review of the history of the development of optoelectronic integrated circuits. The importance of being able to predict and control the optical polarisation state during propagation in waveguide devices is discussed and previous work carried out with these aims is reviewed. The objectives of the work presented in this thesis are stated.

Chapter two introduces the theoretical background to the work. Elements of relevant theory are presented, including the definitions and notations of polarisation states, the nature of optical modes in semiconductor waveguides, the techniques and computer models used for waveguide design, the coupled-mode theory for the description of polarisation transformations in waveguides and the theory of the linear electrooptic effect in GaAs.

Chapter three describes the experimental methods used in this work. The processes used for the fabrication of the waveguide devices and test structures are briefly described. The methods used for optical testing of waveguides are detailed, including a novel experimental technique for the measurement of waveguide birefringence.

Chapter four presents an experimental investigation of polarisation conversion in passive optical waveguides and compares the results with theoretical treatments.

Chapter five presents an experimental investigation of the influence of the electrooptic effect on polarisation conversion in optical waveguides and compares the results with theory.

Chapter six describes a method for waveguide design to prevent polarisation conversion while maintaining key waveguide parameters. Experimental designs are given and their performance is compared with predictions.

Chapter seven describes a novel waveguide device which provides universal electrooptic control and switching of the optical polarisation state. An experimental demonstration is presented.

Chapter eight summarises the research presented in the thesis and proposes further work.

# Contents

<b>Abstract</b>	<b>ii</b>
<b>Acknowledgements</b>	<b>iii</b>
<b>List of Published Work</b>	<b>iv</b>
<b>Content of the Thesis</b>	<b>v</b>
<b>Contents</b>	<b>vi</b>
<b>Chapter 1: Introduction</b>	<b>1</b>
1.1    Background	1
1.1.1    Optoelectronic integrated circuits in GaAs	1
1.1.2    Polarisation conversion in passive waveguides	2
1.1.3    Devices for polarisation control and modulation	3
1.2    Objectives	5
<b>Chapter 2: Theory</b>	<b>6</b>
2.1    The polarisation of light	6
2.2    Polarisation state representations	7
2.2.1    The Poincaré sphere	7
2.2.2    Jones Vector representation of polarisation states	7
2.2.3    Transformation matrices	9
2.3    Waveguide theory and design	10
2.3.1    Slab waveguide theory	10
2.3.2    Rectangular waveguide theory	13
2.3.3    Mode-filtering epitaxy design	13
2.3.4    Electrooptic waveguide configuration	14
2.4    Computer models used	14
2.4.1    Effective index method	15
2.4.2    Spectral index method	15
2.4.3    Numerical methods	15
2.5    Coupled-mode theory	16
2.6    The linear electrooptic effect in GaAs	20
<b>Chapter 3: Device Fabrication and Experimental Methods</b>	<b>23</b>
3.1    Device fabrication	23
3.1.1    GaAs wafer epitaxial growth	24
3.1.2    Photolithographic mask design and production	24
3.1.3    Wafer processing	24
3.2    Material characterisation	26

3.2.1	Determination of relative Al fraction as a function of depth	26
3.2.2	Determination of layer depths	27
3.2.3	Results	27
3.3	Optical testing	29
3.3.1	Mode angle measurements	29
3.3.2	Effective index difference measurements	31
3.3.3	Direct measurements of polarisation conversion	32
3.3.4	Optical loss measurements	32
<b>Chapter 4: Polarisation Conversion in Passive Waveguides</b>		<b>33</b>
4.1	Theory of polarised mode propagation	33
4.1.1	FMM method simulations	33
4.1.2	Elliptical polarisation analysis	39
4.1.3	Coupled-mode theory	39
4.2	Experiments	40
4.2.1	Experimental device design and fabrication	40
4.2.2	Experimental methods	40
4.3	Experimental results and comparisons	41
4.4	Conclusions	47
<b>Chapter 5: Polarisation Conversion in Electrooptic Waveguides</b>		<b>48</b>
5.1	Electrooptic polarisation conversion theory	48
5.1.1	Electrooptic index matching	49
5.1.2	Electrooptic coupling mechanism	50
5.2	Experiments	51
5.2.1	Experimental device design and fabrication	51
5.2.2	Experimental methods	53
5.2.3	Quantification of the linear electrooptic effect	54
5.3	Experimental results and comparisons	55
5.3.1	Phase-matching voltage versus width results	55
5.3.2	Offset electrode results	57
5.4	Conclusions	61
<b>Chapter 6: Prevention of Polarisation Conversion</b>		<b>62</b>
6.1	Purpose	62
6.2	Wafer design theory	62
6.3	Experiments	63
6.3.1	Test wafer epitaxy design	63
6.3.2	Experimental device design and fabrication	64
6.3.3	Experimental methods	65
6.4	Experimental results and comparisons	66
6.4.1	Optical loss measurements	66

6.4.2	Output mode profile observations	66
6.4.3	Index difference results	69
6.4.4	Passive waveguide polarisation conversion results	71
6.4.5	Electrooptic waveguide results	75
6.5	Conclusions	77
<b>Chapter 7: Electrooptic Polarisation Controller</b>		<b>79</b>
7.1	Device concept	79
7.2	Theoretical analysis	81
7.2.1	Electrooptic waveguide birefringence control in two dimensions	81
7.2.2	Conditions for arbitrary polarisation control	85
7.2.3	Transformation matrices	87
7.2.4	TE-TM switching	88
7.3	Experiments	89
7.3.1	Low frequency arbitrary polarisation state synthesiser design	89
7.3.2	Experimental methods	90
7.4	Results and comparison with theory	91
7.4.1	Arbitrary polarisation control	91
7.4.2	TE-TM switching	92
7.4.3	Field overlap and coupling constant calculations	95
7.5	Device variants	98
7.5.1	Travelling-wave device	98
7.5.2	Multiple stage devices	98
7.5.3	Integration of additional functions	100
7.6	Conclusions	101
<b>Chapter 8: Summary and Conclusions</b>		<b>103</b>
<b>References</b>		<b>107</b>

## **Chapter 1: Introduction**

### **1.1 Background**

#### **1.1.1 Optoelectronic integrated circuits in GaAs**

The field of integrated optics provides methods of generating, manipulating and detecting light on the same chip, with similar benefits to those provided by the integration of electronic circuits. In addition to the compactness and small mass of integrated optical devices, the fabrication of multiple components within a single process leads to low cost and enables the attainment of levels of device performance and complexity beyond those achievable using discrete components. Light may be manipulated in a number of ways, including the functions of phase modulation, intensity modulation, switching and routing, splitting and mixing, polarisation control and switching, wavelength filtering and multiplexing, spectrum analysis, and nonlinear wavelength generation. The basic component which provides the foundation for these functions is the optical waveguide.

Interest in planar waveguide devices began in the 1960's [3]-[4], influenced by the invention of the laser, the development of the optical fibre and the success of integrated electronics. III-V semiconductors were identified as suitable candidate materials due to the presence of the linear electrooptic effect [5]-[6], with the GaAs/AlGaAs alloy system favoured for the reasons of the availability of reliable high-quality epitaxial growth techniques, established processing techniques developed within the field of integrated electronics and the wide wavelength band of optical transmission [7]-[11]. Electrooptic phase modulation was demonstrated in GaAs waveguides in 1966 [12], in turn providing polarisation switching and intensity modulation [7], [10]. The implementation of phase modulators in a Mach-Zehnder interferometer intensity modulator configuration [13]-[16] offered a monolithic device for digital data transmission. The potential for high-speed modulation at microwave frequencies was identified [17]-[18], and devices were developed for on-off key (OOK) optical fibre communications. Compact intensity modulators have been demonstrated, utilising the enhanced electrooptic effects exhibited close to the absorption edge in waveguides containing quantum wells [19]-[24].

The application in Dense Wavelength Division Multiplexing (DWDM) has become the main driving force behind the development of optical waveguide devices, with devices such as modulators, wavelength multiplexers and routers fabricated in materials including LiNbO<sub>3</sub>, GaAs and InP having reached the market. Numerous other applications exist, for example in

optical signal processing, microwave photonic applications and remote sensing [25]-[31]. The strong optical confinement available in GaAs waveguides, combined with the development of low-loss small-radius waveguide bends [32]-[34] and efficient high-order multimode interference (MMI) splitters and recombiners [35]-[36] has enabled the fabrication of complex photonic integrated circuits containing a high density of components.

Recent developments have included demonstrations of photonic wire waveguides [34] and photonic crystal waveguide structures [37]-[44], both of which feature physical dimensions on the scale of the optical wavelength. There is currently an effort to realise in silicon the optical functions currently available in GaAs [45]-[54], to permit the monolithic integration of optical and electronic functions using complementary metal-oxide semiconductor (CMOS) technology. This research has the purpose of enabling intra-chip optical communication and chip interconnects, driving future advances in microprocessor performance.

### **1.1.2 Polarisation conversion in passive waveguides**

Polarisation effects are of interest to the photonic circuit designer for two reasons. Firstly, the operation of many devices, such as electrooptic intensity modulators, is not independent of the polarisation state of the light. For the operation of high performance waveguide devices the light must be maintained in the required state; it is therefore important to understand the circumstances in which unwanted polarisation conversion may occur in order to design devices which are not susceptible. Secondly, the added function of deliberate manipulation of the polarisation state brings further scope for integration and broadens the potential application of integrated optics.

Earlier work has been directed at the prediction and demonstration of deliberate polarisation conversion in integrable structures, including asymmetric passive waveguides [55]-[64], bending waveguides [65]-[67] and strained waveguides [68], while experimental methods have been presented for the characterisation of polarisation crosstalk in long silica waveguides [69]-[71]. Studies have been made of the design and control of modal birefringence in planar waveguides [72]-[74]. Theoretical work using the finite element method has explored polarisation behaviour in high-index-contrast waveguides of nominally rectangular cross section [75], [76]. The modelling has provided a thorough understanding of the conversion mechanism presented by small asymmetry in straight passive waveguides. Detailed experimental observations of this behaviour in GaAs/AlGaAs waveguides, including evidence of the physical origin of the conversion as predicted by the theory, are presented in this thesis and in reference [1].

### 1.1.3 Devices for polarisation control and modulation

The fixed TE-TM polarisation transformation performed by passive waveguide devices is analogous with the function of a non-rotatable half-wave plate. Other polarisation manipulation functions in waveguide devices reported in the literature include polarisation splitting and multiplexing [77]-[80], optical isolation [81], single polarisation transmission [82], polarisation scrambling [133] and electrooptic polarisation modulation. The latter is of particular importance, having broad applicability. Specific applications for electrically controlled polarisation modulators have been identified in optical telecommunications, including polarisation shift keying (PolSK) [83], polarisation multiplexing and the compensation of polarisation mode dispersion (PMD) [84]. Electrooptic polarisation switching has also been proposed for transmitters in quantum cryptography [85].

The simplest form of electrooptic polarisation modulator in GaAs is the phase modulator of references [5]-[7], in which induced birefringence produces a restricted set of output polarisation states. One of a number of specific orientations of the waveguide with respect to the crystal lattice must be used. In these devices, a vertical applied electric field in the waveguide core results in birefringent axes which are aligned to the polarisation angles of the modes of the passive waveguide. Consequently, only the relative phase of the field components of the vertical and horizontal modes can change, and not the relative magnitude. In the usual mode of operation, the field components are chosen to have equal magnitude, so that the restricted set of output states includes two orthogonal linear states polarised at  $\pm 45^\circ$  to the epitaxial plane. This kind of device offers limited scope for monolithic integration with other waveguide components in GaAs because it is not compatible with the horizontal polarisation state that is usually required.

Several variants of an alternative form of electrooptic polarisation controller have been reported in the literature [86]-[89]. A feature common to all of these is the use of a horizontal applied electric field in the waveguide core, which is typically produced by a voltage applied between electrodes placed on either side of a shallow-etched waveguide, in a plane that coincides with the optical mode. The horizontal electric field enables coupling between horizontal and vertical polarisation components by altering the refractive index ellipsoid (the optical indicatrix) of the semiconductor crystal in such a way that the principal dielectric axes exist at angles of  $+45^\circ$  and  $-45^\circ$  to those directions. However, in general the polarised modes of the waveguide device are not orientated at the  $+45^\circ$  and  $-45^\circ$  angles of the crystal birefringence because of the waveguide birefringence introduced by the waveguide boundaries. For complete conversion from the horizontal input polarisation to a vertical



output polarisation to occur, it is necessary to eliminate or allow for the waveguide birefringence (also called the phase mismatch).

The devices referenced above suffer from shortcomings such as limited polarisation conversion efficiency or the requirement for specialised fabrication processes that prevent integration with other waveguide devices. For example, the device proposed by Rahmatian et al. [88] uses low-birefringence waveguides without independent electrooptic control of the phase mismatch. The device reported by Schlak et al. [86] allows for the presence of the phase mismatch by using a periodic reversal of the horizontal electric field direction with a longitudinal period matched to the phase-reversal length. This requires complex drive circuitry and a specialised fabrication process. The polarisation converter proposed by Grossard et al. [87] does provide independent electrooptic control of the phase mismatch by the application of a vertical electric field component. However, there are drawbacks resulting from the specific configuration of the electrodes, whereby an electrode to the side of the optical region is used as the ground for an electrode on top of the waveguide and for an electrode on the opposite side of the waveguide, without a separate ground plane underneath the waveguide. This arrangement suffers from poor overlap of the vertical and horizontal electric field components with the optical field; consequently, the required switching voltages are large. Because of the horizontal offset of the ground electrode, a voltage signal applied between the top electrode and ground results in both vertical and horizontal electric field components being produced. This prevents the integration of devices that require only a vertical electric field, such as phase modulators and Mach-Zehnder interferometers. Additionally, to allow placement of the lateral electrodes in the same plane as the optical field, the waveguide must be formed by shallow etching, which limits the scope for control of the waveguide birefringence in the waveguide design, and precludes the possibility of integration of waveguide components that require deep etching, such as small-radius bends, unless a more complicated fabrication process is used.

A novel polarisation controller device [2] is presented in this thesis, which uses a unique approach to avoid some of the shortcomings of the existing technology described. The device features a pair of coplanar electrodes on top of a deep-etched waveguide, out of the plane of the optical mode, with a ground plane underneath the waveguide. This is shown to produce independently controllable horizontal and vertical field components of requisite magnitude within the waveguide core to enable accurate arbitrary polarisation control. The device provides the integrated optical equivalent of a particular combination of bulk optical phase retarders, which may be used to convert any polarisation state to any other polarisation state. Such a system consists of a quarter-wave plate followed by a half-wave plate followed by a second quarter-wave plate, all of which may be rotated in the plane perpendicular to the direction of propagation. The first quarter wave plate converts any elliptical polarisation to a

linear state polarised along either of the axes of the ellipse. The half wave plate rotates the linear polarisation to any angle. The second quarter wave plate converts the linear state to any elliptical state with the same major axis. This system is inherently expensive as it consists of three optically flat components which require antireflection coated surfaces if they are not to cause significant back reflections or introduce optical loss. Suitable rotation mounts are required, with manual or motorised control. The system has the further disadvantages that it requires collimated light and that the waveplates are wavelength sensitive. If used in a fibre-optic system, optimisation of the coupling between the fibres and the collimated free space beam can be labour-intensive and can introduce optical loss. The limitations of this bulk optical system serve to further emphasise the utility of the integrated optical approach.

## 1.2 Objectives

The purpose of the research described in this thesis is to provide an understanding of polarisation effects in gallium arsenide optical waveguides, primarily through experimental demonstration. The research was carried out with the particular aims of enabling the prediction, prevention or harnessing of such effects.

Although the work presented was carried out using waveguides fabricated in the GaAs/AlGaAs materials system, most of the findings are applicable to other III-V semiconductor materials such as InP/InGaAsP, and some are applicable to any dielectric optical waveguide. Polarisation effects in bending waveguides or guides containing discontinuities in the direction of propagation are excluded.

The specific goals are:

1. To demonstrate by experiment the mechanism by which unwanted polarisation conversion occurs in waveguides that possess cross-sectional asymmetry, as predicted by theory. To describe this behaviour in terms of the coupled-mode theory, and provide an experimental benchmark to quantify the effect.
2. To extend the above demonstration to include electrooptic effects.
3. To describe and demonstrate a method of waveguide design that prevents unwanted polarisation conversion within the constraints of the use of an unchanged fabrication process, an unchanged waveguide cross section, established material compositions, maintenance of single mode propagation, and without disruption of the output mode profile.
4. To demonstrate a new invention of an electrooptic polarisation controller that provides arbitrary polarisation transformations, is fabricated using a standard process, and can be integrated with other waveguide components.

## Chapter 2: Theory

### 2.1 The polarisation of light

Light may be represented as a transverse electromagnetic wave [90]-[91]. The polarisation of light is usually defined in terms of the temporal behaviour of the optical electric field vector  $E$ , observed at a fixed point in space. Three other field vectors are required for a complete description of light: the electric displacement (or electric flux density)  $D$ , the magnetic field strength  $H$  and the magnetic flux density  $B$ . These are related to the electric field strength by Maxwell's equations. In this work the assumption of monochromatic, coherent, polarised light as approximated by the output from a laser will be made throughout.

In a general Cartesian coordinate system, the electric field vector of a uniform, monochromatic, transverse electromagnetic wave of arbitrary polarisation propagating along  $z$  with wavelength  $\lambda_0$  in free space is given by:

$$E(z, t) = \left[ A_y \cos\left(\omega t - \frac{2\pi}{\lambda_0} z + \delta_y\right) \right] y_u + \left[ A_x \cos\left(\omega t - \frac{2\pi}{\lambda_0} z + \delta_x\right) \right] x_u \quad (2.1.1)$$

where  $A_y$  and  $A_x$  are the amplitudes of the optical electric field components along the horizontal  $y$  axis and the vertical  $x$  axis respectively,  $y_u$  and  $x_u$  are unit vectors along those axes,  $\omega$  is the optical angular frequency and  $\delta_y$  and  $\delta_x$  are absolute phase terms. It may be shown that in general the  $E$  vector of a repeating time-harmonic optical field measured from a fixed point in space will trace out an ellipse [92]-[93]. The polarisation state is therefore described as elliptical, which includes the special cases of linear and circular polarisations.

Given the stated assumptions, the ellipse is orientated in the plane orthogonal to the propagation direction  $z$ . If the absolute phase is neglected, and the amplitude is normalised, the elliptical polarisation may be defined by the following parameters:

1. The azimuth angle  $\theta$ , which is the angle of the direction of the major axis measured anticlockwise from the horizontal. The directions of the major and minor axes of the ellipse are orthogonal to each other and to  $z$ . The azimuth angle has values in the range  $-\pi/2$  to  $\pi/2$ .
2. The ellipticity  $e$ , given by the ratio of the field amplitude along the minor axis of the ellipse to that along the major axis. The ellipticity has values in the range  $-1$  to  $1$ , where positive and negative values of  $e$  are defined corresponding to right and left handed polarisations respectively. For right handed polarisations, the electric field vector rotates in an anticlockwise direction when viewed along the direction of propagation. It is convenient to define the ellipticity angle  $\phi_e$ , equal to  $\tan e$ .

## 2.2 Polarisation state representations

### 2.2.1 The Poincaré sphere

The use of a spherical surface to represent all of the available polarisation states was proposed by Poincaré in 1892 [94]. The Poincaré sphere, which is depicted with the positions of some polarisation states in Fig. 2.1, has the following properties:

1. The south and north poles represent left-hand and right-hand circular polarisations respectively.
2. Each point on the equator of the sphere represents a linear polarisation.
3. All other points on the sphere represent elliptical polarisation states. In the southern hemisphere they are left handed; in the northern they are right handed.
4. The lines of longitude, or lines of equal azimuth, each represent polarisation states with the same major axis azimuth angle.
5. The lines of latitude represent polarisation states with equal ellipticity.

A polarisation state represented by the point  $P$ , on the Poincaré sphere may also be described in a Cartesian coordinate system with the parameters  $(S_0, S_1, S_2, S_3)$  in which  $S_0$  denotes the radius of the sphere. The parameters are given by [92]:

$$\begin{aligned}
 S_0 &= \frac{1}{2} \\
 S_1 &= \cos(2\phi_e)\cos(2\theta)/2 \\
 S_2 &= \cos(2\phi_e)\sin(2\theta)/2 \\
 S_3 &= \sin(2\phi_e)/2
 \end{aligned} \tag{2.2.1}$$

When the radius is multiplied by two, equations (2.2.1) are known as the Stokes parameters.

### 2.2.2 Jones Vector representation of polarisation states

A concise representation of the polarisation state may be obtained by carrying out the following steps to reduce the electric field vector equation (2.1.1):

1. Removal of the unit vectors by grouping the scalar components in a column vector.
2. Suppression of the temporal information.
3. Suppression of the spatial information.

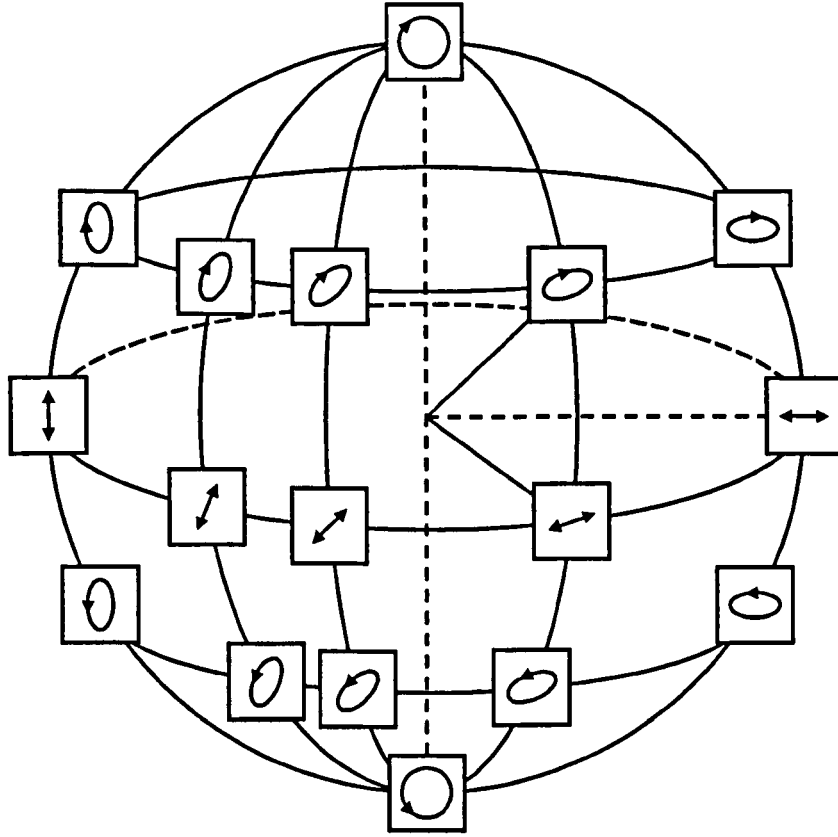


Fig. 2.1: The Poincaré Sphere.

Equation (2.1.1) is then replaced by equation (2.2.3), where  $i$  is the imaginary unit:

$$E(0) = \begin{bmatrix} A_y e^{i\delta_y} \\ A_x e^{i\delta_x} \end{bmatrix} \quad (2.2.3)$$

$E(z,t)$  in free space may be retrieved from  $E(0)$  using the following equation:

$$E(z,t) = \text{Re} \left[ E(0) e^{i \left( \omega t - \frac{2\pi}{\lambda_0} z \right)} \right] \quad (2.2.4)$$

Equation (2.2.3) expresses the electric field vector in terms of field amplitudes in the  $y$  and  $x$  directions and the phases of the two components. This form is valid given the conditions required by equation (2.1.1). It is also valid for a dielectric waveguide if those conditions are met by making the following assumptions:

1. The electric field is purely transverse to the direction of propagation, i.e. the component along  $z$  is neglected.
2. The relative spatial profile of the guided light is considered to be invariant. This may be assumed if only the fundamental modes propagate, and if the spatial distributions of the two orthogonally polarised modes are sufficiently similar that they may be considered identical.
3. The electric field vector has the same direction at all points across a mode.

These assumptions are valid approximations for the waveguides considered in this work. It is convenient to make further simplifications. Firstly, the wave amplitude is normalised to unity. Secondly, only the relative phases of the two components are considered. This is sufficient to describe the polarisation state. The Jones vector then has the form [92]:

$$\begin{bmatrix} A_y \\ A_x \end{bmatrix} = \begin{bmatrix} \cos \theta e^{i\phi} \\ \sin \theta \end{bmatrix} \quad (2.2.5)$$

where  $\phi$  is the phase difference  $\delta_x - \delta_y$  and  $\theta$  gives the azimuth angle as before.

### 2.2.3 Transformation matrices

A change in polarisation state may be described by a transformation matrix  $P$ , which is multiplied by the initial Jones vector to give the new Jones vector. Transformation matrices for actions occurring in sequence in a system or device may be multiplied to obtain a single matrix describing the whole system [92]. Two important transformation matrices which are relevant to electrooptic GaAs waveguides are given below.

#### 1. Phase shift

$$P = \begin{bmatrix} e^{i\Delta\phi} & 0 \\ 0 & 1 \end{bmatrix} \quad (2.2.6)$$

$\Delta\phi$  gives the phase shift, which, in general, has two components:  $(\Delta\phi)_p$ , the phase shift due to passive waveguide modal birefringence, and  $(\Delta\phi)_{EO}$ , the electrooptically induced phase shift due to applied electric fields. An expression for the phase shift is given later.

#### 2. Coordinate transformation

Coordinate transformations, which map one set of Cartesian axes onto another, are required in the analysis of electrooptic birefringence. For example, the transformation given in equations (2.2.7) gives a new set of axes  $x'$  and  $y'$  in terms of the old  $x$  and  $y$ , as shown in Fig. 2.2.

$$x = x' \cos \theta + y' \sin \theta \quad y = y' \cos \theta - x' \sin \theta \quad (2.2.7)$$

This may be expressed as a matrix multiplication of an electric field vector:

$$\begin{bmatrix} A_y \\ A_x \end{bmatrix} = \begin{bmatrix} \cos \theta & -\sin \theta \\ \sin \theta & \cos \theta \end{bmatrix} \begin{bmatrix} A_{y'} \\ A_{x'} \end{bmatrix} \quad \text{and} \quad \begin{bmatrix} A_{y'} \\ A_{x'} \end{bmatrix} = \begin{bmatrix} \cos \theta & \sin \theta \\ -\sin \theta & \cos \theta \end{bmatrix} \begin{bmatrix} A_y \\ A_x \end{bmatrix} \quad (2.2.8), (2.2.9)$$

where the  $2 \times 2$  matrices are the transformation matrices that describe the transitions between a section of waveguide with modes polarised along  $y$  and  $x$ , and a section with modes polarised along  $y'$  and  $x'$ .

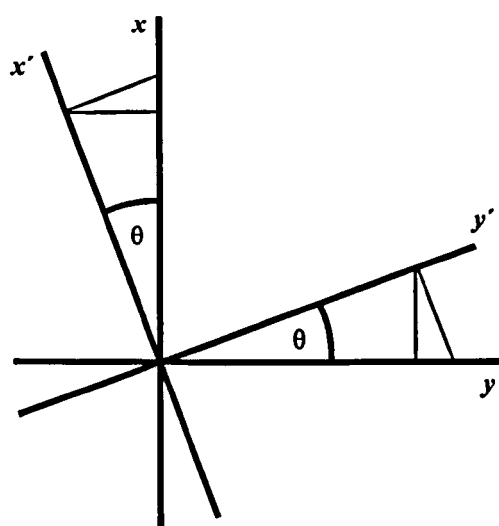


Fig. 2.2: The axis components in an example of a coordinate transformation that expresses a set of Cartesian axes  $x$  and  $y$  in terms of a new set of axes  $x'$  and  $y'$ .

2.3 Waveguide theory and design

2.3.1 Slab waveguide theory

The main properties and design principles of optical waveguides may be understood by consideration of the slab waveguide, shown in Fig 2.3, which is infinite in the  $y$  direction. Light is guided along the core by total internal reflection [95] provided the core refractive index  $n_2$  is larger than the cladding indices  $n_1$  and  $n_3$ . From Snell’s Law of refraction, the critical angle  $\theta_c$  may be derived, giving the minimum angle of incidence  $\theta_i$  for total internal reflection [96]. This is given for the case where  $n_1$  is larger than  $n_3$  by equation (2.3.1).

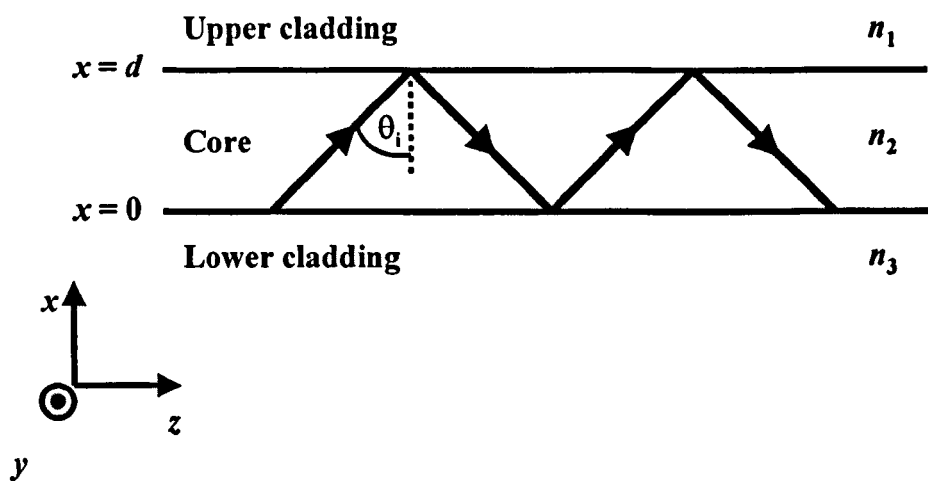


Fig. 2.3: Schematic diagram of a slab waveguide in cross section, in general Cartesian coordinates.

$$\theta_c = \sin^{-1} \left( \frac{n_1}{n_2} \right) \quad (2.3.1)$$

In order to describe and predict the behaviour of guided light, it is necessary to obtain expressions for the waveguide modes, which are discrete solutions for spatial amplitude distribution plus an associated propagation constant and polarisation state. This may be carried out by solving for a wave equation in each region of the waveguide under the constraints of the boundary conditions at the dielectric interfaces and at  $x = \pm\infty$ . The procedure for a slab waveguide is described in a number of textbooks [97]-[99] and is not reproduced here. However, a limited treatment is instructive [97].

The wave equations for the electric field  $E$  and the magnetic field  $H$  can be derived from Maxwell's equations [100] and expressed as [97]:

$$\nabla^2 E + \omega^2 \mu \epsilon_0 \epsilon_r E = 0, \quad \nabla^2 H + \omega^2 \mu \epsilon_0 \epsilon_r H = 0 \quad (2.3.2), (2.3.3)$$

where  $\epsilon_0$  is the permittivity of free space,  $\epsilon_r$  is the dielectric constant of the medium,  $\mu$  is the permeability, and  $\omega$  is the radian frequency. Given uniformity in  $y$  and assuming a solution of the form of a plane wave propagating along  $z$ :

$$E(\mathbf{r}, t) = E(x, y) e^{i(\omega t - \beta z)} \quad (2.3.4)$$

the wave equation (2.3.2) can be written for each of the three index regions as [97]:

$$\frac{\partial^2}{\partial x^2} E(x, y) + (k_0^2 n^2 - \beta^2) E(x, y) = 0 \quad (2.3.5)$$

where  $n$  is the refractive index of the region under consideration,  $\beta$  is the propagation constant and  $k_0$  is related to the free space wavelength  $\lambda$  by:

$$k_0 = \omega \sqrt{\mu_0 \epsilon_0} = \frac{2\pi}{\lambda_0} \quad (2.3.6)$$

in which  $\mu_0$  is the permeability of free space. Inspection of equation (2.3.5) reveals that the

term  $\frac{1}{E} \frac{\partial^2 E}{\partial x^2}$  is positive if  $\beta > k_0 n$  and negative if  $\beta < k_0 n$ . If  $n_2 > n_1 > n_3$ , which is the case

relevant to this work, then the condition  $k_0 n_1 < \beta < k_0 n_2$  results in  $\frac{1}{E} \frac{\partial^2 E}{\partial x^2}$  being negative in

the core and positive in the cladding regions. This result yields solutions for the electric field distribution that are sinusoidal in the core and exponential in the cladding regions, which represents confinement of light in the core, with evanescent fields outside it. These solutions represent modes that have discrete propagation constants, and can be regarded as being

subject to an effective index  $n_{\text{eff}}$ , such that  $\beta = \frac{2\pi n_{\text{eff}}}{\lambda_0}$ . The second important circumstance is



that of  $\beta < k_0 n_3$ , in which case the field in the region 3 is also sinusoidal, representing leakage of light out of the core into the lower cladding.

Two sets of mode solutions exist in the slab waveguide, with orthogonal polarisations. Transverse electric (TE) modes have an electric field component only in the horizontal direction, with the magnetic field directed substantially in the vertical direction. Transverse magnetic (TM) modes have a magnetic field component only in the horizontal direction, with the electric field directed substantially in the vertical direction. TE and TM modes of the same order have different propagation constants due to the different boundary conditions applicable at the dielectric interfaces for electric and magnetic fields. There are also subtle differences in the field profiles. The boundary conditions for electric and magnetic field components tangential or normal to dielectric interfaces are summarised in Table 2-I [100]. For the slab waveguide, the upper two rows of Table 2-I apply to the TE modes, and the lower two to TM modes. Additionally, the gradients of both electric field components must be continuous across the boundary. This fact, plus the discontinuity of the normal  $E$  field means that the TM mode of a given order has an evanescent field of larger amplitude than the equivalent TE mode. The TM mode penetrates further into the cladding regions, and consequently has a smaller effective index. This conclusion will be drawn upon later, as it is relevant to the study of polarisation transformations in optical waveguides.

Field component	Boundary condition
Tangential $E$	Continuous
Normal $H$	Continuous
Normal $E$	Discontinuous such that $n^2 E$ is continuous
Tangential $H$	Continuous

Table 2-I: Boundary conditions at dielectric interfaces. In determining the boundary condition for the normal component of  $H$ , the assumption is made that the relative permeability  $\mu_r$  of a dielectric is equal to 1, so that  $\mu = \mu_0$ . Otherwise, the relevant boundary condition would be the continuity of the normal component of the magnetic flux density  $B$ .

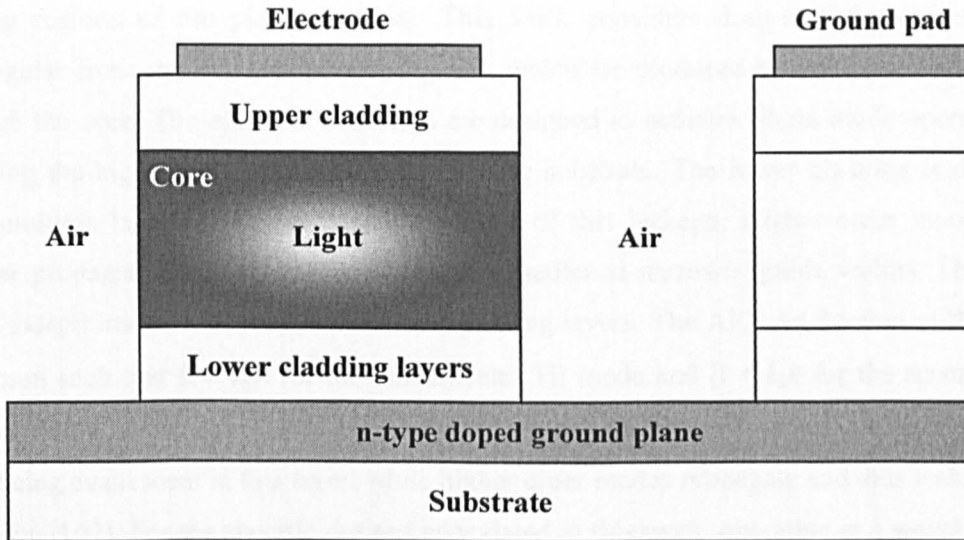


Fig. 2.4: Schematic of a deep-etched electrooptic waveguide cross section and ground connection arrangement. The ground pad is forward-biased with respect to the electrode, so that the applied voltage is dropped between the electrode and the n-type doped ground plane.

### 2.3.2 Rectangular waveguide theory

A schematic diagram of a deep-etched dielectric waveguide cross section is shown in Fig. 2.4. If light is confined laterally as well as vertically in a rectangular waveguide structure such as this, there is no exact analytic solution to the problem [101]. Modelling of the modes of such waveguides requires either an analytic approximation such as the effective index method, or a calculation intensive numerical method. The techniques used during the course of this work are described in section 2.4. Optical modes in a dielectric waveguide of rectangular cross section are hybrid in nature, having electric and magnetic field components along three axes [76]. Also, the nett directions of the  $E$  and  $H$  vectors are not completely uniform across the mode. Nonetheless, the convention persists that modes with optical electric fields substantially parallel to and perpendicular to the epitaxial layers are referred to as TE and TM modes respectively. Specific aspects of the nature of the modes and the consequences for polarised mode propagation are investigated in chapter four.

### 2.3.3 Mode-filtering epitaxy design

In the aluminium gallium arsenide alloy system, vertical confinement is achieved by substituting a fraction of gallium with aluminium during epitaxial growth of the cladding layers, resulting in a smaller refractive index than that of the GaAs core [102]-[105]. This is possible without disrupting the crystal because the lattice constant of AlAs is similar to that of GaAs [106], [103]. Lateral confinement is provided by the interfaces with air produced by

etching regions of the planar material. This work considers deep-etched waveguides of rectangular cross section, as shown in Fig. 2.4, which are produced by etching all of the way through the core. The epitaxial structures are designed to achieve single mode operation by allowing the higher order modes to leak into the substrate. The lower cladding is designed with multiple layers to permit accurate control of this leakage. Higher order modes have smaller propagation constants, which become smaller at narrower guide widths. The mode fields extend into the deepest of the lower cladding layers. The AlGaAs fraction of this layer is chosen such that  $\beta > k_0 n$  for the fundamental TE mode and  $\beta < k_0 n$  for the second order (lateral) TE mode at the required guide width. This condition results in the fundamental mode field being evanescent in this layer, while higher order modes propagate and thus leak into the substrate [107]. For the specific designs considered in this work, operating at a wavelength of  $1.55\ \mu\text{m}$ , the second order mode cuts off at a guide width of around  $5\ \mu\text{m}$ , while the fundamental mode remains subject to low loss in guides as narrow as  $3\ \mu\text{m}$ . This defines the range of useful guide widths.

### 2.3.4 Electrooptic waveguide configuration

Electric fields are applied in the waveguide by contacting the top metal electrode and the n-type ground plane. For specific orientations of the waveguide with respect to the GaAs crystal, the applied field causes a change in the refractive index due to the linear electrooptic effect (Pockels effect). Silicon is used as the n-type dopant in the second and third lower cladding layers [108]. Gold bond pads on unetched material connected to the top electrode provide a large area, typically greater than  $100\ \mu\text{m}$  square, which may be contacted by probes or bond wires. The metal deposited on semiconductor forms a Schottky barrier diode [109] which must be reverse biased for the applied voltage to be dropped across the waveguide core. The ground plane is contacted by forward biasing a diode formed by another bond pad nearby, also on unetched material, surrounded by etched regions. This arrangement, which is shown in Fig. 2.4, was preferred in this work to an alternative configuration in which the ground pad is deposited directly onto the ground plane exposed by etching, which requires an additional processing step.

## 2.4 Computer models used

Several computer models were used during the course of this work, both for device design and interpretation of results. These fit into either of two categories. Analytic approximations such as the effective index method and the spectral index method are efficient techniques for

obtaining basic waveguide design information, but are of limited use in describing the principles explored in this work because they require the assumption that the modes are polarised purely TE or TM. Numerical methods are more sophisticated, more versatile and generally more accurate. Some numerical methods provide full-vector mode solutions, for waveguide structures of arbitrary cross section. These techniques are calculation intensive, but their rigorous treatment of the problem is essential for a detailed understanding of the physics explored here. The methods used are described briefly in this section.

#### **2.4.1 Effective index method**

An effective index method [110]-[112] computer programme written by John Heaton was used in this work. The method involves the calculation of the effective index of the mode of interest for the slab structure as outlined above. The modes are assumed to be TE and TM polarised. The system is then rotated through  $90^\circ$  and the structure is treated, in the case of deep etched waveguides, as a uniform core bounded by air. The slab effective index is substituted for the refractive index of the core of the second slab, and the calculation is repeated with the new boundaries. The effective index method programme was used to model the effective indices of the waveguide modes.

#### **2.4.2 Spectral index method**

A Spectral Index method programme was used to model leakage into the substrate [113], [114]. This technique is also capable of simulating the component of loss due to absorption, but this facility was not used in the design of the devices used in this work. This method is also restricted to the assumption of purely TE and TM polarised modes, and the programme used was also limited in that it used the assumption of zero evanescent field at the GaAs-air boundaries to minimise computation time. This feature makes the available programme unsuitable for modelling effective indices.

#### **2.4.3 Numerical methods**

FIMMWave is a commercial software package which contains several different modelling tools. The film mode matching method (FMM) [115] was used in this work to provide full-vectorial mode solutions for waveguides of arbitrary cross section, with the limitation that oblique boundaries in the cross section must be approximated by a series of steps. It is an example of the sophisticated design tools that have become available commercially in recent

years. This software was used to produce simulations used in providing some of the comparisons with experimental results, and in describing the theoretical background to this work. FIMMWave was not used in the design phase of this research.

Additionally, substantial insight into the issues described in this thesis were obtained from simulations provided by Prof. Rahman and his research group at City University using their vector finite element method (VFEM) techniques [61], [72], [75]-[76], [82], [116]-[118].

## 2.5 Coupled-mode theory

A coupled-mode approach is useful for describing many problems involving energy exchange between modes. Optical filtering, second harmonic generation, directional coupling and polarisation conversion in waveguide bends [66] may be described by coupled-mode theory. The technique is also applicable to the case of polarisation conversion in linear waveguides investigated in this work. The formulation permits the assumption that the modes of the waveguide have pure TE and TM polarisations, and coupling between the two is permitted in the presence of a coupling mechanism. A number of coupling mechanisms may be envisaged, including asymmetry in the waveguide cross section, or anisotropy due to the electrooptic effect or stresses in the material.

The slowly-varying mode amplitudes change during propagation along length  $z$  according to the coupled equations [119]:

$$\frac{dE_{\text{TM}}}{dz} = -i\kappa E_{\text{TE}} e^{-i2\delta z} \quad (2.5.1)$$

$$\frac{dE_{\text{TE}}}{dz} = -i\kappa E_{\text{TM}} e^{i2\delta z} \quad (2.5.2)$$

The coupling constant  $\kappa$  describes the strength of the coupling mechanism. The phase mismatch is given by  $2\delta$ , which is equal to the difference of the mode propagation constants:

$$2\delta = \Delta\beta = \beta_{\text{TM}} - \beta_{\text{TE}} = \frac{2\pi}{\lambda_0} (n_{\text{TM}} - n_{\text{TE}}) \quad (2.5.3)$$

where  $n_{\text{TM}}$  and  $n_{\text{TE}}$  are the effective indices of the respective transverse modes. If  $E_{\text{TM}} = 0$  and  $E_{\text{TE}} = 1$  at  $z = 0$ , i.e. the input state is TE, the solutions of (2.5.1) and (2.5.2) are [119]:

$$E_{\text{TM}}(z, \kappa, \delta) = -i \left( \frac{\kappa}{\sqrt{\kappa^2 + \delta^2}} \right) \sin \left( z \cdot \sqrt{\kappa^2 + \delta^2} \right) e^{-i\delta z} \quad (2.5.4)$$

$$E_{\text{TE}}(z, \kappa, \delta) = \left\{ \cos \left[ z \sqrt{\kappa^2 + \delta^2} \right] - i \left[ \left( \frac{\delta}{\sqrt{\kappa^2 + \delta^2}} \right) \sin \left( z \cdot \sqrt{\kappa^2 + \delta^2} \right) \right] \right\} e^{i\delta z} \quad (2.5.5)$$

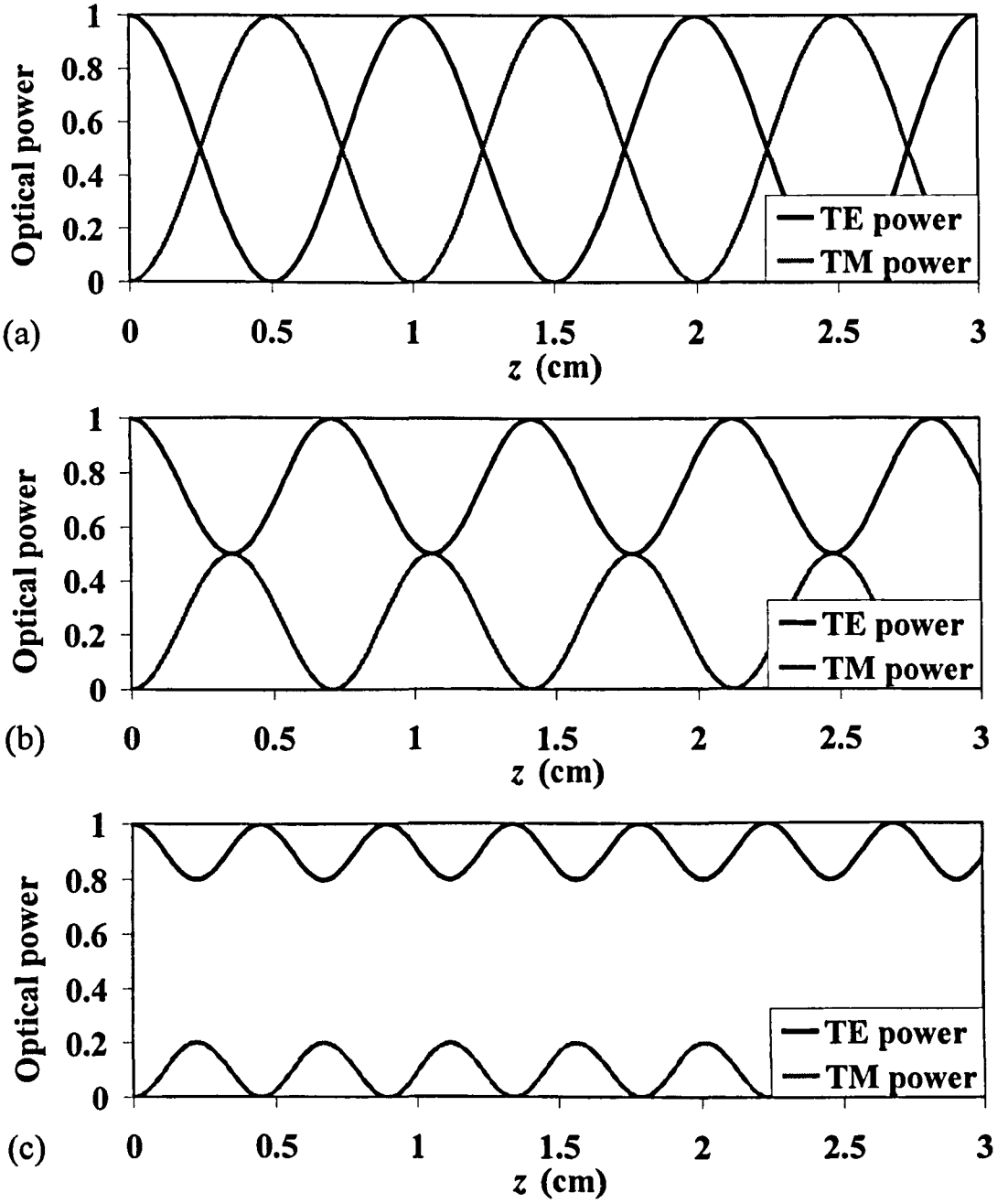


Fig. 2.5: Coupled-mode theory predictions of normalised TE and TM mode power versus length  $z$  given a TE input polarisation, for a value of the coupling constant  $\kappa = \pi \text{ cm}^{-1}$ , with three phase difference conditions: (a) phase-matched case,  $\Delta\beta = 0$ , (b)  $\Delta\beta = 2\pi \text{ rad/cm}$ , (c)  $\Delta\beta = 4\pi \text{ rad/cm}$ .

The power in the TE and TM modes and hence the polarisation extinction may be calculated from (2.5.4) and (2.5.5), provided that values for  $\kappa$  and  $\Delta\beta$  are available. Differentiation of the TM power with respect to  $z$  reveals that its maximum is first reached at a length given by:

$$z_{\text{TM max}} = \frac{\pi}{2\sqrt{\kappa^2 + \delta^2}} \quad (2.6.6)$$

An expression for the envelope of maximum TM power as a function of phase mismatch for a given coupling constant may then be obtained:

$$P_{\text{TMmax}} = \frac{\kappa^2}{\kappa^2 + \delta^2} \quad (2.6.7)$$

Fig. 2.5 shows the power in the two modes as they propagate along  $z$ , given by the real parts of the magnitudes of  $E_{\text{TE}}$  and  $E_{\text{TM}}$  respectively. In this example the magnitude of the coupling constant is  $\kappa = \pi \text{ cm}^{-1}$ . In Fig. 2.5a the modes are phase matched, in which case complete coupling occurs over a coupling length which is dependent on the coupling constant, and is given by  $\kappa z = \pi/2$ . Figs. 2.5b and 2.5c show examples of the phase-mismatched case, with  $\Delta\beta = 2\pi$  and  $4\pi \text{ rad/cm}$  respectively. In the absence of phase matching incomplete power transfer from TE to TM occurs before the light begins to couple back again. Also, the coupling length becomes progressively shorter as the magnitude of  $\Delta\beta$  increases, for a given value of  $\kappa$ .

Fig. 2.6 shows the power in the TE and TM modes versus  $\Delta\beta$  at the coupling length, for the same example of coupling strength,  $\kappa = \pi \text{ cm}^{-1}$ . The TM curve has a characteristic shape that consists of a series of conversion peaks that become progressively weaker as the phase difference increases. Where there is a large index mismatch very little power can couple between the modes. The evolution of the TM signal through ten equally spaced values of  $z$  is shown in Fig. 2.7 for fixed  $\kappa$  equal to  $\pi \text{ cm}^{-1}$ , with  $z$  ranging from 0.25 cm to 2.5 cm. The envelope of maximum TM power is also shown. At  $\Delta\beta = 0$ , the TM power repeatedly rises to 1 then falls back to zero. A larger coupling constant would result in more rapid conversion and a change in the shape of the TM power envelope, given by equation (2.6.7).

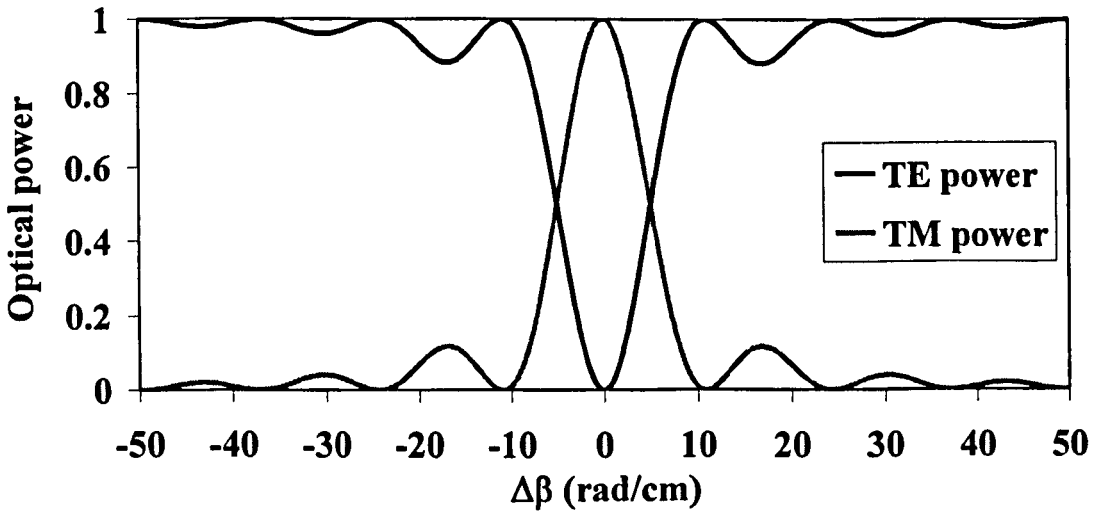


Fig. 2.6: Coupled-mode theory prediction of normalised TE and TM power versus  $\Delta\beta$  given a TE input, for a value of the coupling constant  $\kappa = \pi \text{ cm}^{-1}$ , at a length  $z = 0.5 \text{ cm}$ .

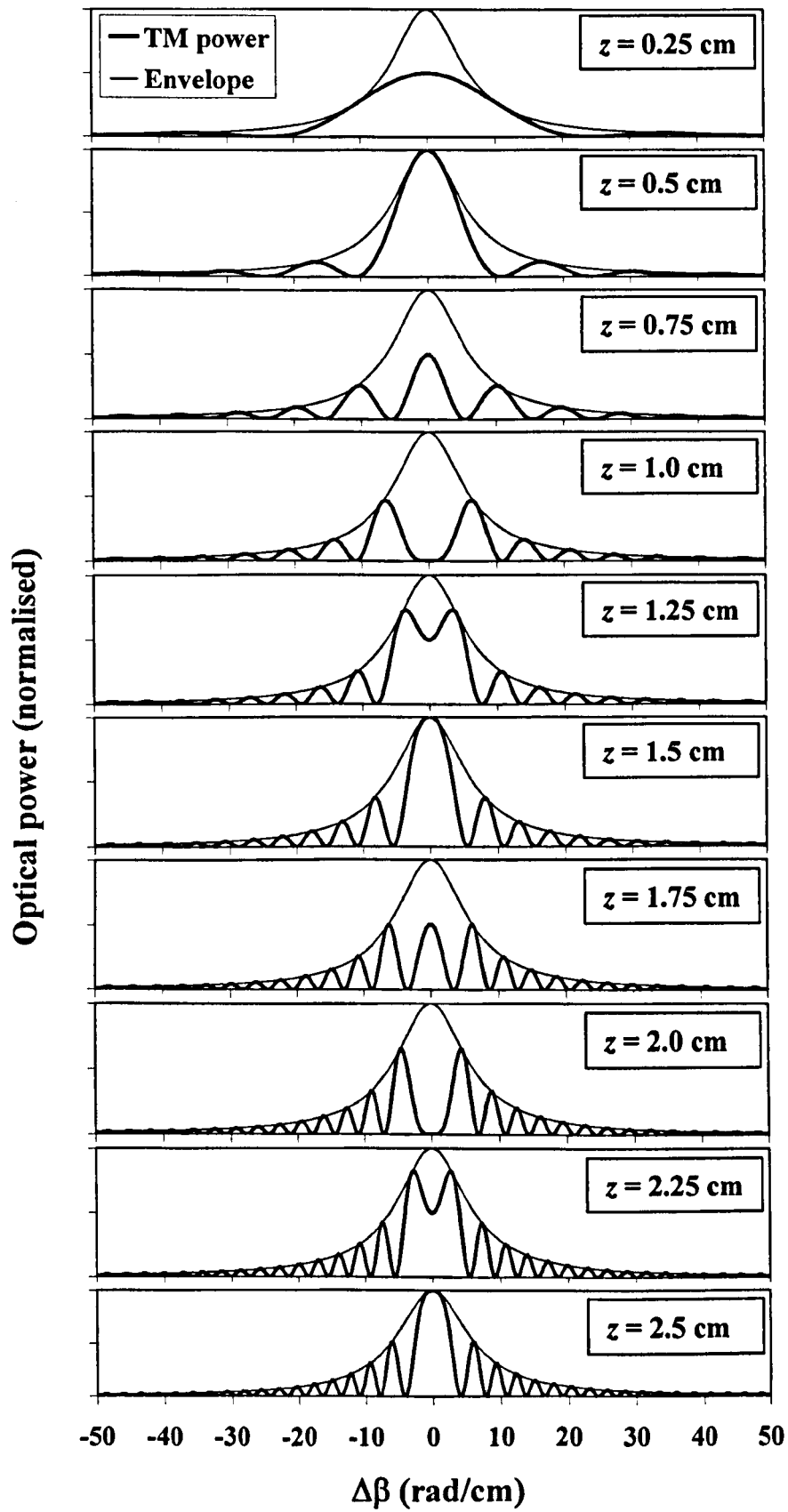


Fig. 2.7: Coupled-mode theory prediction of TM power versus  $\Delta\beta$  given a TE input, for a value of the coupling constant  $\kappa = \pi \text{ cm}^{-1}$ , through ten equally spaced values of length  $z$  up to 2.5 cm. The normalised envelope of maximum TM power is also shown.



## 2.6 The linear electrooptic effect in GaAs

The optical indicatrix or index ellipsoid describes the refractive index of a crystal for all polarisations, i.e. all directions of the optical electric field vector. Its radius gives the refractive index for a given direction. Using standard notation, it is given in general by [97]:

$$\left(\frac{1}{n^2}\right)_1 x^2 + \left(\frac{1}{n^2}\right)_2 y^2 + \left(\frac{1}{n^2}\right)_3 z^2 + 2\left(\frac{1}{n^2}\right)_4 yz + 2\left(\frac{1}{n^2}\right)_5 xz + 2\left(\frac{1}{n^2}\right)_6 xy = 1 \quad (2.6.1)$$

The Cartesian coordinate system is now defined for the specific case of the principal dielectric axes of the crystal as  $x$ ,  $y$  and  $z$  which run in the  $[100]$ ,  $[010]$  and  $[001]$  directions respectively [121]. GaAs is a cubic zinc blende crystal ( $\bar{4}3m$ ) [120], and is isotropic in the absence of an applied electric field. In this case, and for bulk material as opposed to a waveguide, the indicatrix reduces to:

$$\frac{x^2 + y^2 + z^2}{n^2} = 1 \quad (2.6.2)$$

which describes a sphere. In the presence of an external electric field equation (2.6.1) is modified by:

$$\Delta\left(\frac{1}{n_0^2}\right)_i = \sum_{j=1}^3 r_{ij} E_j \quad (2.6.3)$$

where  $j = 1$  to  $3$  gives  $x$ ,  $y$  and  $z$  respectively, and  $r_{ij}$  is a third rank tensor of the linear electrooptic coefficients, expressed by convention as a  $6 \times 3$  matrix [97]. Due to symmetry considerations, in GaAs the only non-zero coefficients are  $r_{41}$ ,  $r_{52}$  and  $r_{63}$ , which are all equal and have a value in the vicinity of  $-1.36 \times 10^{-12} \text{ mV}^{-1}$  at  $1500 \text{ nm}$  [106]. There are also quadratic and higher terms, but these are weak, and so are neglected. In the general case of an applied electric field with components  $E_x$ ,  $E_y$ ,  $E_z$ , the indicatrix becomes:

$$\frac{x^2 + y^2 + z^2}{n_0^2} + 2r_{41}yzE_x + 2r_{41}xzE_y + 2r_{41}xyE_z = 1 \quad (2.6.4)$$

The presence of mixed terms indicates that the index ellipsoid no longer describes a sphere, and that its major and minor axes are in general not aligned with the  $xyz$  axes. The crystal has become birefringent. It is always possible to define a new set of axes  $x'$ ,  $y'$  and  $z'$  which are aligned with the new principal dielectric axes, such that:

$$\frac{x'^2}{n_{x'}^2} + \frac{y'^2}{n_{y'}^2} + \frac{z'^2}{n_{z'}^2} = 1 \quad (2.6.5)$$

Only electric fields which are transverse to the direction of propagation are of interest. There are two relevant possibilities which are commonly used for GaAs waveguides:

propagation along  $[011]$  and propagation along  $[0\bar{1}1]$ . It will be assumed that the wafer epitaxy is grown on the  $(100)$  surface. For propagation along  $[0\bar{1}1]$ , a transverse field will have equal components in  $y$  and  $z$ . Inspection of equation (2.6.4) with  $E_y$  substituted for  $E_z$  reveals that  $y$  and  $z$  are interchangeable, i.e. the new ellipsoid is symmetric about the transverse plane. It is therefore apparent that one of the new dielectric axes must be parallel to the direction of propagation. This axis is labelled  $z'$ . A similar conclusion may be drawn for propagation along  $[011]$ . Given that only transverse field components will be applied, the components of the ellipsoid along  $z'$  can now be neglected. The resulting ellipse which forms a section through the ellipsoid in the plane  $z' = 0$ , which is also a section through the waveguide. The other two dielectric axes are normal to  $z'$ .

This analysis is now primarily concerned with the case of propagation along  $[011]$ , with which the universal polarisation controller device demonstration was made. This will be the case under consideration unless otherwise stated. A new axis  $v$  is defined to be directed horizontally across the waveguide, perpendicular to both  $x$  and  $z'$ . The axis directions are shown in Fig. 2.8. To obtain an equation for the ellipse in the plane  $z' = 0$ , the old axes are defined in terms of the new axes:

$$y = \frac{v}{\sqrt{2}} + \frac{z'}{\sqrt{2}} \quad z = \frac{z'}{\sqrt{2}} - \frac{v}{\sqrt{2}} \quad (2.6.6)$$

Substituting similarly for the applied field components, taking  $z' = 0$  for  $[011]$  propagation, and substituting in (2.6.4) gives the ellipse equation in which  $r_{41}$  is negative:

$$\frac{x^2}{n_0^2} + \frac{v^2}{n_0^2} - r_{41}v^2E_x - 2r_{41}xvE_v = 1 \quad (2.6.7)$$

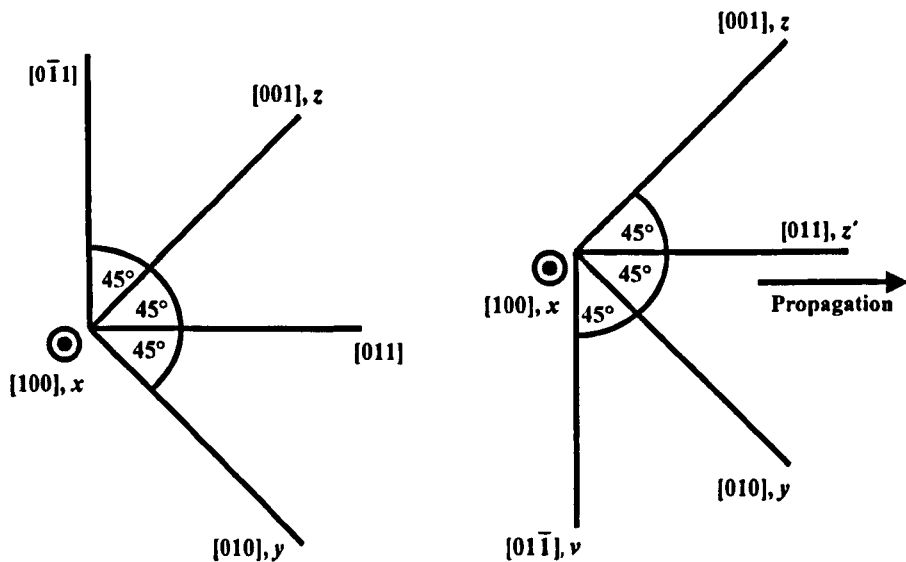


Fig. 2.8: Axis directions.

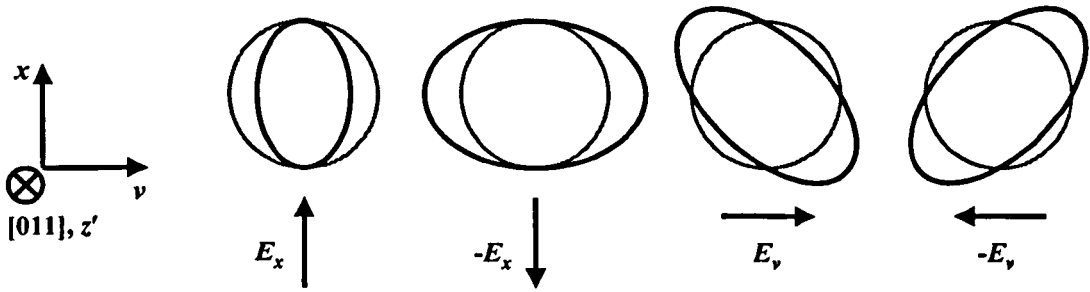


Fig. 2.9: Sections through the index ellipsoid for propagation along  $[011]$  in the presence of  $E_x$  and  $E_v$  applied field components.

Equation (2.6.7) describes the ellipse in terms of the axes along which the electric field vectors of the polarised modes of the waveguide are aligned. It is instructive to view the ellipses resulting from applied fields in the directions  $x$ , minus  $x$ ,  $v$  and minus  $v$ . These are shown in Fig. 2.9 for propagation along  $[011]$ , with the zero-field ellipse in grey. The ellipticity is greatly exaggerated in comparison with any practical example.

For the alternative case of propagation along  $[0\bar{1}1]$ , equation (2.6.7) is modified by reversal of sign of the third and fourth terms. The corresponding pairs of ellipses for positive and negative fields of each component are exchanged for each other. The axis  $v$  is again defined as being perpendicular to the direction of propagation and the  $x$  axis, and therefore corresponds to a different crystal axis from the  $[011]$  propagation case, as does  $z'$ . Fig. 2.9 indicates that combinations of  $E_x$  and  $E_v$  may be used to control the directions of the dielectric axes and the ellipticity or birefringence.

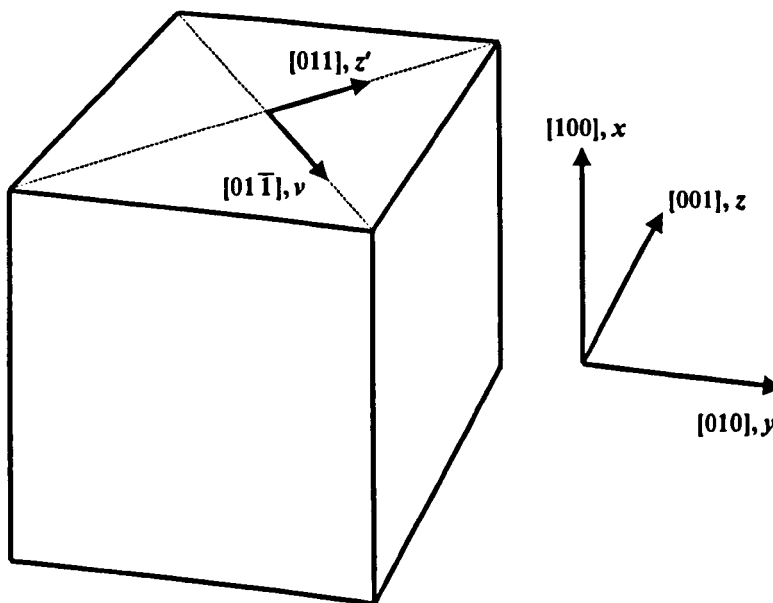


Fig. 2.10: Axis directions with respect to the cubic crystal structure of GaAs.

### Chapter 3: Device Fabrication and Experimental Methods

This chapter describes the experimental methods used in this work and the techniques used for the fabrication of experimental devices. Some sections are general, with specific detail provided later in the relevant experimental chapters.

#### 3.1 Device fabrication

Fabrication of devices was carried out by a number of colleagues at QinetiQ Malvern, to designs prepared by the author. Their contributions are stated in the acknowledgements section and are repeated in the relevant sections below. The steps involved are outlined in this chapter. Initially three test wafers were fabricated with different epitaxy designs, labelled P0, P1 and P2. A fourth wafer with a further epitaxy design was fabricated later, labelled P0a. The epitaxy designs are presented for reference in Table 3-I. The purpose of each design is discussed in the relevant experimental chapter.

Layer	Design P0		Design P1		Design P2		Design P0a		All
	Depth (μm)	Al fraction	Depth (μm)	Al fraction	Depth (μm)	Al fraction	Depth (μm)	Al fraction	Doping
Cap	0.1	0	0.1	0	0.1	0	0.1	0	Intrinsic
Upper cladding	1.2	0.2	1.2	0.3	1.2	0.3	1.2	0.2	Intrinsic
Core	2.0	0	0.95	0	0.5	0	2.4	0	Intrinsic
			0.1	0.5	0.3	0.085			
					0.4	0			
					0.3	0.085			
					0.95	0			
			0.5	0					
1 <sup>st</sup> lower cladding	0.2	0.2	0.2	0.3	0.2	0.3	0.3	0.2	Intrinsic
2 <sup>nd</sup> lower cladding	0.5	0.3	0.5	0.3	0.5	0.3	0.4	0.3	n+
3 <sup>rd</sup> lower cladding	3.8	0.06	3.6	0.09	3.6	0.09	3.6	0.055	n+
Substrate	650	0	650	0	650	0	650	0	Intrinsic

Table 3-I: Wafer specifications P0, P1, P2 and P0a. Layer depths, Al fractions and doping for the wafers fabricated for use in experiments. The required tolerance on Al fractions and layer depths was ±10%.

### **3.1.1 GaAs wafer epitaxial growth**

Three test wafers were grown to different epitaxial layer designs by Dennis Soley at QinetiQ Malvern by Molecular Beam Epitaxy (MBE) [108], [122]-[124]. The technique involves vaporisation of the required elements, gallium, arsenic, aluminium, and silicon, which is used for the n-type doping. The vapours pass over a GaAs substrate under a high vacuum and are deposited to form the epitaxial layers. The composition of the structure at a given depth is controlled by the rate of evaporation of each of the elements according to pre-defined calibrations. MBE is favoured for the low impurity concentrations obtained compared to other methods such as Metal-Organic Chemical Vapour Deposition (MOCVD). The consequence of this lower background doping is that there are fewer free carriers in the intrinsic semiconductor region, so that the voltage required to deplete through the structure is small, typically <1 V compared to several volts for MOCVD. The wafers were of 3" diameter, with a substrate thickness of 650  $\mu\text{m}$ .

### **3.1.2 Photolithographic mask design and production**

A polarisation test mask set was designed, containing a variety of test structures to investigate coupling mechanisms and mode index dependence. The mask set design was defined and drawn by the author as an electronic file in the GDS II standard, using a mask drawing programme written by John Heaton. It consisted of two masks for the definition of metal deposition and etch patterns. The masks were fabricated in chrome on crown glass by Compugraphics Ltd. A second mask set was later produced by the same methods.

### **3.1.3 Wafer processing**

Wafers P0, P1 and P2 were processed using the first mask set, while wafer P0a was processed using the second mask set. In each case the process was identical, consisting of single metal deposition and etch stages. The metallisation and etch regions were defined by patterning photoresist using ultraviolet photolithography, which was carried out by Brian Smith, Julia Guest, Helen Johnson and Peter Wilding, and etching was performed by Alan Hydes.

Metal deposition was the first processing step. Positive photoresist was spun onto the wafer surface and exposed to UV with the metallisation mask applied, aligned to the appropriate crystal axis as indicated by the positions of the major and minor flats located on the wafer edge. These may be observed in Fig. 3.1. The flats run parallel to the [011] direction or equivalent. Following removal of exposed areas of resist by immersion in developer and

rinsing in water, the patterned wafer was placed in a metal evaporator for the deposition of a  $0.5\ \mu\text{m}$  thick layer of gold over the whole surface, preceded by thin layers of titanium and palladium to ensure adhesion to the semiconductor. The wafer was then immersed in acetone to dissolve the photoresist and thus float off metal deposited on top of it. This is commonly called a “lift-off” process.

A similar resist patterning procedure was used with the waveguide etch mask, which was aligned to alignment markers formed in metal at various points across the wafer. The deep-etched waveguides were formed by Reactive Ion Etching (RIE) of the exposed regions of semiconductor, using an Oxford Instruments Plasmalab System 90 machine. This machine operates using a 15 MHz plasma in  $\text{SiCl}_4$  in which the GaAs wafer is negatively charged. Positively charged ions accelerate through the discharge over several RF cycles before combining with Ga and As to form volatile chlorides which are pumped away. The target etch depth of  $4\ \mu\text{m}$  was checked by Dektak stylus measurement.

Removal of photoresist completed the process, yielding the finished wafer as depicted in Fig. 3.1. In order to cleave out individual devices, diamond scribing was performed using a Karl Suss skip scribe. Device cleaving was performed by hand by the author.

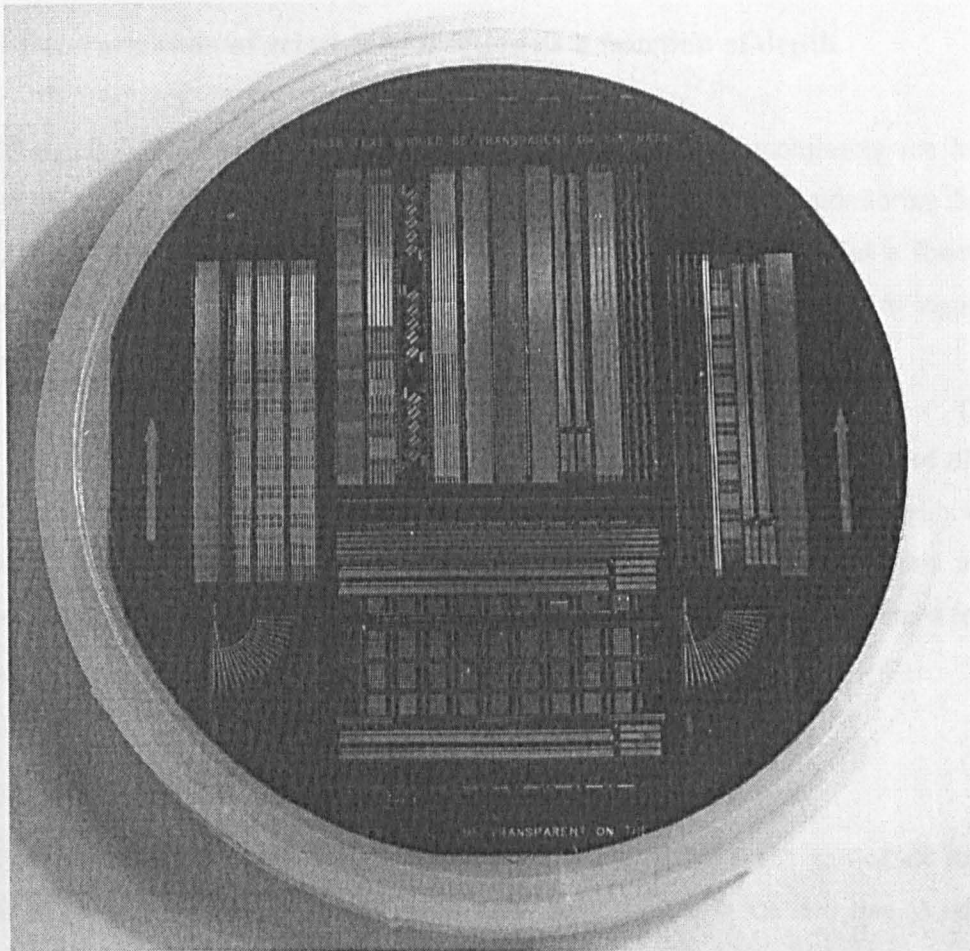


Fig. 3.1: A processed GaAs wafer, 3" diameter.

The highly directional etching process results in near-vertical waveguide side walls. However, it had been observed that at the extreme edges of a 3" diameter wafer, waveguides running tangentially to the wafer edge exhibited a parallel side-wall slant, resulting in a parallelogram-shaped cross section, leaning towards the centre of the wafer. This was attributed to the shape of the discharge at its extremes, and it was allowed to persist during the fabrication of devices for this work. The matter is discussed further in the experimental chapters.

## 3.2 Material characterisation

The epitaxial layer structures of wafers P0, P1 and P2 were characterised to determine whether or not the layer thicknesses and Al fractions were within the required tolerances. This was carried out by Secondary Ion Mass Spectroscopy (SIMS) by Dr Andrew Simons at QinetiQ Malvern. SIMS is a destructive technique in which sputtering of a sample is performed by a focused ion beam, while the composition of the removed material is analysed by mass spectroscopy [125]-[129]. Small unetched areas were reserved on each wafer for this purpose.

### 3.2.1 Determination of relative Al fraction as a function of depth

The Ga signal (measured in counts per second) is measured by monitoring the level of (69Ga+133Cs) positive secondary ions, and the Al signal is measured by monitoring the level of (27Al+133Cs) positive secondary ions [129]. The absolute Al fraction as a function of depth can be determined due to the relationship between the Ga signal and Al signal as a function of Al fraction. The Ga signal  $Ga_c$  and Al signal  $Al_c$  are given by:

$$Ga_c = Ga_0(1-x), \quad Al_c = Al_1x \quad (3.1)$$

where  $x$  is the Al fraction,  $Ga_0$  is the value of  $Ga_c$  when  $x = 0$  and  $Al_1$  is the value of  $Al_c$  when  $x = 1$ . The values of  $Ga_0$  and  $Al_1$  are dependent on the experimental conditions. Calibration of their values is required to take account of the variation in ion yield from different material compositions, which is termed the matrix effect [128]. The Al fraction is determined from the ratio of the Ga and Al signals, which yields the relationship:

$$x = \left[ 1 + \left( \frac{Ga_c Al_1}{Al_c Ga_0} \right) \right]^{-1} \quad (3.2)$$

$Ga_0$  is obtained from the measurement of the value of  $Ga_c$  in the GaAs part of the structure.  $Al_1$  can be determined directly if there is an AlAs layer present in the structure. As this was not the case, a value was obtained using the assumption that the upper cladding Al fraction

was correct as specified. For this reason, the Al fraction data obtained can only be considered relative to the upper cladding composition, with the absolute values strictly being suitable for indication only. The growth technique used has been shown to reliably produce Al compositions of 0.2 and 0.3 within the quoted tolerance of  $\pm 10\%$ , using characterisation methods including photoluminescence (PL) measurements.

### **3.2.2 Determination of layer depths**

The layer depths were obtained from a measurement of the total depth sputtered during analysis, using a Sloane Dektak stylus profilometer, and the count rate data modified to take account of the non-uniform sputter rate with Al fraction. AlGaAs sputters at a slower rate than GaAs, according to the empirical relation [129]:

$$R = 1 - 0.34x \quad (3.3)$$

### **3.2.3 Results**

The measurements of Al fraction are plotted versus depth for wafers P0, P1 and P2 in Figs. 3.2a to 3.2c respectively. The corresponding secondary ion count rate is plotted on the second vertical axis. By comparison with the design specifications given in Table 3-I, it is shown that the layer thicknesses are within the required tolerance of  $\pm 10\%$ . The relative Al fractions are also shown to meet this tolerance. Although this does not demonstrate that the absolute values of the Al fractions are within the specification, it is suggestive that the MBE growth process used was accurately calibrated.



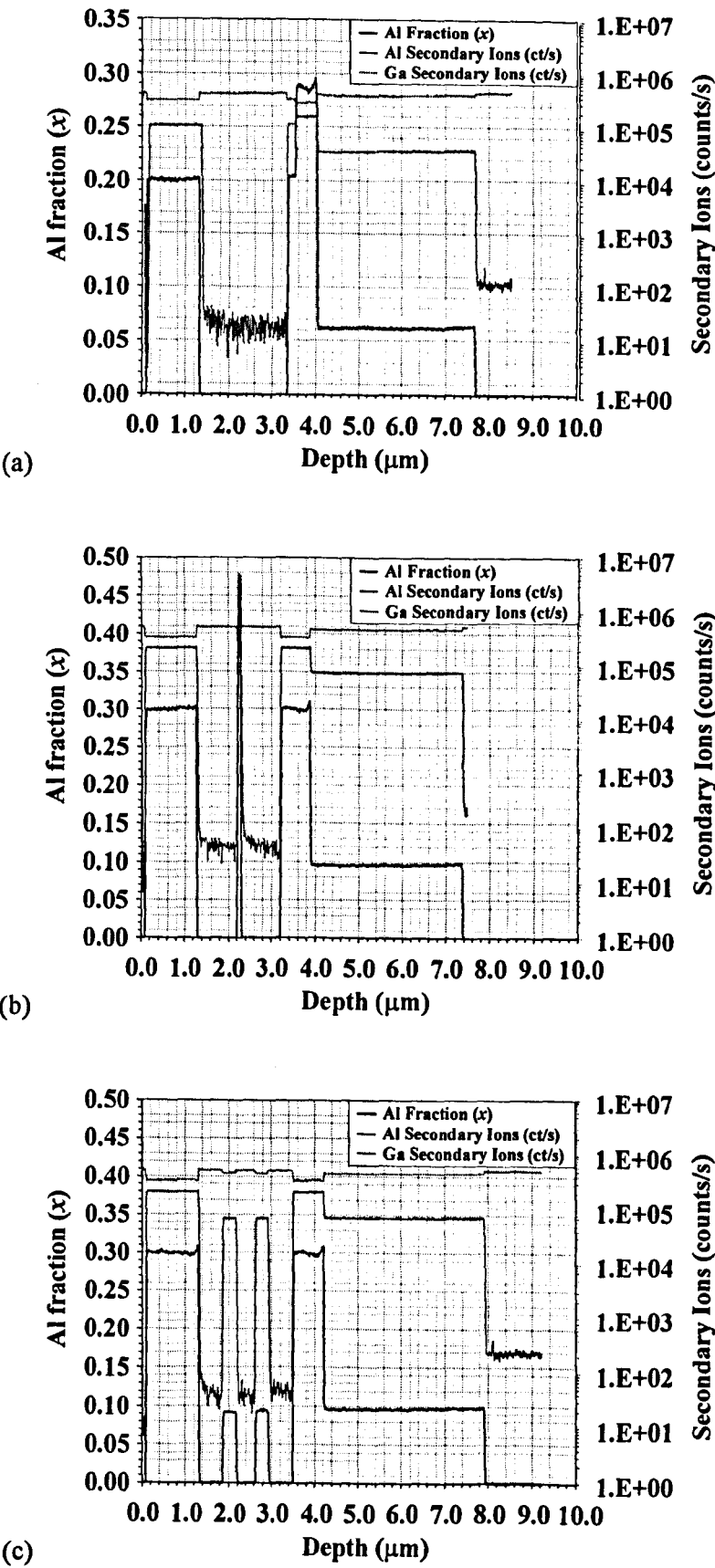


Fig. 3.2: Al fraction versus epitaxy depth measured by SIMS: (a) wafer P0, (b) wafer P1, (c) wafer P2. Measured secondary ion count rates are plotted on the second vertical axis.

### 3.3 Optical testing

A schematic diagram of the experimental setup is shown in Fig. 3.3. The light source consisted of a fibre-coupled semiconductor laser operating at a wavelength of 1550 nm, which was amplified by an Erbium Doped Fibre Amplifier (EDFA). The power coupled into the device under test was typically 10 mW. An in-fibre polarisation controller was used to correct variations in the polarisation state at the exit from the fibre, due to environmental variations. The collimated output from the fibre was directed through a Glan-Taylor polariser to ensure 50 dB purity of the chosen input polarisation. Light was coupled into waveguides by a  $\times 20$  microscope objective lens, and the output was collimated by a second  $\times 20$  microscope objective lens. Analysis of the output was conducted using a second Glan-Taylor polariser and a large area InGaAs p-i-n diode detector connected to an oscilloscope, which provided temporal output signal data. The output profile was observed using a vidicon camera and monitor, while the power was sampled and directed to the detector by a pellicle beam splitter at near-normal incidence. For the testing of electrooptic waveguides and devices, the bond pads were contacted electrically using probes fitted with 5  $\mu\text{m}$  needles, positioned using three-axis translation stages.

The specific experimental methods used are described below. Minor variations to the basic setup described above and to the general experimental methods are detailed in the relevant experimental chapters.

#### 3.3.1 Mode angle measurements

When light is coupled accurately into one polarised waveguide mode it will retain its polarisation state during propagation. A method was devised to determine the mode angles of each waveguide by finding the input linear polarisation states that were preserved to the highest degree. To measure the degree of preservation for a given input state, the output power was first measured with the input and output polarisers set to the same angle. This was then repeated with the output polariser turned through  $90^\circ$ , and the extinction ratio of the preserved component to the orthogonal component was calculated. Measurements were obtained for linear input states throughout the  $180^\circ$  range of angles. For each guide width, the extinction was found to have two peaks separated by  $90^\circ$ , which were taken to give the mode angles. An example of the result for one waveguide is shown in Fig. 3.4. For these measurements, Fabry-Pérot resonance was suppressed by using a source with a coherence length shorter than the round-trip optical length of the cavity formed by the waveguide.

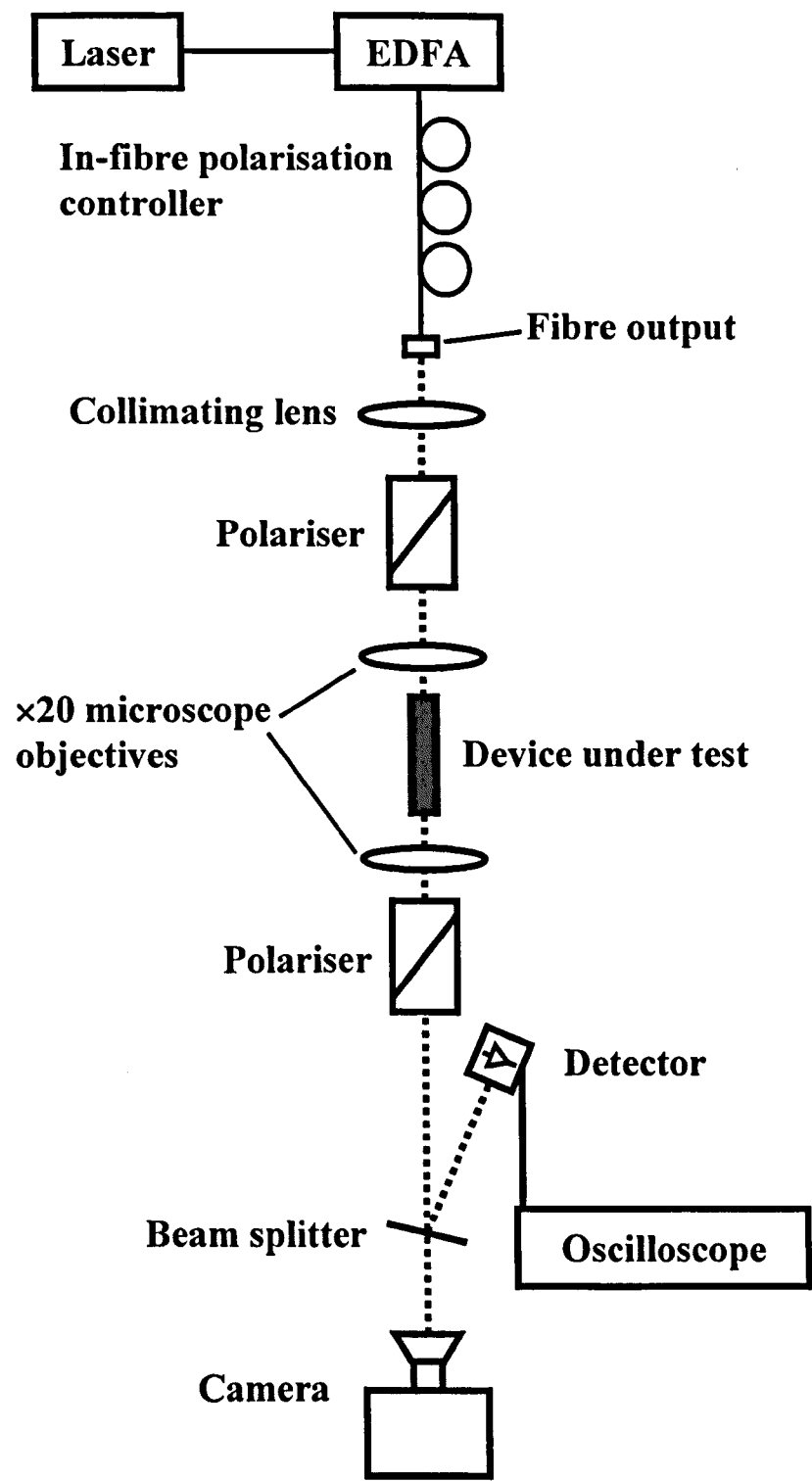


Fig. 3.3: Schematic diagram of the experimental setup.

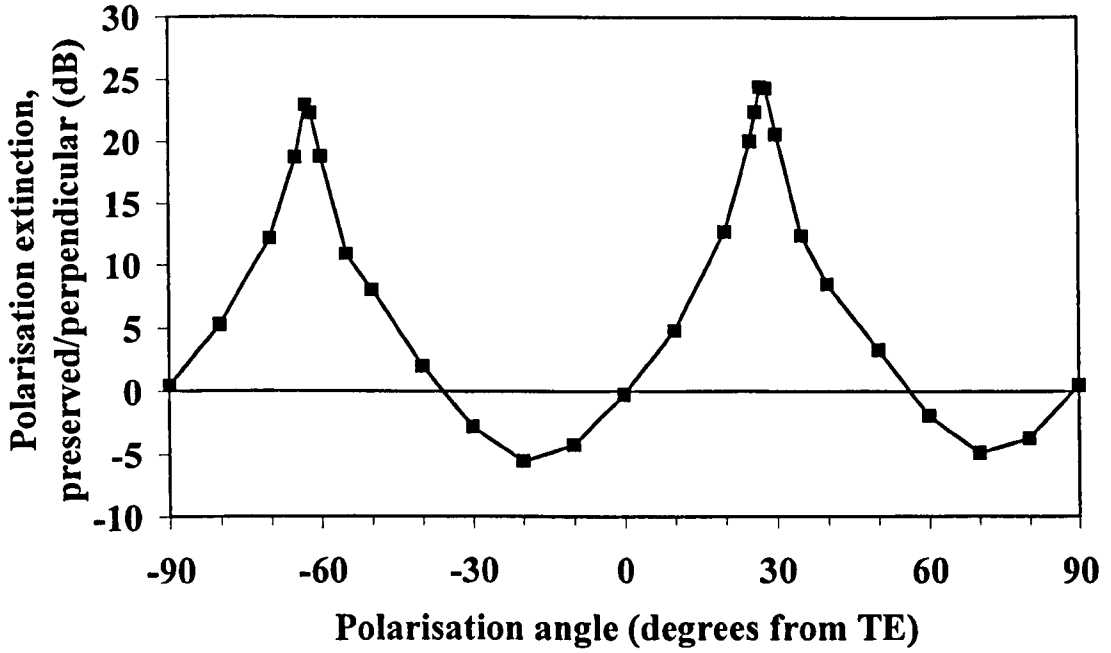


Fig. 3.4: An example of a mode angle measurement, carried out on a 3.55  $\mu\text{m}$ -wide asymmetric waveguide, indicating mode angles of  $-63^\circ$  and  $27^\circ$ .

### 3.3.2 Effective index difference measurements

For the measurement of the difference between the effective indices of the polarised modes of a waveguide, a method offering sufficient accuracy to distinguish the expected features close to the phase-matching guide width was required. A novel technique utilising the strong Fabry-Pérot resonance exhibited by the waveguides was used. This resulted from the absence of anti-reflection coatings on the cleaved facets, the large power reflection coefficient at the GaAs – air interface ( $R \sim 0.3$ ), and low optical loss in the waveguides. Typically, fringe contrasts of 2 or 3 were measured. The input polarisation was set to excite both orthogonal modes equally, while the output polariser was replaced with a polarising beam splitter which was adjusted to pass one of the mode outputs at the measured mode angle. A second detector was introduced to measure the light rejected by the polariser, which contained only the output from the orthogonal mode. The device length was altered by a few wavelengths through thermal expansion, obtained by radiative heating using a fibre-coupled lamp. This produced a set of Fabry-Pérot fringes in each signal, with a period determined by the rate of heating, which was effectively linear. The two fringe sets exhibited a temporal separation, relative to the period, because of the difference between the optical lengths traversed by the two modes. Assuming that only one cavity round trip need be considered, the index difference is given by:

$$\Delta n = \frac{\lambda_0}{2L} \left( \frac{t}{T} \right) \quad (3.4)$$

where  $L$  is the device length,  $\lambda_0$  is the free space wavelength, and the ratio  $(t/T)$  is the temporal separation of the two fringe sets divided by the fringe period. In each case two lengths of guide were measured, to reduce the number of possible integer values to be added to the fringe offset, measured as a fraction of the period. This was sufficient to allow the correct integer to be determined by inspection of the data. For a round trip length of 2 cm, an index difference of  $10^{-6}$  may be resolved using this method.

For some waveguides it was necessary to use a very short length, as little as 1 mm. In this case the radiative heating technique provided insufficient Fabry-Pérot resonance cycles to allow a measurement of phase difference as a fraction of period. An alternative was obtained by scanning the wavelength from 1448 nm to 1552 nm. This function was available as a feature of the tunable laser used in the experiments.

The amplitudes of the Fabry-Pérot fringes were also measured to enable the calculation of the optical losses of the modes for comparison, as described in section 3.3.4.

### 3.3.3 Direct measurements of polarisation conversion

Direct measurements of polarisation extinction were made on waveguides. TE polarised light was coupled into the guides, while horizontal and vertical output components were measured. In passive waveguides, the signal levels were averaged over the Fabry-Pérot cycle. For voltage-dependent measurements in electrooptic waveguides, the Fabry-Pérot resonance was suppressed as described in section 3.3.1.

### 3.3.4 Optical loss measurements

The optical loss per unit length of the fundamental TE and TM modes of passive waveguide sets of various guide widths were measured using the Fabry-Pérot resonance technique described by Walker [130]. This is based on the strong reflection that occurs at uncoated cleaved waveguide end facets. The power reflection coefficient  $R$  was taken to be 0.295. With a continuous-wave optical input applied to the device, the waveguide length was altered by a few wavelengths through thermal expansion, obtained by radiative heating using a fibre-coupled lamp. This produced a set of temporal fringes in the output signal, which was measured using a photodiode connected to an oscilloscope. The loss in dB per unit length is then obtained from the inverse of the fringe visibility, given by the ratio of the minimum and maximum transmissions,  $K$ :

$$\Gamma = -\frac{10}{L} \log_{10} \left[ \frac{R(1 + \sqrt{K})}{1 - \sqrt{K}} \right] \quad (3.5)$$

## Chapter 4: Polarisation Conversion in Passive Waveguides

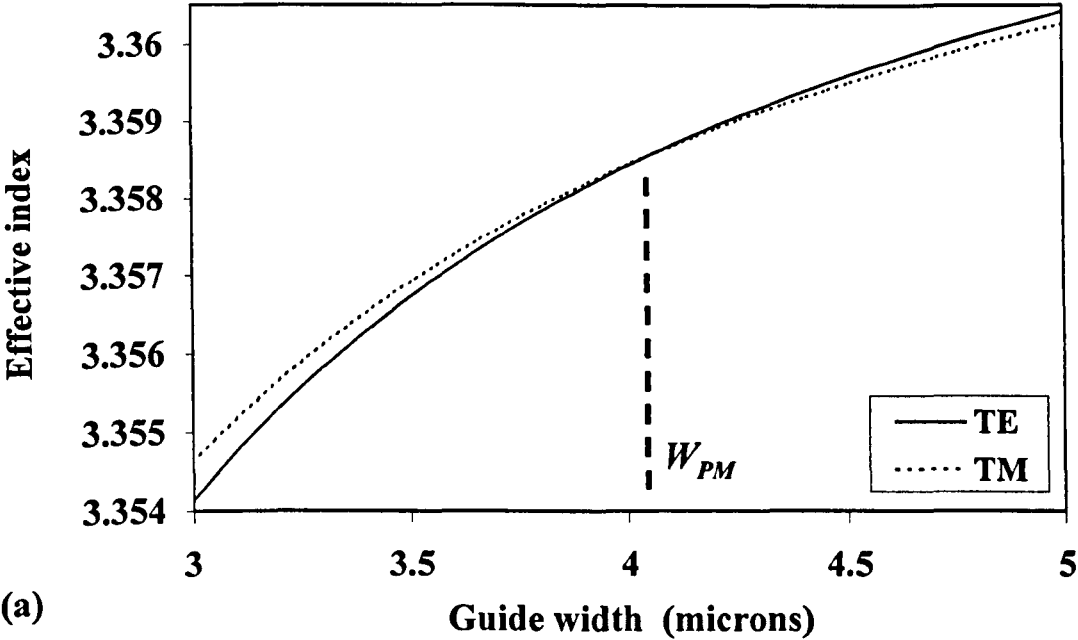
This chapter presents an experimental investigation of polarisation conversion in passive dielectric optical waveguides. The effect due to process-dependent features of waveguide cross-section geometry, in particular asymmetry resulting from non-vertical etching, is investigated. The results are compared with theoretical simulations to determine the physical origin of the conversion and to provide the basis of a simplified model for the behaviour.

### 4.1 Theory of polarised mode propagation

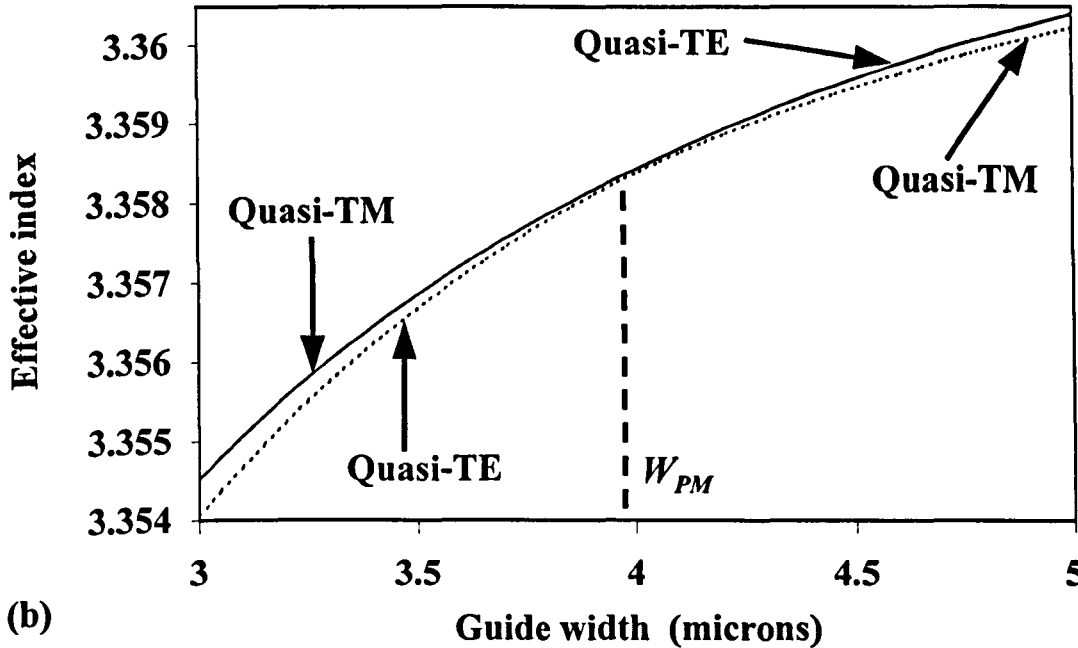
By convention, optical electric fields parallel to and perpendicular to the horizontal plane of the epitaxial layers are referred to as transverse electric (TE) and transverse magnetic (TM) polarisations respectively. Optical modes in a dielectric waveguide of rectangular cross section are hybrid in nature, having electric and magnetic field components along three axes. Also, the nett directions of the  $E$  and  $H$  vectors are not completely uniform across the mode. A thorough theoretical analysis requires a vectorial numerical approach such as the vector finite element method described in references [75]-[76], [116]. The FIMMWave software package also provides vectorial simulations using the film mode matching (FMM) method.

#### 4.1.1 FMM method simulations

Three important results of FIMMWave simulations for an example waveguide design are shown in Figs. 4.1 and 4.2. For reference, the layer thicknesses and refractive indices used in these simulations are given in Table 4-I [102], [104]-[105], [107]. The effective indices of the fundamental modes are plotted against guide width in Fig. 4.1a. The corresponding plot in Fig. 4.1b is for a waveguide with asymmetry in the form of a small parallel side-wall slant of  $5^\circ$ , resulting in a parallelogram-shaped cross section. Angled boundaries were approximated by a series of right-angled steps in FIMMWave. In symmetric waveguides the modes are dominated by TE and TM components respectively, and are only weakly hybrid. Depending on the design of the epitaxy, there may be a guide width at which the difference between the indices goes to zero. At this phase-matching guide width,  $W_{PM}$ , degenerate modes with equal field components in the horizontal and vertical directions can be defined (i.e. the principal polarisation directions are  $+45^\circ$  and  $-45^\circ$ ). However, this is of no practical consequence for polarisation conversion because the indices are identical. In effect, any polarisation state will propagate unchanged, and it may be argued that TE and TM modes still exist.



(a)



(b)

Fig. 4.1: FIMMWave FMM method simulations of modal effective index versus guide width for wafer specification P0 (given in Table 4-I) with a wavelength of 1550 nm.  
(a) Symmetric cross section waveguides, (b) asymmetric cross section waveguides.

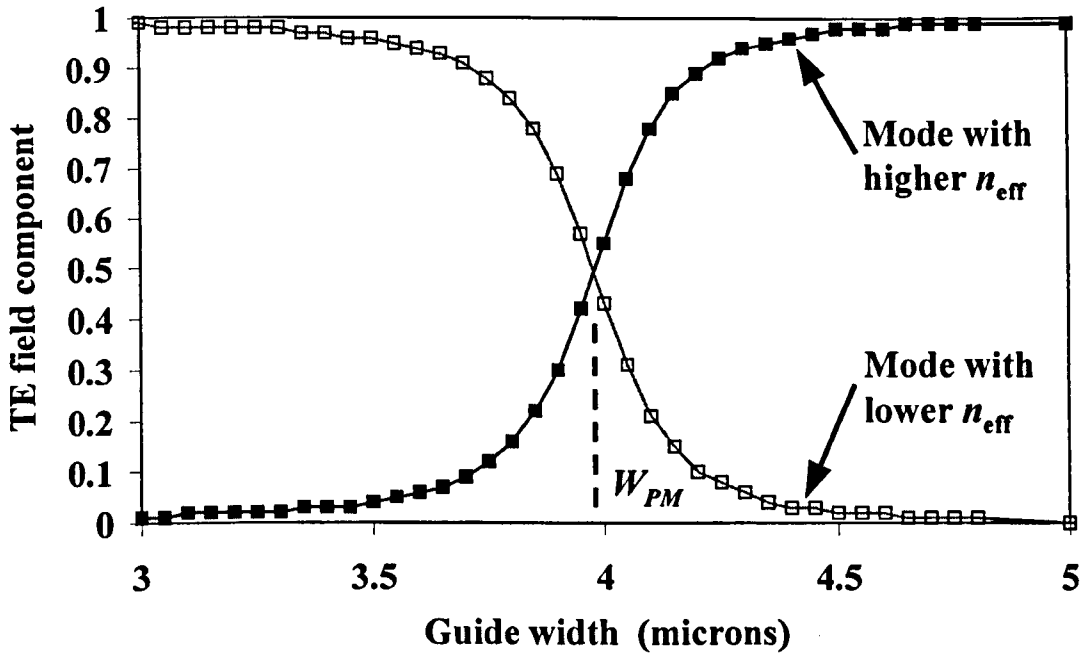


Fig. 4.2: FIMMWave FMM method simulations of horizontal optical electric field component versus guide width for both modes in asymmetric cross section waveguides. The field parameter is defined as the fraction of the Poynting vector with horizontal field orientation.

In guides with asymmetric cross section, the hybrid nature of the modes becomes prominent. The two modes can be tracked continuously through the range of guide widths. They are referred to here as quasi-TE and quasi-TM depending on which field component is dominant. One mode has horizontal and vertical field components with the same sign, while in the other they have opposite signs. The mode which is quasi-TM for widths narrower than  $W_{PM}$  has the larger effective index. The horizontal optical electric field component of both modes of asymmetric cross section waveguides is plotted for the same range of guide widths in Fig. 4.2. The field parameter is defined as the fraction of the Poynting vector with horizontal field orientation. The figure shows that, as the guide width increases, the non-dominant field component increases in magnitude until it becomes dominant in guides wider than  $W_{PM}$ . In this case the modes are never degenerate because the index difference does not go to zero. However, at the closest approach of their indices the two modes again have equal field amplitude components in the horizontal and vertical directions. This occurs at  $W_{PM}$ , which is referred to as the phase-matching width throughout for consistency. This fact is indicated by the VFEM simulations reported in [75]-[76]. It is noted that in Fig. 4.1 the phase-matching width is not identical for the symmetric and asymmetric cases. This is assumed to be partly an artefact of the FIMMWave simulations, caused by the approximation of the angled boundaries by a series of right-angled steps. By contrast, oblique boundaries can be defined in the VFEM model, which is therefore better suited to this problem.



In the general case of a waveguide with significantly hybrid modes, a purely TE input polarisation will excite both modes which will then propagate with different phase, resulting in polarisation conversion. Complete coupling from a TE input state to a TM output state can only occur when the guide width is  $W_{PM}$ , so that the principal polarisation directions of the modes are  $+45^\circ$  and  $-45^\circ$ , and both modes are excited equally. The coupling length is then determined by the index difference, which depends on the degree of asymmetry.

The facility to predict quantitatively the polarisation behaviour of specific waveguide designs is of value to the designer. While the effects can be modelled directly using vectorial methods such as VFEM or FMM, an alternative approach involves the use of the coupled-mode theory. A limitation of a coupled-mode description is that a value for the coupling constant must be obtained, either experimentally or using a sophisticated model. The latter route would negate the main benefit of the approach, which is that only the index relationship for non-hybrid modes is required. This situation may be modelled using non-vectorial techniques such as the effective index method. However, the ability of any technique to model accurately the TE-TM mode index relationship is limited by the fidelity of the refractive index data used in the model.

Layer	Depth ( $\mu\text{m}$ )	Al fraction	Doping	Refractive indices			
				Modified Afromowitz (FMM method)	Adachi	Afromowitz	Gehrsitz
Cap	0.1	0	Intrinsic	3.376946	3.488145	3.376946	3.595318
Upper cladding	1.2	0.2	Intrinsic	3.281172	3.416816	3.275124	3.436779
Core	2.0	0	Intrinsic	3.376946	3.488145	3.376946	3.595318
1 <sup>st</sup> lower cladding	0.2	0.2	Intrinsic	3.281172	3.416816	3.275124	3.436779
2 <sup>nd</sup> lower cladding	0.5	0.3	n+	3.232520	3.369271	3.225046	3.364820
3 <sup>rd</sup> lower cladding	3.8	0.06	n+	3.348452	3.469716	3.346181	3.552271
Substrate	650	0	Intrinsic	3.376946	3.488145	3.376946	3.595318

Table 4-I: Wafer specification P0. Layer depths, doping, Al fractions, and the corresponding refractive index values for four different sets of published data, which are given in [102], [104], [105], and [107]. The modified Afromowitz data were used for the FMM method simulations.

There is sufficient variation in the empirical formulae quoted for AlGaAs compositions in the literature to place doubt on quantitative predictions of  $W_{PM}$  and the index relationship, as they are critically dependent on the index contrast. This variation is apparent in the refractive index values given in Table 4-I, obtained using several sets of published index data for the wafer P0 layer structure. The refractive index values used in the FMM simulations are provided by a slightly modified [107] version of the data published by Afromowitz et al [102]. This formula has been verified for the design of low-loss, single-mode waveguides for a range of near-infrared wavelengths, and is built into the QinetiQ in-house models developed by John Heaton. Alternative index data sets are provided by Adachi et al [104], the unmodified Afromowitz data, and Gehrsitz et al [105]. The modal effective indices of symmetric waveguides were modelled using the effective index method for all four sets of index data given in Table 4-I to investigate the sensitivity of  $W_{PM}$  to the index contrast and the uncertainty in the simulations resulting from the variation in available index data. The results are presented in section 4.3.

In addition to reporting demonstrations of the principles shown qualitatively by rigorous simulations, this chapter aims to provide a quantitative experimental benchmark for the polarisation behaviour of a typical waveguide epitaxy design. The index relationship for this epitaxy is measured for TE/TM modes, and for hybrid modes for a particular side-wall slant angle. The coupling constant for use in coupled-mode simulations is also determined experimentally for the same slant angle example. The main parameters of a simple epitaxy design affecting the polarisation behaviour are the core composition, the upper and lower cladding compositions, and the core thickness. The wafer epitaxy design given in Table 4-I was used for all modelling and experimental work described in this chapter. It was chosen as a simple design which is typical of designs that may be used for deep-etched waveguides.

Further FMM method simulations were carried out to quantify the predicted polarisation behaviour of the test epitaxy design. The minimum index difference values were obtained at phase matching, as a function of side-wall slant angle. The coupling length and coupling constant were calculated from the index difference at phase matching, given respectively by:

$$z_c = \frac{\lambda_0}{2\Delta n} \quad (4.1)$$

$$\kappa = \frac{\pi\Delta n}{\lambda_0} \quad (4.2)$$

The coupling constant is plotted versus slant angle in Fig. 4.3, with the index difference at phase matching indicated for the same data points on the second vertical axis. The coupling length is plotted versus slant angle in Fig. 4.4. The simulations show that significant polarisation conversion can result from a small asymmetry in the waveguide cross section, for

example a parallel side-wall slant of 1° corresponds with a coupling constant of 23 m<sup>-1</sup> and complete coupling from TE to TM in a length of 71 mm for the phase-matching guide width of 4.1 μm. The figures for a 5° slant are 95 m<sup>-1</sup> for the coupling constant and a coupling length of 16.5 mm.

Two simplified models for the description of the polarisation state during waveguide propagation are described below.

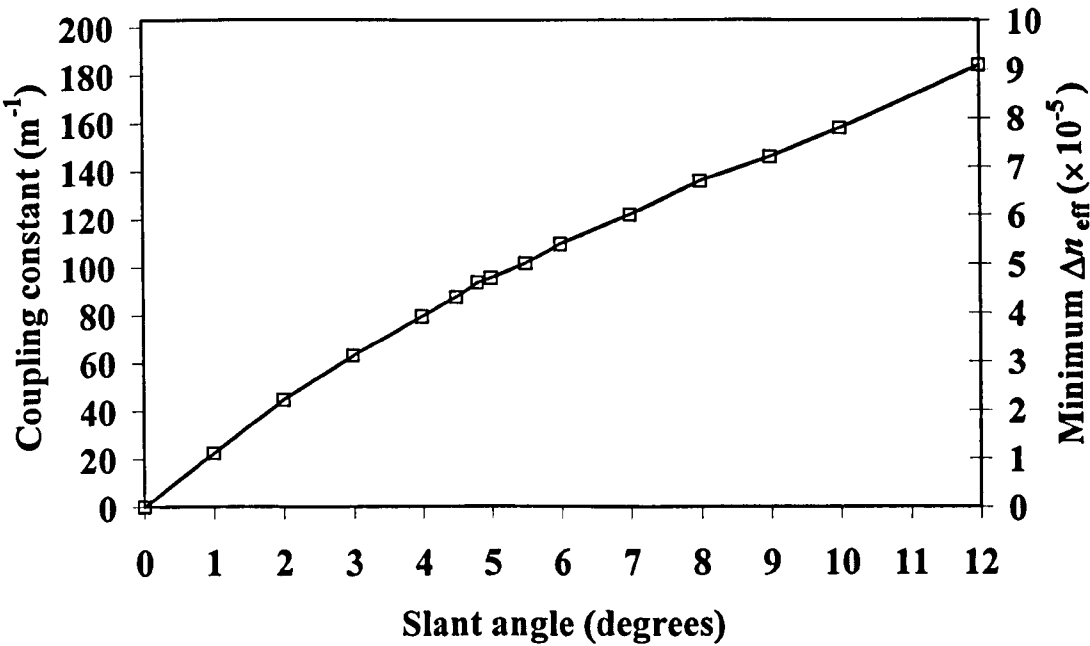


Fig. 4.3: FMM method simulations of coupling constant versus slant angle, with index difference at phase matching on the second vertical axis.

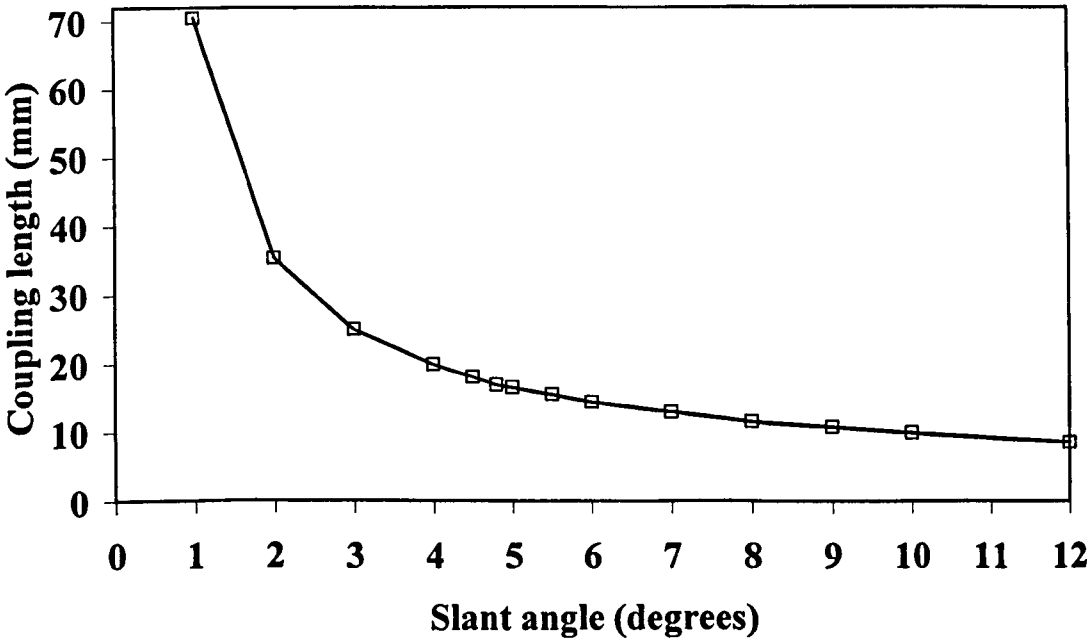


Fig. 4.4: FMM method simulations of coupling length versus slant angle.

### 4.1.2 Elliptical polarisation analysis

The term “mode angle” is used here to describe the nett direction of the electric field of the mode in the plane of the waveguide cross section, with respect to the horizontal axis. We consider two orthogonal waveguide modes  $A$  and  $B$  with  $E$  field directions at angles  $\theta_A$  and  $\theta_B$  from the horizontal and effective indices  $n_A$  and  $n_B$  respectively, and a free-space wavelength  $\lambda_0$ .  $\theta_B$  may be eliminated as it is always equal to  $\theta_A$  minus  $90^\circ$ . The direction of the  $E$  field is assumed to be spatially uniform. Given the mode angles, the difference between their effective indices, and the relative initial power in each mode, the light may be characterised as having an elliptical polarisation state which changes during propagation.

If the input power is  $P_0$ , with TE polarisation, the power coupled into modes  $A$  and  $B$  respectively is given by:

$$P_{A0} = P_0 \cos^2 \theta_A, \quad P_{B0} = P_0 \sin^2 \theta_A \quad (4.3)$$

Assuming that the propagation losses of the modes are equal, their electric fields as functions of propagation length  $z$  are given by equation (4.4). In the context of these passive waveguides,  $z$  does not denote a specific crystal axis.

$$E_A = E_{TE0} \cos \theta_A e^{\frac{i2\pi n_A z}{\lambda_0}}, \quad E_B = E_{TE0} \sin \theta_A e^{\frac{i2\pi n_B z}{\lambda_0}} \quad (4.4)$$

$E_{TE0}$  is the initial horizontal field. The horizontal component of the resultant electric field as a function of  $z$  is then given by:

$$E_{TE}(z) = E_{TE0} \cos^2 \theta_A e^{\frac{i2\pi n_A z}{\lambda_0}} + E_{TE0} \sin^2 \theta_A e^{\frac{i2\pi n_B z}{\lambda_0}} \quad (4.5)$$

The power in the TE state, as analysed by a polariser after propagation along length  $z$ , is given by the square of the modulus of the TE field. Following a similar treatment for the TM component, an expression may be obtained for the expected polarisation extinction ratio in decibels, which is given by:

$$\text{Polarisation extinction} = 10 \log_{10}(P_{TE}/P_{TM}) \quad (4.6)$$

### 4.1.3 Coupled-mode theory

A coupled-mode approach is useful for describing many problems involving energy exchange between modes. The approach requires the assumption that purely TE and TM modes propagate, while coupling between the two is permitted in the presence of a coupling mechanism. The coupled-mode theory was described in chapter two, including solutions to the coupled-mode differential equations to give the TE and TM mode amplitudes as functions

of propagation length  $z$ , coupling constant  $\kappa$  which describes the strength of the coupling mechanism, and  $\Delta\beta$ , which is the difference between the TE and TM propagation constants.

In order to calculate the expected polarisation extinction from the solutions of the coupled-mode equations given in section 2.5, values for  $\kappa$  and  $\Delta\beta$  are required. These are obtained from measurements in the experimental section of this chapter.

## 4.2 Experiments

### 4.2.1 Experimental device design and fabrication

Experiments were carried out on waveguides fabricated on a 3" diameter wafer with epitaxy design P0, which is given in Table 4-I. A general description of the techniques used for wafer and waveguide design and fabrication is given in chapters two and three. The epitaxy was chosen as an example of a simple design, typical of those suitable for use with deep-etched waveguides. It was designed to support the fundamental modes with low loss, while allowing higher order modes to leak into the substrate for guides with widths in the range  $\sim 3\text{--}5\text{ }\mu\text{m}$  [107]. Sets of straight passive waveguides with widths of  $1.0\text{ }\mu\text{m}$  to  $7.0\text{ }\mu\text{m}$  in  $0.05\text{ }\mu\text{m}$  intervals were defined, with lengths of up to 3 cm. The wafer was etched to a depth of  $4\text{ }\mu\text{m}$  by Reactive Ion Etching (RIE). The RIE machine was set up to give a non-uniform plasma near the edge of the wafer. The end facets of waveguides positioned near the centre of the wafer are shown in a scanning electron micrograph in Fig. 4.5a. The guides show the characteristic near-rectangular profile obtained from a dry-etch process. Fig. 4.5b shows the corresponding facets for waveguides formed near to and running tangentially to the wafer edge. A near-parallel side-wall slant of about  $5^\circ$  is apparent. This is in contrast with the waveguides in Fig. 4.5a which have symmetry about the vertical axis.

### 4.2.2 Experimental methods

Experiments were carried out on symmetric and asymmetric sets of waveguides to obtain the mode angles and the difference between their effective indices, and to measure polarisation conversion directly. For the purpose of elliptical polarisation analysis the absolute values of the indices are not required. The asymmetric waveguide set was cleaved successively to several different lengths and a measurement was obtained for each. The methods used are described in chapter three.

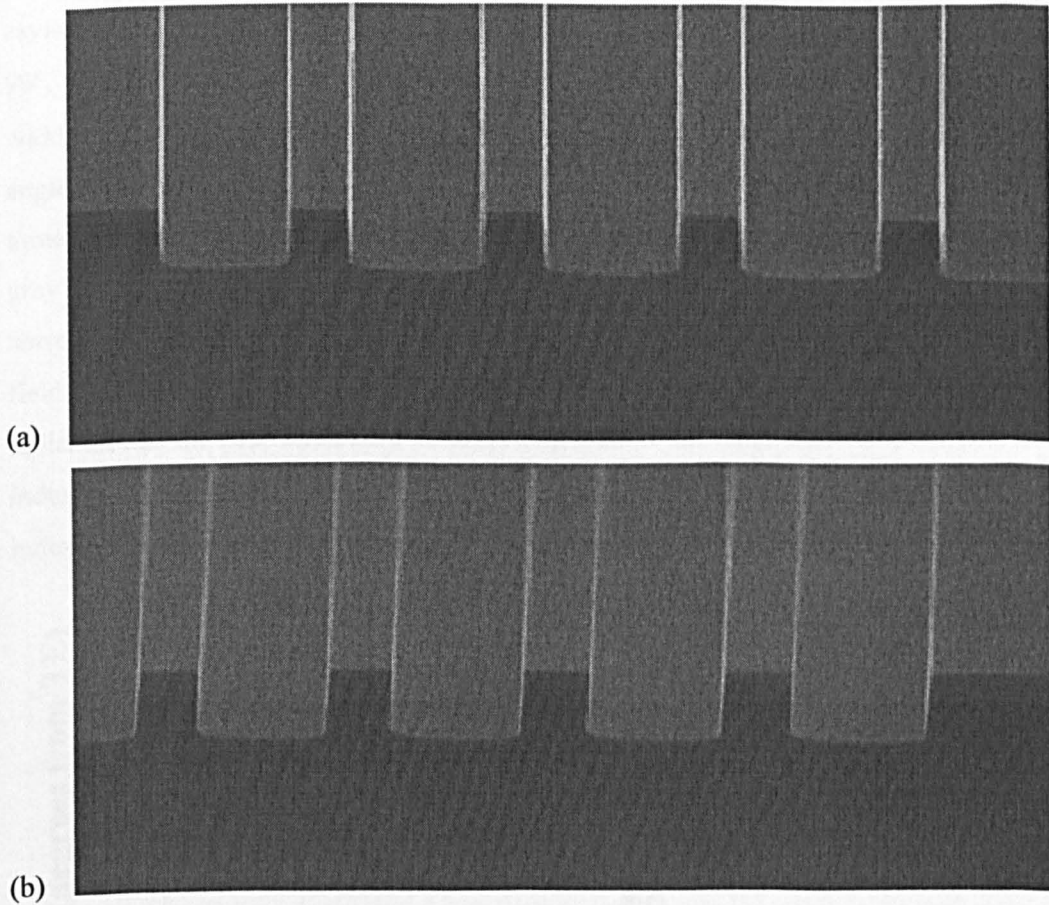


Fig. 4.5: Scanning electron micrographs of the cleaved end facets of waveguides nominally  $4\text{ }\mu\text{m}$  wide. (a) Symmetric cross section, (b) asymmetric cross section.

### 4.3 Experimental results and comparisons

The optical losses of the TE and TM modes were calculated from measurements for the symmetric waveguide set, and were found to be identical within the experimental uncertainty for guide widths of  $2.4\text{ }\mu\text{m}$  and greater. Polarisation measurements were limited to waveguides meeting this condition, as the elliptical polarisation analysis does not take account of differential loss. The loss measurements are presented and discussed in chapter six. The mode angle measurements are plotted in Fig. 4.6. The vertical scale shows the modulus of the angle in degrees from horizontal, the two angles always being separated by  $90^\circ$ . The waveguide widths were measured from scanning electron micrographs to an accuracy of  $0.1\text{ }\mu\text{m}$  between points halfway up the side walls.

The results demonstrate the main aspects of the theory. The modes in the waveguides with symmetric cross section are close to TE and TM for all guide widths, with a sudden switch at a guide width of  $\sim 3.63\text{ }\mu\text{m}$ , the phase-matching width. The narrow range of widths over which the transition occurs verifies that the waveguides are nearly symmetrical. The

asymmetric waveguide results indicate orthogonal modes rotating together through nearly 90°. The switching of dominant field components occurs gradually over a range of guide widths, and the mode angles pass through  $\pm 45^\circ$  at  $W_{PM}$ . The measured orientation of the mode angles with respect to the side-wall slant direction is shown schematically in Fig. 4.7, for three different waveguide widths where the central guide has the phase-matching width. The grey arrow represents the mode with the smaller effective index, which is quasi-TE in the narrowest guide and quasi-TM in the widest guide. Inspection of the directions of the electric field vectors of the modes with respect to the waveguide boundaries at phase-matching indicates that the nett ratio of the normal component to the tangential component of the lower-index mode is larger than that of the orthogonal mode. This fact provides the origin of the index difference at phase-matching.

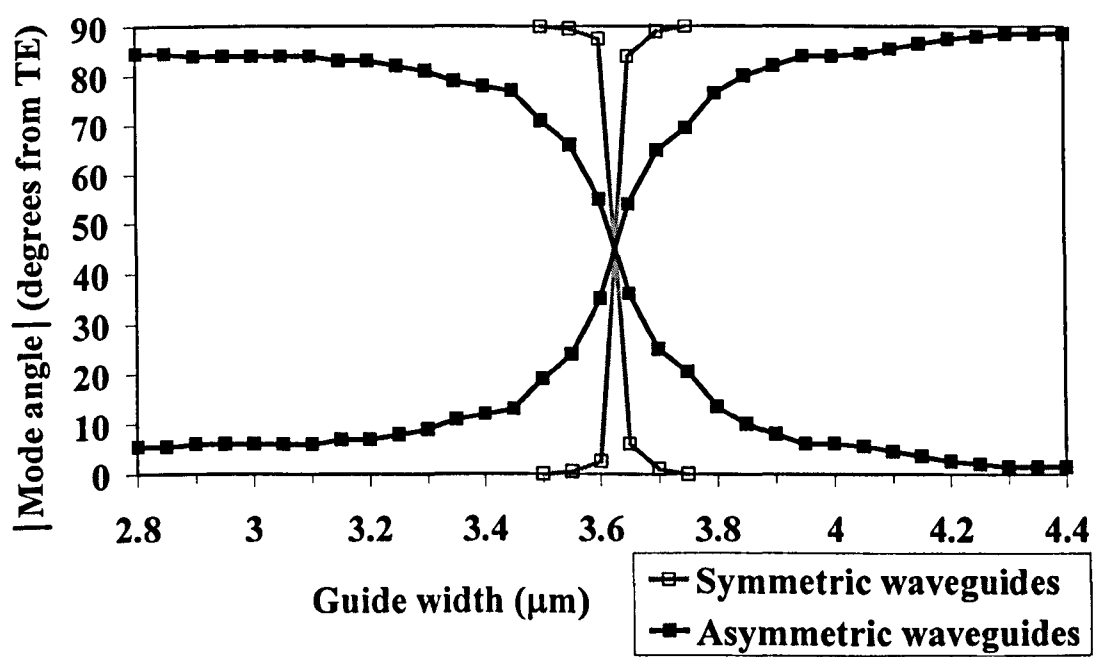


Fig. 4.6: Measured mode angles versus waveguide width. The modulus of the mode angle is plotted in degrees from horizontal; one mode angle is positive and the other negative, so that the two angles are always separated by 90°.

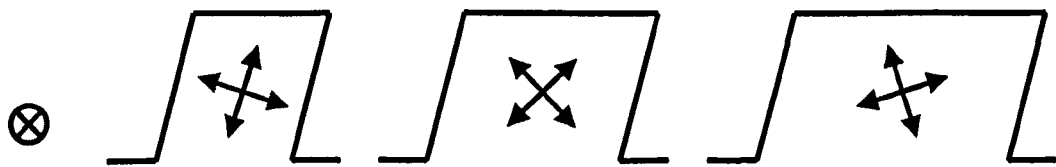


Fig. 4.7: Schematic diagram of asymmetric waveguide cross sections showing the measured orientation of the mode angles with respect to the side-wall slant direction. The guide width increases from left to right, with the central guide having the phase-matching width. The grey arrow represents the mode with the smaller effective index, which is quasi-TE in the narrowest guide and quasi-TM in the widest guide.

The modulus of the measured index difference is plotted against guide width in Fig. 4.8. The symmetric guide plot confirms the phase-matching guide width, where the index difference approaches close to zero. The asymmetric guide data show clearly that the index difference does not go through zero. The minimum occurs at  $W_{PM}$ . The two sets of data have similar values for guide widths for which the modes are not strongly hybrid.

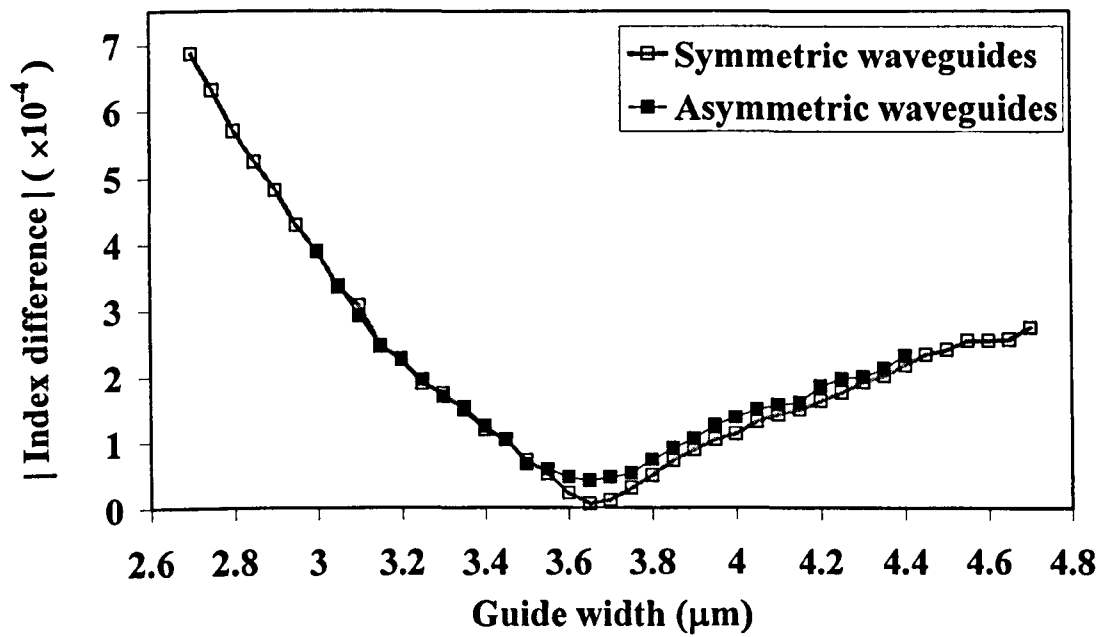


Fig. 4.8: Modulus of effective index difference versus waveguide width.

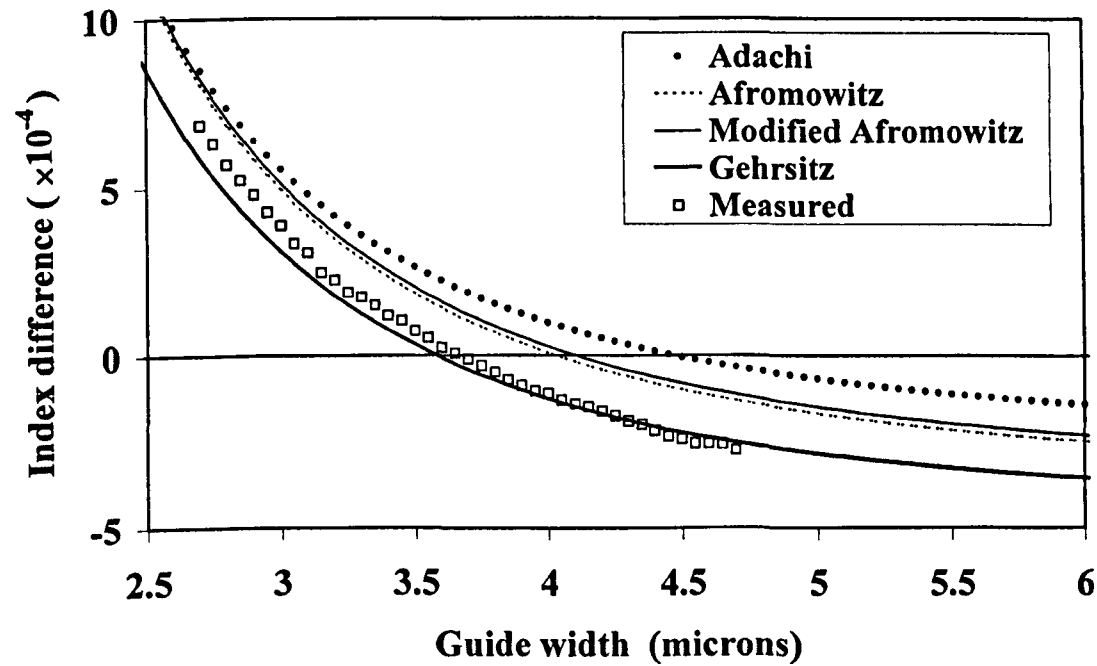


Fig. 4.9: Effective index method simulations of index difference versus waveguide width for symmetric waveguides. Comparison of results for several sets of published index data, and measured values.



Effective index method simulations of index difference versus waveguide width for symmetric waveguides are shown in Fig. 4.9. Results obtained using four sets of published GaAs/AlGaAs refractive index data for the P0 wafer specification are compared with the measured values. The results obtained using the Afromowitz index data, with or without the minor modification, are almost identical to the FMM method results obtained using the same data as presented in Fig. 4.1, with phase matching predicted at a guide width close to 4.1  $\mu\text{m}$ . The prediction of 3.55  $\mu\text{m}$  obtained using the Gehrsitz data is closest to the measured value of 3.63  $\mu\text{m}$ , while the Adachi data appears to be the least accurate, returning a value of 4.45  $\mu\text{m}$ . The sensitivity of the value of  $W_{PM}$  to the index contrast is revealed by the wide range of predicted values. This is despite the fact that verification of all of these sets of index data has been reported for the design of waveguides in respect of the parameters of fundamental mode propagation and higher order mode leakage (Gehrsitz in [131], Afromowitz in [107] and Adachi in [132]). The best match to the experimental data is provided by the Gehrsitz model, which is the most recently published of these empirical formulations and should therefore be the most thoroughly informed.

Other potential causes for the discrepancy between measured values and given predictions are considered as follows. The guide widths were measured to 0.1  $\mu\text{m}$  accuracy, while the SIMS characterisation of wafer layer thicknesses and Al fractions confirmed only insignificant deviations from the specification. Some material birefringence is expected in the AlGaAs layers, resulting from compressive strain due to the small difference in lattice constant [103] between these layers and that of the GaAs substrate [134]-[135], [105]. The influence of this birefringence is expected to be small as most of the optical field propagates in unstrained GaAs. The near-identical data obtained for the effective index and FMM methods indicates that they are equally suitable for the purpose of modelling waveguide birefringence. The sensitivity of the phase-matching width to the epitaxy design is investigated experimentally in chapter six. Further effective index method simulations showed that  $W_{PM}$  is not sensitive to wavelength, having a variation of  $-0.08 \mu\text{m}$  per 100 nm around the design wavelength of 1550 nm.

The measurements of mode angle and index difference enabled the calculation of expected polarisation extinction for any propagation length from elliptical analysis. These indirect measurements are compared with direct measurements and coupled-mode theory predictions for asymmetric guides with lengths of 5, 10, 15, and 20 mm in Figs. 4.10a to 4.10d respectively. The direct and indirect measured data are plotted against guide width, which appears on the upper horizontal axis. Values of the propagation constant difference  $\Delta\beta$  measured on symmetric waveguides with the corresponding width are given on the lower horizontal axis. The modes of these symmetric waveguides provide a close approximation to

the purely TE and TM case required by coupled-mode theory. The values of  $\Delta\beta$  can be determined from Fig. 4.8 using equation (2.5.3). The coupled-mode theory predictions were calculated using a value of  $93 \text{ m}^{-1}$  for the coupling constant  $\kappa$ , which was obtained from the coupling length expected from the extinction values measured at the phase-matching width.

There is a clear agreement between the experimental and theoretical data. The progress of the polarisation conversion at the guide width of phase matching may be tracked through the plots, increasing with length to a maximum at  $z = 15 \text{ mm}$  where 97% of the power has coupled from TE to TM. With  $\kappa = 93 \text{ m}^{-1}$ , complete coupling is expected at  $z = 17 \text{ mm}$ . Beyond this length the light begins to couple back again. For  $\Delta\beta \neq 0$ , complete coupling does not occur, but the coupling length becomes shorter as the index difference increases. In the resulting curve, each subsequent lobe away from the central lobe corresponds to light that has coupled to a maximum and back again one additional time. These smaller peaks can be seen in the experimental data, especially at the shorter lengths.

The longer lengths of 25 mm and 30 mm were measured, but the plots are not included here because they are less clear due to undersampling of the closely spaced peaks, particularly for narrower guide widths where the  $0.05 \text{ }\mu\text{m}$  interval corresponds to a larger change in  $\Delta\beta$ . Conversely, the form of the data remains clear at narrow widths for the 5 mm long guides, enabling the directly measured data to be displayed for an extended guide width range.

The coupling mechanism in the symmetric guides was very weak. A direct measurement of polarisation conversion was performed on a 30 mm length and the extinction was found to be greater than 20 dB for all widths, indicating negligible conversion. Elliptical analysis predicts this result. The FMM method simulations show that a slant angle of  $4.8^\circ$  is required to produce a coupling constant of  $93 \text{ m}^{-1}$  and a coupling length of 17 mm. This gives very good agreement with the experimental data.

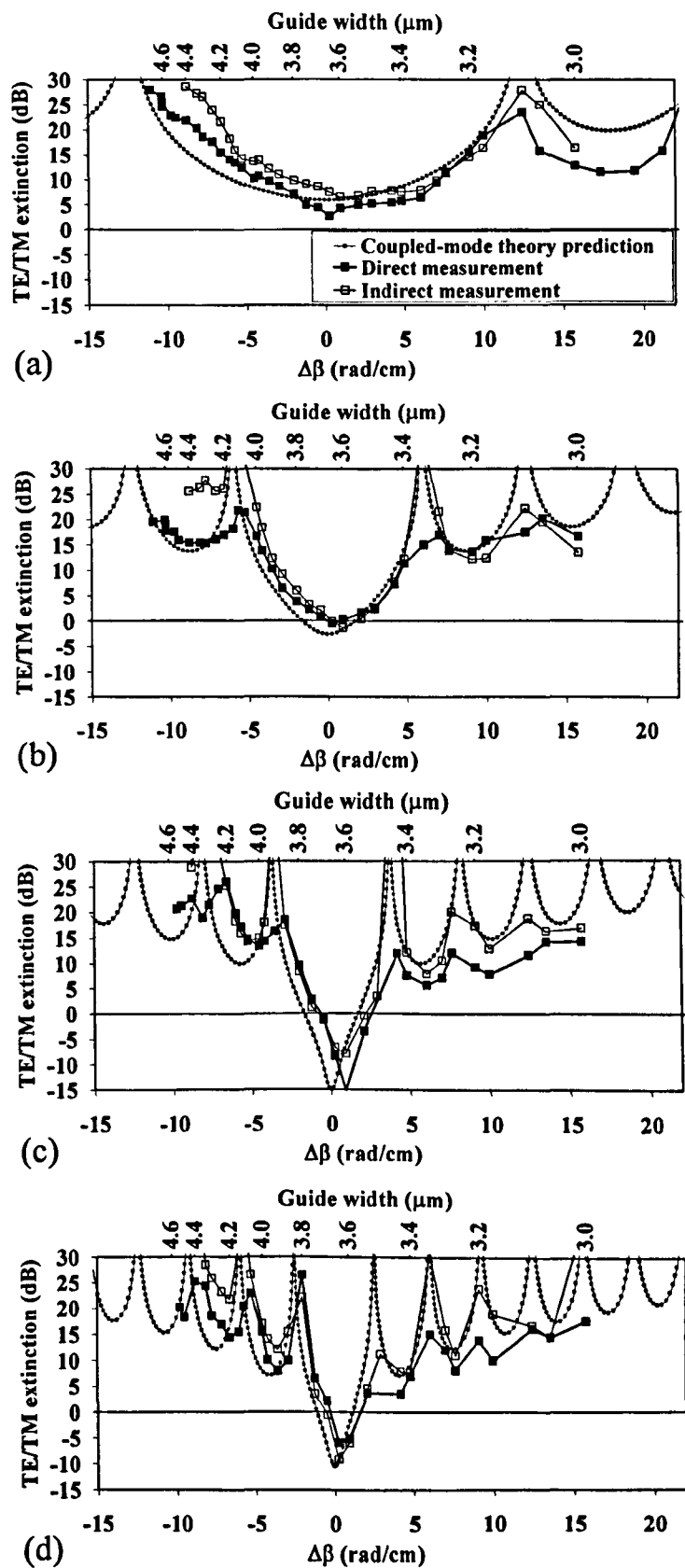


Fig. 4.10: Polarisation extinction versus propagation constant difference  $\Delta\beta$ . Comparison of coupled-mode theory prediction with direct measurement and indirect measurement obtained from elliptical polarisation analysis. Guide lengths (a) 5 mm, (b) 10 mm, (c) 15 mm, (d) 20 mm.

## 4.4 Conclusions

The sensitivity of polarisation behaviour to process-dependent asymmetry caused by non-vertical etching in high-index-contrast passive waveguides has been investigated experimentally. Strong polarisation conversion was observed at a critical guide width corresponding to the closest approach of the effective indices of the polarised modes. Results indicate that light propagating in a waveguide with a parallel side-wall slant angle of  $5^\circ$  and a critical width of  $3.63\ \mu\text{m}$  will undergo complete polarisation conversion from TE to TM in a length of 17 mm. The polarisation angles of the fundamental waveguide modes were measured, and a novel technique was employed to measure the index difference between these modes. The two cases of waveguides with and without cross-sectional symmetry were compared. An elliptical polarisation analysis was carried out using these results, for a range of guide widths.

The results have been described in terms of coupled-mode theory, using a value of the coupling constant that was determined experimentally. The validity of the coupled-mode description has been confirmed. In particular, the results demonstrate that if the index relationship for purely TE and TM modes is known accurately for a given epitaxy design, then the coupling constant can be calculated from measurements of the behaviour of one waveguide width; hence the behaviour of a waveguide with any width can be predicted.

Waveguide mode characteristics predicted by vector finite element method and film mode matching method simulations have been demonstrated experimentally. It has been shown that the polarisation mode angles rotate through  $90^\circ$  as the guide width passes through the critical width, rather than remaining as TE and TM modes. The results also confirm that while the modes in symmetric guides become degenerate at a critical width, the modes in an asymmetric guide do not become degenerate for any width. Quantitative agreement has been established between FMM method simulations and experimental observation of polarisation coupling strength. It is concluded that a discrepancy between predicted and measured phase-matching guide width is attributable to inaccurate refractive index data. The sensitivity of the phase-matching width to the index contrast has been shown, and the uncertainty in predictions of its value due to disagreements in published refractive index data has been demonstrated using effective index method simulations.

The results presented in this chapter highlight important issues for both the waveguide designer and the process engineer engaged in the realisation of high-index-contrast waveguide devices. The need to predict and avoid the critical guide width is emphasised, while the impact of process-dependent asymmetry in the waveguide cross section is shown. The experimental examples given provide quantitative benchmarks.

## Chapter 5: Polarisation Conversion in Electrooptic Waveguides

This chapter describes and demonstrates how unintended polarisation conversion can occur in GaAs waveguides in the presence of applied electric fields. An experimental investigation of the influence of the electrooptic effect is presented, and the results are described in terms of the coupled-mode theory.

### 5.1 Electrooptic polarisation conversion theory

Electrooptic waveguides in GaAs are commonly used as phase modulators, often as part of a Mach-Zehnder interferometer modulator. The scope of this chapter is limited to phase modulators in which the intended electrooptic modulation is produced by a field applied in the structure whose net direction is vertical. A cross section of such a waveguide is shown schematically in Fig. 5.1 with emphasis on the electrical aspects of the device, including the distribution of the applied electric field. The linear electrooptic effect in GaAs is described in section 2.6. The behaviour described in chapter four is modified in two ways by the electrooptic effect which may be presented in terms of the coupled-mode theory. Firstly, correct operation of the phase modulator results in an alteration of the TE-TM phase relationship; secondly, a small misalignment of the electrode with respect to the waveguide may introduce a horizontal applied field component which presents an additional coupling mechanism. These two effects are discussed in more detail below.

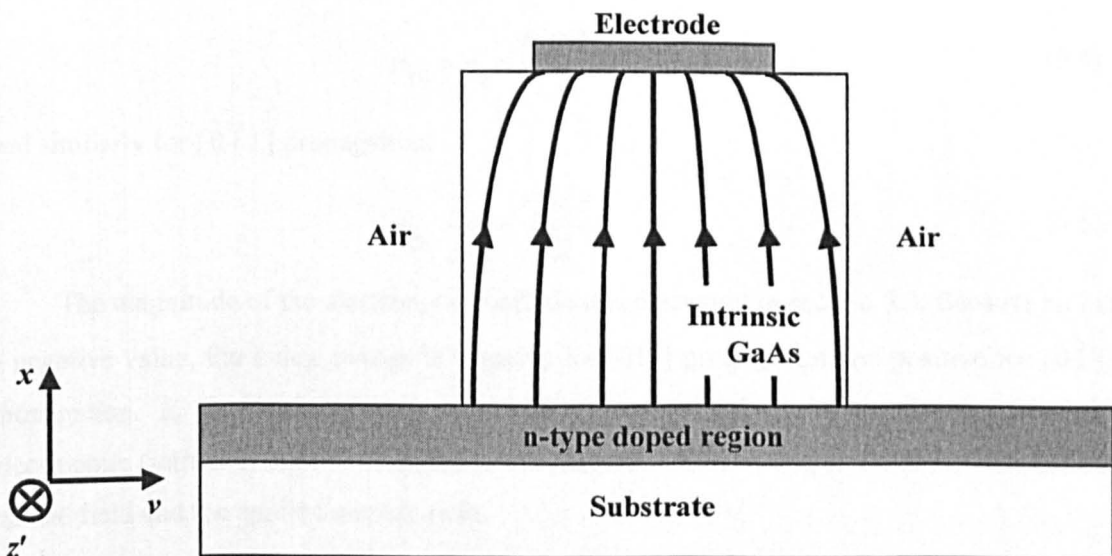


Fig. 5.1: Schematic of an electrooptic waveguide cross section showing the applied electric field.

### 5.1.1 Electrooptic index matching

It was shown in section 2.6 that for epitaxy on the (100) surface an electric field applied in the vertical direction will alter the propagation constant of TE polarised light by the linear electrooptic effect, with a magnitude and sign that are dependent on the propagation direction. The propagation constant of TM polarised light is not altered by the linear electrooptic effect. It is therefore apparent that the TE-TM index relationship is changed by the application of an electric field. The two cases of propagation along the [011] and the  $[0\bar{1}1]$  directions are considered, as they provide the largest magnitude of TE index change, with opposite sign.

The magnitude of the TE index change may be obtained from the index ellipsoid. Recalling equation (2.6.7) and setting  $E_v$  to zero gives the section through the index ellipsoid for [011] propagation with only vertical applied fields:

$$\frac{x^2}{n_0^2} + \frac{v^2}{n_0^2} - r_{41} v^2 E_x = 1 \quad (5.1)$$

This ellipse equation may be reduced to its simplest form, generalised in equation (2.6.5), by introducing the TE effective index  $n_{TE}$ , requiring:

$$\frac{1}{n_{TE}^2} = \frac{1}{n_0^2} - r_{41} E_x \quad (5.2)$$

Small index differences may be approximated by the relation:

$$n_{TE} - n_0 \approx -\frac{n_0^3}{2} \left( \frac{1}{n_{TE}^2} - \frac{1}{n_0^2} \right) \quad (5.3)$$

which is obtained from the differential relation  $dn = -(n^3/2)d(n^{-2})$ . Substitution in (5.2) yields for [011] propagation:

$$n_{TE} = n_0 + \frac{r_{41} n_0^3 E_x}{2} \quad (5.4)$$

and similarly for  $[0\bar{1}1]$  propagation:

$$n_{TE} = n_0 - \frac{r_{41} n_0^3 E_x}{2} \quad (5.5)$$

The magnitude of the electrooptic coefficient is discussed in section 5.3. Because  $r_{41}$  has a negative value, the index change is negative for [011] propagation and positive for  $[0\bar{1}1]$  propagation.  $E_x$  is given by  $V/d_x$ , where the parameter  $d_x$  expresses the depth of the electrooptic (intrinsic) region, modified to take account of an incomplete overlap between the optical field and the applied electric field.

### 5.1.2 Electrooptic coupling mechanism

The description of the electrooptic effect in GaAs given in section 2.6 shows that an applied electric field component  $E_v$  which is directed horizontally across the waveguide induces birefringence with principal axes inclined at  $\pm 45^\circ$  from the horizontal plane. In this circumstance, the mode polarisation angles will also be inclined, at an angle which is influenced by the horizontal field component, the index relationship for the modes of the passive guide, and any vertical applied field. Polarisation coupling from TE to TM can then occur, in a manner which is also influenced by those factors. An unintended horizontal applied field component can result from an offset of the electrode with respect to the waveguide, resulting from alignment tolerances in the UV photolithographic process. This situation is depicted schematically in Fig. 5.2, which shows that the fringing electric field is asymmetric in the intrinsic region of the waveguide. This is in contrast with the symmetry shown in Fig. 5.1 for the accurately aligned electrode, resulting in no nett horizontal field.

Rigorous modelling of polarisation conversion occurring due to this effect would require sophisticated numerical techniques such as VFEM, including simulations of the applied field distribution and its overlap with the optical field. Such simulations are not attempted in this work. A simpler description is again provided by the coupled-mode theory, with the benefits described in chapter four. The horizontal field component provides a coupling mechanism, and the index relationship identified in chapter four is influenced by the vertical applied field component. The coupling constant will be obtained as a function of electrode offset from measurements, providing an experimental benchmark.

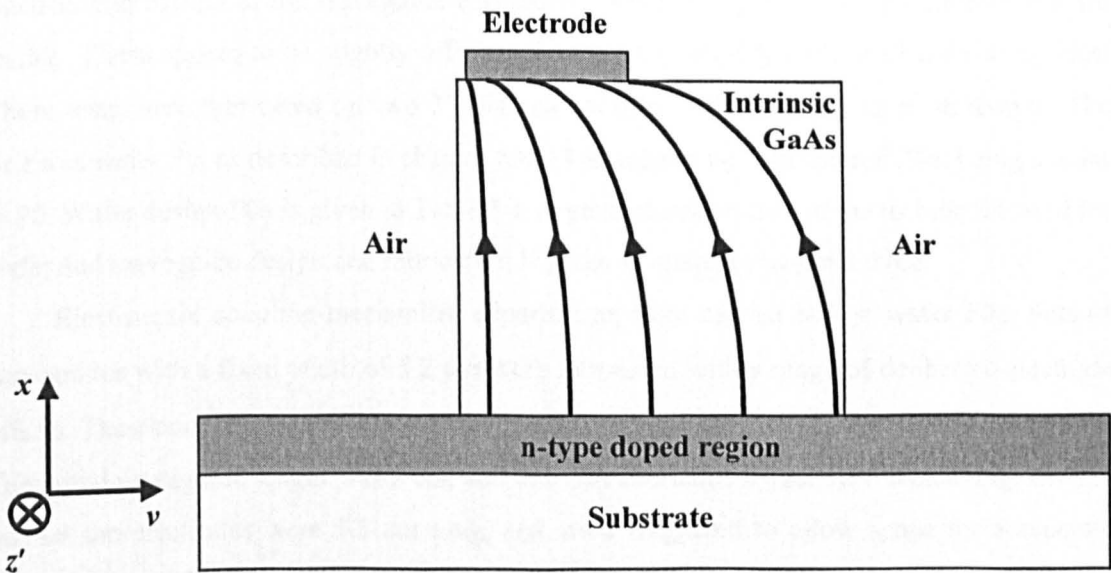


Fig. 5.2: Schematic diagram of an electrooptic waveguide cross section featuring the electric field resulting from an offset electrode.

## 5.2 Experiments

### 5.2.1 Experimental device design and fabrication

Electrooptic waveguide tests were designed to investigate electrooptic index matching and the electrooptic coupling mechanism. For electrooptic index matching experiments, sets of straight electrooptic waveguides were defined, with widths of  $3.0\text{ }\mu\text{m}$  to  $7.0\text{ }\mu\text{m}$  in  $0.5\text{ }\mu\text{m}$  intervals, and with lengths of up to 3 cm. On each waveguide the electrode was  $2\text{ }\mu\text{m}$  narrower than the waveguide. A section of this waveguide set is shown in the scanning electron micrograph in Fig. 5.3. To the left is a bond pad measuring  $100\text{ }\mu\text{m}$  by  $120\text{ }\mu\text{m}$ , to facilitate temporary electrical connections to be made using probes. This single bond pad was connected to all of the test waveguides to save space. Electrical connection to the n-type doped region was made using a free-standing ground pad positioned nearby on the chip, consisting of gold deposited on the top surface of the wafer surrounded by etched regions. The circuit formed by the top contacts and ground pad therefore contained a pair of back-to-back Schottky barrier diodes, in which the top contact was reverse biased and the ground pad was forward biased. This ensured that the n-type material was grounded and the signal voltage was dropped across the electrooptic region. It was found that typically around 1 V was required to deplete free carriers from the intrinsic (minimised n-type) region.

To ensure the presence of a coupling mechanism, the guides were fabricated with a small parallel side-wall slant as described in chapter four. This is apparent in the scanning electron micrograph of the waveguide end facets shown in Fig. 5.4. The gold electrodes are visible. These appear to be slightly offset with respect to the top surface of the waveguides. These tests were fabricated on two 3" diameter wafers with different layer structures. The first was wafer P0, as described in chapter four. The second was designated P0a, being similar to P0. Wafer design P0a is given in Table 3-I. A general description of the techniques used for wafer and waveguide design and fabrication is given in chapters two and three.

Electrooptic coupling mechanism experiments were carried out on wafer P0a. Sets of waveguides with a fixed width of  $5.2\text{ }\mu\text{m}$  were fabricated with a range of deliberate electrode offsets. The electrodes were  $1\text{ }\mu\text{m}$  wide and were offset by  $-2\text{ }\mu\text{m}$  to  $2\text{ }\mu\text{m}$  in steps of  $0.5\text{ }\mu\text{m}$ . The initial waveguide length was 2 cm, and this was shortened by sequential cleaving. On this test set the electrodes were 1.5 cm long, and were staggered to allow space for a separate bond pad for each to one side of the waveguide set. Identical sets of both tests were fabricated for propagation along both the  $[011]$  and  $[0\bar{1}1]$  directions to ensure that both positive and negative electrooptic index changes were available.



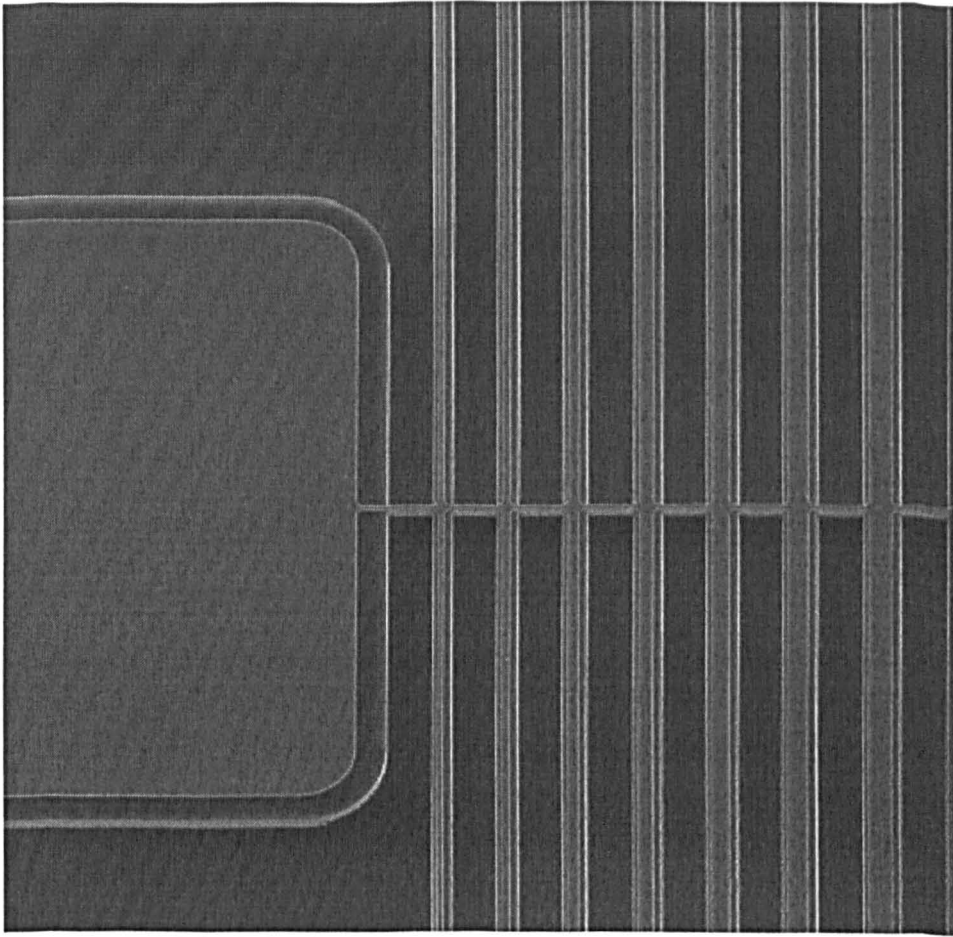


Fig. 5.3: Scanning electron micrograph of electrooptic waveguides of various widths, showing a bond pad on the left, and a 1  $\mu\text{m}$ -wide track connecting to all of the waveguide electrodes.

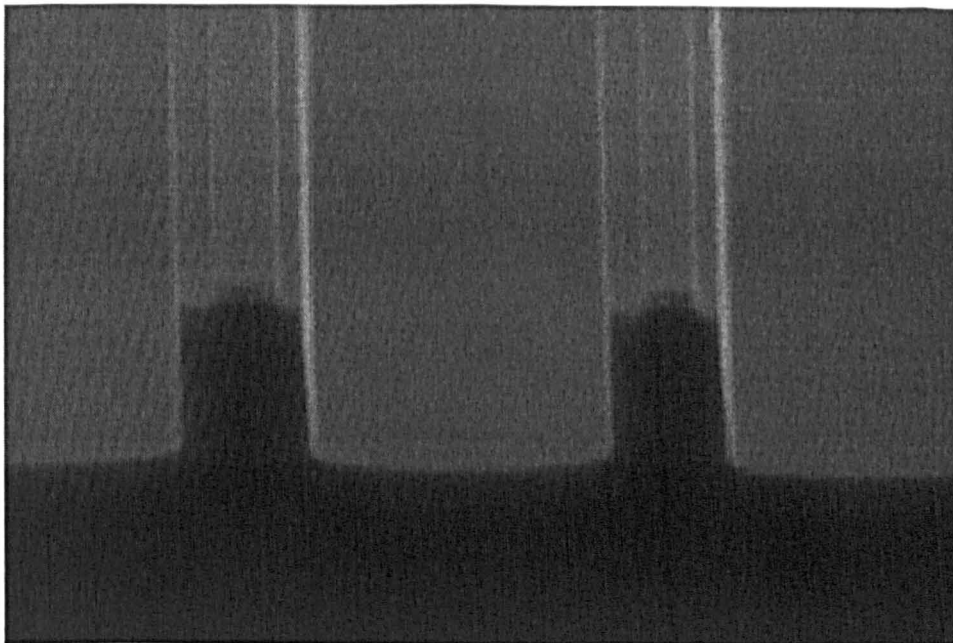


Fig. 5.4: Scanning electron micrograph of the end facets of electrooptic guides, wafer P0.

### 5.2.2 Experimental methods

The experimental methods used are described in chapter three. For the electrooptic measurements described in this chapter, a linear ramp voltage was applied to the device under test in the form of a sawtooth signal at low frequency. A TE input polarisation was used throughout, and the output polarisation state was analysed using a second polariser. The transmitted signal and the voltage across the device were observed using an oscilloscope. The voltage required to obtain phase matching was measured as a function of waveguide width. This was indicated by the presence of a conversion peak. An example of this measurement is shown in Fig. 5.5. The curves have a characteristic shape that matches the form of the coupled-mode theory prediction of mode coupling versus phase mismatch shown in Fig. 2.6, as presented in chapter two. In cases of very strong coupling, indicated by multiple peaks, the waveguides were cleaved to a shorter length to enable identification of the correct voltage.

The offset electrode waveguide set was used to measure coupling constant as a function of electrode offset. Measurements of the progress of the polarisation conversion along the length of the waveguides were enabled by sequential cleaving. In order to obtain a value for the coupling constant for each electrode offset, the data for each guide were compared with a theoretical plot provided by the coupled-mode theory. An estimate of the best fit to the coupling length enabled a value for the coupling constant to be determined.

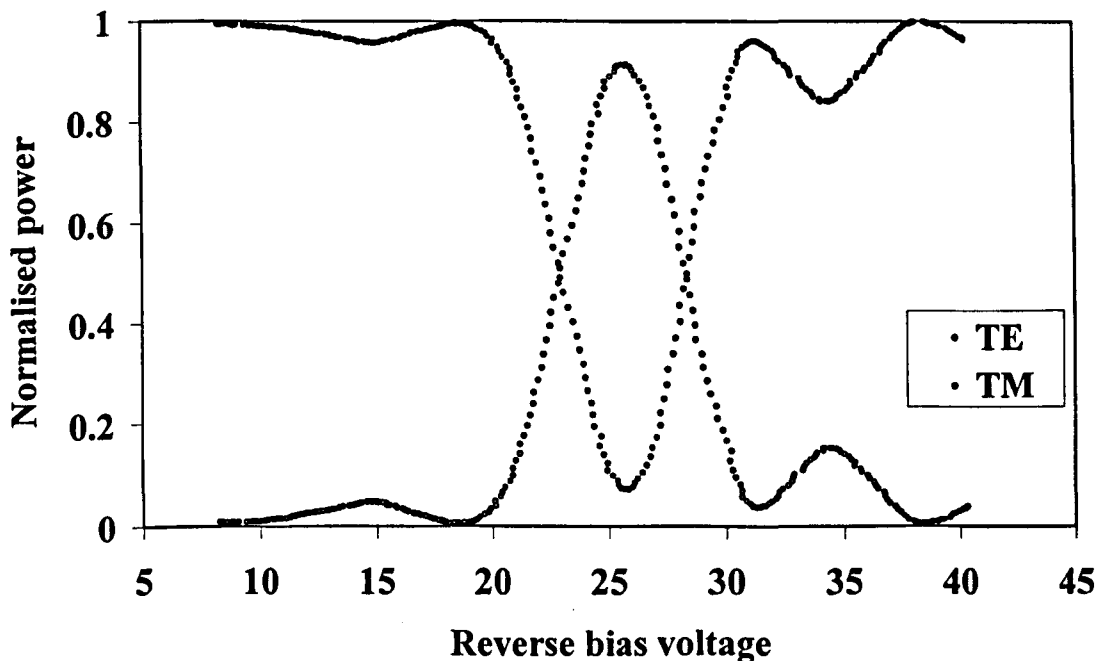


Fig. 5.5: An example of a measurement of phase-matching voltage and polarisation coupling. TE and TM components of normalised optical power versus reverse bias voltage for an electrooptic waveguide with an offset electrode. 91% power coupling from the TE input state to TM is indicated at the phase-matching voltage of 25.9 V, occurring in a length of 1 cm.

### 5.2.3 Quantification of the linear electrooptic effect

In order to predict the influence of the linear electrooptic effect on polarisation behaviour, it is necessary to quantify accurately its strength. The refractive index of the TE mode with a vertical applied field is given by:

$$n = n_0 \pm \frac{n_0^3 r_{41} V_x}{2d_x} \quad (5.6)$$

where  $d_x$  is an equivalent length taking account of the electrooptic depth, modified by the imperfect overlap of the optical and electric fields. The accuracy of the effective index  $n_0$  is critical in equation (5.6) because it is raised to the third power. The uncertainty in published refractive index data was highlighted in chapter four. The exact value of the electrooptic coefficient  $r_{41}$  is also uncertain, as a range of values has been published [136]-[138], [139]-[143], [148]. These studies are reviewed in references [144] and [106], which favour the value  $-1.36 \times 10^{-12} \text{ m}^{-1}\text{V}$  at a wavelength of  $1.5 \text{ }\mu\text{m}$ . Specifically, this is the “unclamped” or constant-stress value of  $r_{41}$ , which applies for voltage signal frequencies well below the acoustic resonances of the sample and is therefore relevant to the experiments presented in this work. The magnitude of the “clamped” or constant-strain value of the electrooptic coefficient is around 12% larger. Additional uncertainty in the strength of the linear electrooptic effect arises from the electrooptic coefficient of AlGaAs, which has not been studied extensively, but is expected to be slightly weaker than that of GaAs [23], [145]. Furthermore, small contributions to refractive index changes from various other electrooptic effects may occur [143], [146], [148].

It is therefore desirable to obtain a specific independent measurement of the index change resulting from an applied voltage in waveguides for the wafer design under consideration, including the influence of  $r_{41}$ ,  $d_x$  and  $n_0$ . This may be expressed by a specific electrooptic parameter  $R_{41}^{\text{P0}}$ , which is defined in equation (5.8). Its value was obtained from measurements on Mach-Zehnder interferometer intensity modulators fabricated on wafer P0. The on-off switching voltage  $V_\pi$  is given by:

$$V_\pi = \frac{d_x}{n_0^3 r_{41}} \frac{\lambda_0}{L} \quad (5.7)$$

$V_\pi$  was measured for several devices, at low voltage to prevent a significant contribution to the phase shift by the quadratic electrooptic effect. The mean value of  $V_\pi$  returned a value for the specific electrooptic parameter:

$$R_{41}^{\text{P0}} = \frac{n_0^3 r_{41}}{d_x} = -1.4 \times 10^{-5} \text{ V}^{-1} \quad (5.8)$$

## 5.3 Experimental results and comparisons

### 5.3.1 Phase-matching voltage versus width results

Fig. 5.6 shows the measured values of the phase-matching voltage,  $V_{PM}$ , versus guide width for wafer P0. These are compared with predicted values of  $V_{PM}$ , calculated from equation 5.6 using the measurements of the index difference in symmetric guides obtained in chapter four, and the measured value of the specific electrooptic parameter. A good agreement is shown. The curve for  $[011]$  propagation shows that the magnitude of the negative TE index change required to match the TE and TM indices becomes smaller with guide width, reducing to zero at  $W_{PM}$ . For guide widths narrower than this the electrooptic effect pulls the indices apart and phase matching is not observed. For  $[0\bar{1}1]$  propagation the positive TE index change causes phase matching only in guides narrower than  $W_{PM}$ . The guide width at which  $V_{PM}$  goes to zero provides a good match with the value of  $W_{PM}$  obtained from passive guide measurements, i.e.  $\sim 3.63 \mu\text{m}$ .

The reciprocal calculation of index difference from the measurements of  $V_{PM}$  is plotted in Fig. 5.7, alongside the measured index difference values which are recalled from chapter four. Fig. 5.7 demonstrates that the  $V_{PM}$  data form a continuous curve, which would be apparent in Fig. 5.6 if the  $[0\bar{1}1]$  data were reflected about the horizontal axis.

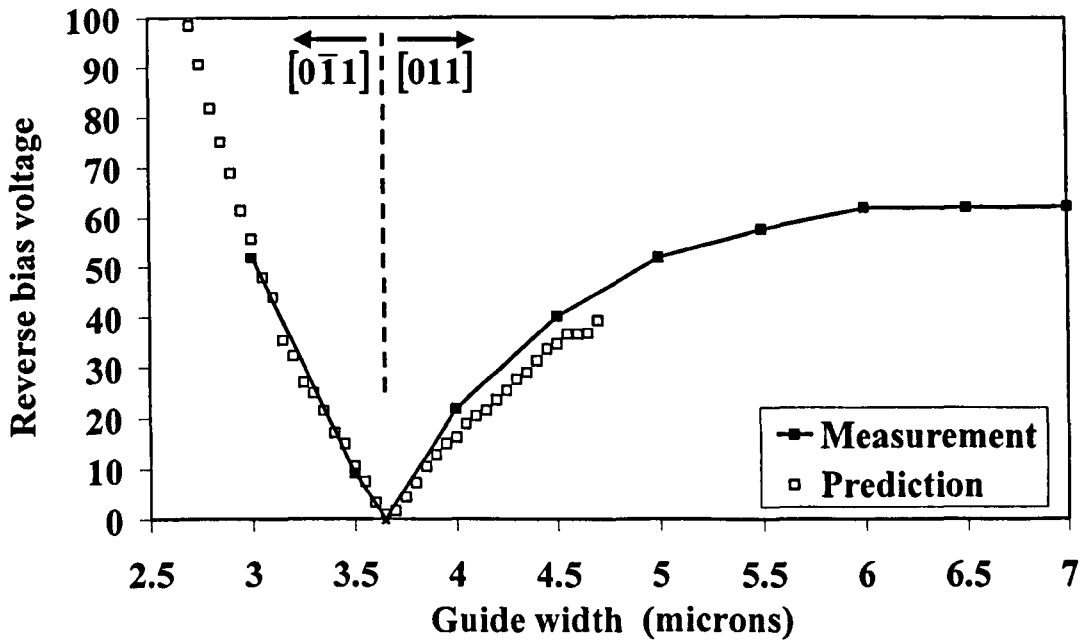


Fig. 5.6: Measured and predicted values of the phase-matching voltage versus guide width for wafer P0. The propagation directions are indicated. The predicted values were calculated from measurements of index difference and the specific electrooptic parameter.

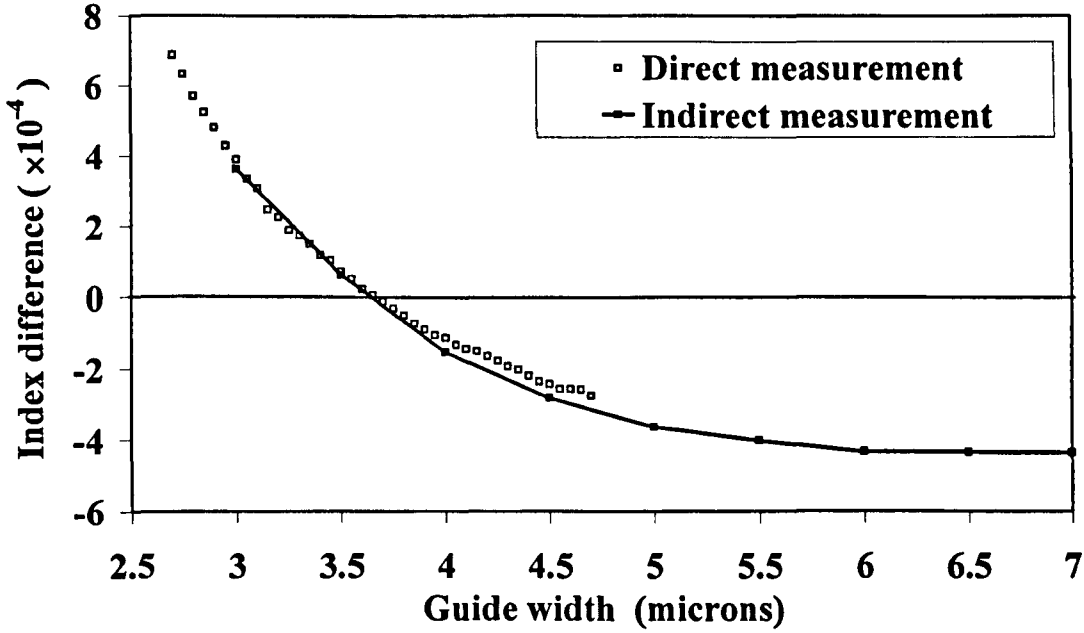


Fig. 5.7: Index difference values for wafer P0, versus guide width. Indirect measurements obtained by calculation from measured values of  $V_{PM}$  and the specific electrooptic parameter. Comparison with direct measurements as presented in chapter four.

The results show that phase-matched polarisation conversion can occur for any guide width in the useful range, nominally 3-5  $\mu\text{m}$ , with an applied voltage smaller than the expected reverse bias breakdown voltage. Using the information presented in Fig. 5.6, phase-matched conversion can be prevented on wafer P0 by selecting appropriate combinations of guide width and propagation direction. However, there would still be a likelihood of significant non-phase-matched conversion occurring in the presence of a coupling mechanism, while the restricted range of guide widths available would cause inconvenience for the device designer. It is concluded that wafer design P0 is generally susceptible to polarisation conversion.

Fig. 5.8 shows the measured values of  $V_{PM}$  versus guide width for wafer P0a. The behaviour is similar to that of wafer P0, but with  $W_{PM}$  shifted to 3.9  $\mu\text{m}$ . Also, the values of  $V_{PM}$  for wider guides are smaller than the equivalents for wafer P0, indicating a smaller index difference. This fact makes wafer P0a more suitable for further investigations of electrooptic polarisation conversion in the following sections of this thesis.

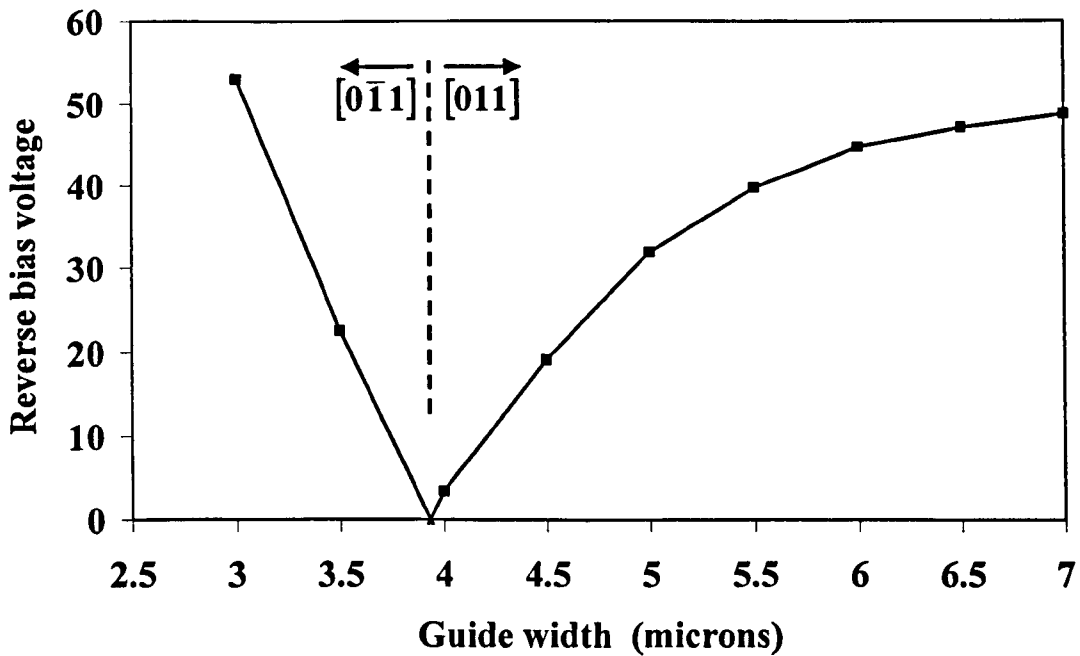


Fig. 5.8: Measured and values of the phase-matching voltage versus guide width for wafer P0a. The propagation directions are indicated.

### 5.3.2 Offset electrode results

The results for offset electrode tests on wafer P0a are shown in Fig 5.9. The TE and TM output power components were measured with the phase-matching voltage applied, which was typically 35 V. Normalised power components with TE and TM polarisations are plotted versus electrooptic length for nine waveguides having electrode offsets of  $-2\text{ }\mu\text{m}$  to  $+2\text{ }\mu\text{m}$  in  $0.5\text{ }\mu\text{m}$  intervals respectively. Each waveguide in the test set contained a different length of passive waveguide. The effect of the passive section on the polarisation extinction can be ignored because the waveguide width of  $5.2\text{ }\mu\text{m}$  is well away from the phase-matching guide width for this wafer, as shown previously in Fig. 5.8. It was also clear during the experiments that the polarisation conversion at zero bias was negligible in the context of this experiment. The chip was successively cleaved to shorter lengths, the interval being 1.6 mm.

The nine plots show the polarisation conversion proceeding with approximately the expected sinusoidal form. A raised cosine curve providing an estimate of the best fit is included on each, to provide a value for the coupling length. As expected, the coupling length is shorter for greater electrode offsets, corresponding to a stronger coupling mechanism provided by a greater horizontal electric field component. The coupling length estimates were used to calculate a value for the coupling constant  $\kappa$  for each waveguide. A plot of coupling length versus electrode offset is shown in Fig. 5.10, with the corresponding coupling constant indicated on the second vertical axis. The results show that the coupling constant increases

rapidly with electrode offset. With 0.5  $\mu\text{m}$  offset, the coupling length is less than 20 mm, with  $\kappa$  approaching  $100\text{ m}^{-1}$ , which is comparable with the value obtained from a parallel side-wall slant of  $5^\circ$  in passive waveguides on wafer P0. For the largest offset of 2  $\mu\text{m}$ , the coupling length is 10 mm, corresponding to a coupling constant of  $174\text{ m}^{-1}$ .

A deviation of the measured polarisation conversion values from the expected theoretical raised cosine form is noticable in Fig. 5.9. A likely reason for this is a small angular misalignment of the metal with respect to the waveguide. For the positive electrode offset values of 2.0, 1.5 and 1.0  $\mu\text{m}$ , the rate of conversion becomes progressively slower relative to the raised cosine with length, suggesting a larger electrode offset at the electrical connection end (opposite to the end that was sequentially cleaved), diminishing along the length due to angular misalignment. The trend is most noticeable for the largest electrode offset. This may be due to an increase in phase-matching voltage, and consequently in coupling strength, caused by the increased guide width due to metal masking. Because the metal deposition is the first processing step, any misalignment of the electrode beyond the intended waveguide edge would increase the guide width, which would raise the phase-matching voltage and also enhance the coupling constant because all measurements were made at the phase-matching voltage. Any angular misalignment would cause a variation of the guide width along the length, and consequently a variation of the phase-matching voltage and of the coupling strength. The variation in phase-matching voltage would in turn cause a further deviation from the expected raised cosine form by smearing the phase-matched peak with respect to voltage along the length. The phase-matching voltage was indeed found to be several volts larger for the 2.0  $\mu\text{m}$  offset, and was observed to vary a little between successive cleaves.

The opposite trend – a progressive strengthening of the conversion with length – would be expected in the guides with negative values of the electrode offset, for which the electrode angular misalignment would cause an increase in offset with length. This trend was not demonstrated due to the limited measurement range available on those guides, which is discussed below. However, on the shorter lengths, for which the data for the positive and negative offsets can be compared, a stronger conversion is apparent for the positive values of offset. This observation tends to support the angular misalignment hypothesis.

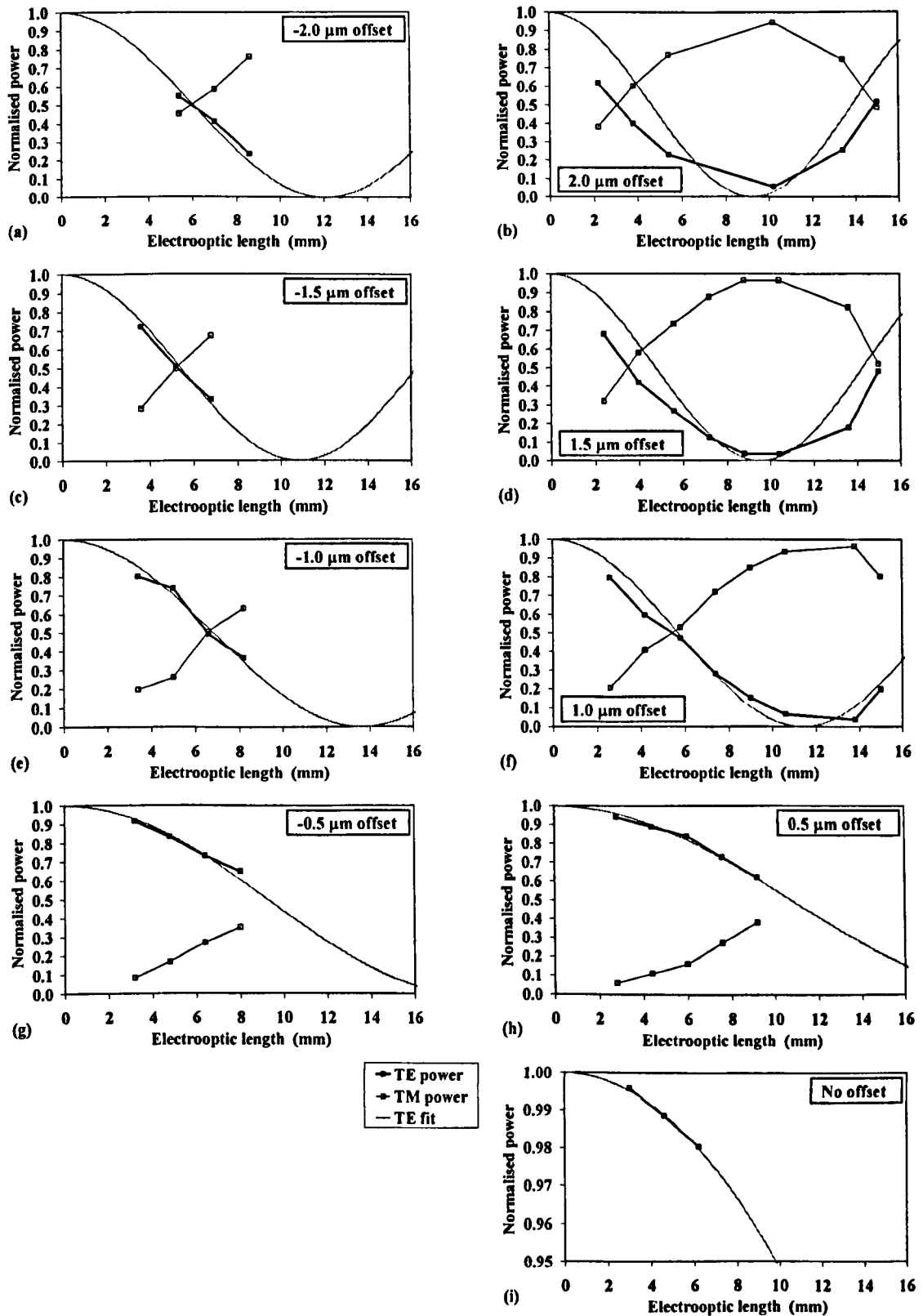


Fig. 5.9: TE and TM polarised components of optical power versus electrooptic length for various electrode offsets, measured at the phase-matching voltage. The electrode offsets are indicated on each plot, as follows: (a)  $-2.0 \mu\text{m}$ , (b)  $2.0 \mu\text{m}$ , (c)  $-1.5 \mu\text{m}$ , (d)  $1.5 \mu\text{m}$ , (e)  $-1.0 \mu\text{m}$ , (f)  $1.0 \mu\text{m}$ , (g)  $-0.5 \mu\text{m}$ , (h)  $0.5 \mu\text{m}$ , (i) no offset.



The measurement range was limited on some of the waveguides due to a break in the electrode, which reduced the available electrooptic length. Consequently, the full length of the electrode could not be contacted on the affected waveguides, so that measurements were not possible for the longer electrooptic lengths. The breaks resulted from a defect on the particular chip under test, which was the only available one of its kind. On this set of tests each electrode was addressed from a single bond pad connected at one end, so that no alternative means could be found of contacting the electrode sections isolated by the breaks. It was only after the sequential cleaving had removed all of the length beyond and including the defect that the expected change in the polarisation conversion was observed. The positions of the electrode breaks were observed using an optical microscope. These positions were found to correspond with the lengths beyond which the polarisation conversion did not proceed.

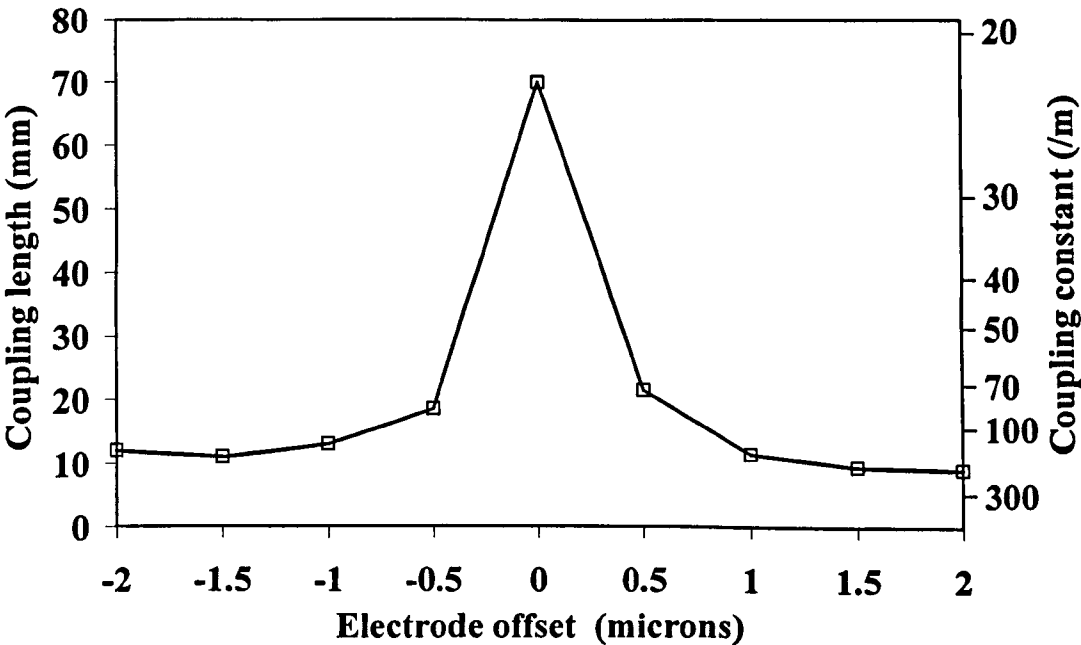


Fig. 5.10: Coupling length versus electrode offset for 5.2  $\mu\text{m}$  wide guides on wafer P0a, measured at the phase-matching voltage, typically 35 V. The corresponding coupling constant is indicated on the second vertical axis.

## 5.4 Conclusions

The influence of the electrooptic effect on polarisation conversion by modification of the modal index relationship has been investigated. Phase matching caused by alteration of the TE effective index relative to the TM index by the application of a vertical electric field has been demonstrated experimentally. It has been shown that for the simple epitaxy design P0, phase-matched conversion can occur in waveguides with a range of widths, extending beyond the full range intended for use in electrooptic waveguide devices. The propagation directions required to cause or prevent electrooptic phase matching for a given guide width have been identified. The strength of the linear electrooptic effect has been measured for wafer design P0, and the value has been used with measurements of the passive guide index difference to predict the phase-matching voltage as a function of guide width using a simple theory. Good agreement with directly measured data has been shown, including the zero phase-matching voltage at the passive critical guide width of  $\sim 3.63 \mu\text{m}$ . The form of the polarisation conversion as a function of applied voltage has been shown to match qualitatively the form as a function of  $\Delta\beta$  predicted by the coupled-mode theory. The suitability of the coupled-mode theory for the prediction of the behaviour of electrooptic guides with a known index relationship has therefore been shown.

An electrooptic coupling mechanism has been identified whereby an offset of the electrode with respect to the waveguide results in a net horizontal component in the applied electric field. Experimental results have been obtained to quantify the coupling constant due to this mechanism as a function of electrode offset, for one example of wafer design and guide width. For wafer design P0a with a guide width of  $5.2 \mu\text{m}$  and a phase-matching voltage of  $\sim 35 \text{ V}$ , the value of the coupling constant  $\kappa$  resulting from a  $0.5 \mu\text{m}$  offset is comparable with that resulting from a  $5^\circ$  parallel side-wall slant, approaching  $100 \text{ m}^{-1}$ . The value of  $\kappa$  reaches  $174 \text{ m}^{-1}$  when the electrode is aligned with one edge of the waveguide.

The results presented in this chapter provide further important information for the waveguide designer and the process engineer. For electrooptic waveguides, the wafer should be designed with a large index difference for the range of guide widths intended for use. The propagation direction should be chosen to increase the index difference rather than reduce it. The experimental examples given provide quantitative benchmarks.

## Chapter 6: Prevention of Polarisation Conversion

### 6.1 Purpose

The purpose of this section of work was to design and demonstrate epitaxy designs which prevented polarisation conversion from occurring even in the presence of a coupling mechanism, without affecting the following key parameters:

1. Waveguide width
2. Electrooptic depth
3. Optical loss per unit length
4. TE optical mode profile
5. Maximum Al fraction
6. Etch depth
7. Fabrication process

### 6.2 Wafer design theory

The use of planar dielectric stacks with boundaries parallel to the direction of propagation has been shown to create a birefringent medium, composed only of isotropic materials [149]-[152]. This induced anisotropy derives from the dielectric boundary conditions given previously in Table 2-I. The tangential component of an electric field is continuous across a boundary, while the normal component is increased by a factor of  $n_H^2/n_L^2$  on the lower index side of the boundary, where  $n_H$  and  $n_L$  denote the larger and smaller refractive indices respectively. With a greater field propagating in the lower index material, an optical electric field polarised normal to the boundary is subject to a lower refractive index than the orthogonal polarisation. By considering the behaviour of the slab waveguide in terms of this principle, an understanding may be obtained of how the waveguide design may be used to manipulate the index difference. A key fact is that the TM mode, for which the optical electric field is normal to the boundary, extends further into the low index cladding regions, and therefore has a smaller effective index. This permits several conclusions to be drawn qualitatively about the nature of rectangular waveguide mode indices, which are summarised below. The definition of index difference is recalled:  $\Delta n = n_{TM} - n_{TE}$ .

- When the waveguide width is large compared to the height, the properties tend towards those of a horizontal slab. The TM effective index is smaller than the TE index,  $\Delta n < 0$ . The opposite would be the case for a simple vertical slab. As the waveguide width is

reduced, the influence of the vertical boundaries increases, and the behaviour tends more towards that of the vertical slab. The TE index decreases more rapidly than the TM index, and may become the smaller of the two. This occurs in wafer P0 for guide widths smaller than the phase-matching width,  $W_{PM} \sim 3.63 \mu\text{m}$ .

- Reducing the core thickness increases the influence of the horizontal boundaries, making the index difference more negative for all guide widths.  $W_{PM}$  is reduced.
- Reducing the etch depth, so that it does not extend below the core, reduces the influence of the vertical boundaries, making the index difference more negative. The effect is stronger on narrower guides, for which the vertical boundaries have greater influence.
- Increasing the number and index contrast of the horizontal boundaries increases their influence, particularly if boundaries are added in the centre of the waveguide core where the optical field is largest. This makes the index difference more negative for all guide widths, and  $W_{PM}$  shifts to a narrower guide width.

This final point indicates a means to control the index relationship while potentially meeting all of the criteria set out in section 6.1, and provides the basis for the waveguide designs investigated in this chapter.

## 6.3 Experiments

### 6.3.1 Test wafer epitaxy design

Two wafers with different epitaxial layer specifications were designed with the purpose of preventing polarisation conversion. Wafer P0 was used as the control, providing values for the reference parameters stated in section 6.1. The three designs are detailed in Table 6-I. The two experimental wafers were designed with the aim of altering the polarisation behaviour without affecting the parameters listed. The core and cladding layer thicknesses, the electrooptic depth, and the etch depth of  $4 \mu\text{m}$  were not changed from those of wafer P0. The main feature of the test wafers was the introduction of additional AlGaAs layers within the waveguide core. Because this has the effect of lowering the core index, it was necessary to adjust the cladding layers to prevent the mode cut-off points shifting to larger guide widths. Compensation was achieved by increasing the aluminium fraction of the main cladding layers from 20% to 30% and increasing that of the bottom cladding layer from 6% to 9%. During the design process, two in-house mode solvers were used with the modified Afromowitz index data. The effective index method programme was used to model the indices, while optical loss due to leakage into the substrate was predicted using the spectral index method programme.

A comparison of effective index method simulations of index difference versus of guide width for the three wafer designs is shown in Fig. 6.1. The curve for P0 was discussed in detail in chapter four. It indicates that phase matching is expected at  $W_{PM} = 4.1 \mu\text{m}$ . Wafer P1 was designed to shift  $W_{PM}$  to a guide width of around  $2.2 \mu\text{m}$ . This is well outside the useful range of widths, but not so narrow as to prevent measurement of the polarisation behaviour. The index difference within the useful range of guide widths is increased by a substantial factor. The shift is achieved by placing a 50% AlGaAs layer in the middle of the core. Such a composition is at the limit of Al concentrations preferred for use in devices of this kind. High Al fractions are susceptible to increased background doping densities and oxidation of the aluminium [147]. Some disruption of the fundamental mode profile may also be expected. Wafer P2 was designed as a compromise, having a pair of 8.5% Al layers in the waveguide core, but with  $W_{PM}$  expected at around  $3.2 \mu\text{m}$ .

### 6.3.2 Experimental device design and fabrication

Wafers P1 and P2 were fabricated as part of the same batch as wafer P0 using an identical process and mask set, as described in chapter three. The passive and electrooptic waveguide test sets described in previous chapters were characterised for each wafer.

Layer	Design P0		Design P1		Design P2		Doping
	Depth ( $\mu\text{m}$ )	Al fraction	Depth ( $\mu\text{m}$ )	Al fraction	Depth ( $\mu\text{m}$ )	Al fraction	
Cap	0.1	0	0.1	0	0.1	0	Intrinsic
Upper cladding	1.2	0.2	1.2	0.3	1.2	0.3	Intrinsic
Core	2.0	0	0.95	0	0.5	0	Intrinsic
					0.3	0.085	
			0.1	0.5	0.4	0	
			0.95	0	0.3	0.085	
					0.5	0	
1 <sup>st</sup> lower cladding	0.2	0.2	0.2	0.3	0.2	0.3	Intrinsic
2 <sup>nd</sup> lower cladding	0.5	0.3	0.5	0.3	0.5	0.3	n+
3 <sup>rd</sup> lower cladding	3.8	0.06	3.6	0.09	3.6	0.09	n+
Substrate	650	0	650	0	650	0	Intrinsic

Table 6-I: Wafer specifications P0, P1 and P2. Layer depths, Al fractions and doping for the wafers fabricated for use in experiments.

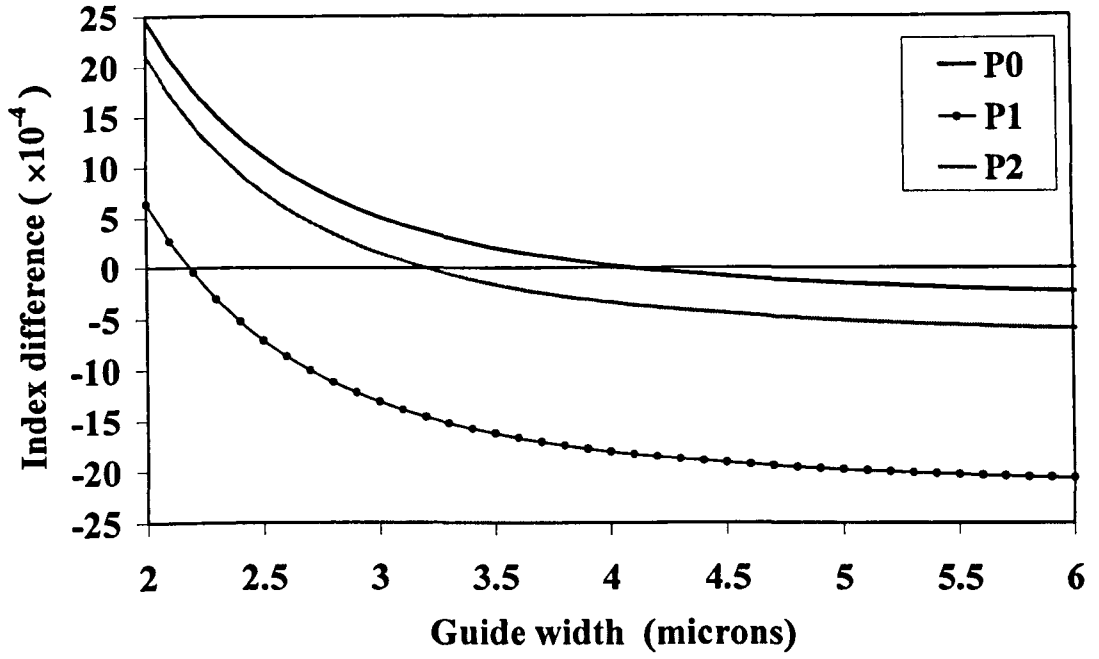


Fig. 6.1: Effective index method simulations of effective index difference ( $n_{TM} - n_{TE}$ ) versus guide width for wafers P0, P1 and P2, obtained using the modified Afromowitz refractive index data.

### 6.3.3 Experimental methods

Waveguide test sets were characterised using a number of techniques detailed in previous chapters, to obtain the following data: optical loss versus guide width; index difference versus guide width for passive waveguides with symmetric cross section; polarisation extinction versus guide width for passive waveguides with asymmetric cross section; phase-matching voltage versus guide width for electrooptic waveguides with asymmetric cross section.

The output mode profiles were observed using a Spiricon Pyrocam III  $\text{LiTaO}_3$  pyroelectric camera with an array size of 12.4 mm square and an element pitch of 100  $\mu\text{m}$ . The TE polarised waveguide output was imaged onto the array with a magnification of 2250. A narrow guide width of 3  $\mu\text{m}$  was chosen to ensure that only the fundamental mode was represented in the output.

## 6.4 Experimental results and comparisons

### 6.4.1 Optical loss measurements

The measured values of optical loss versus guide width for the three wafer designs are plotted in Fig. 6.2a for the TE fundamental mode and Fig. 6.2b for the TM fundamental mode. The losses are typically in the range  $0.4$  to  $0.8 \text{ dBcm}^{-1}$  for the useful range of guide widths, where the lower figure is considered representative because the Fabry-Pérot fringe visibility that provides the measurement is easily compromised by residual higher order mode content in the output. Figure 6.2a shows that the TE fundamental mode is subject to increasing loss as the guide width becomes narrower than  $3.0 \text{ }\mu\text{m}$ , and the mode cuts off at around  $2.0 \text{ }\mu\text{m}$ . The losses for TE and TM modes are almost identical. It is apparent that the test epitaxy designs P1 and P2 were successful in meeting the criteria that their optical loss per unit length and fundamental mode cut-off guide width should be similar to those of the standard wafer P0. It may be implied from these results that the higher order mode losses and cut-off widths are also very similar for the three designs.

### 6.4.2 Output mode profile observations

The measured TE fundamental mode intensity profiles for the three wafer designs are shown in Fig. 6.3, with the horizontal and vertical scales showing the dimensions of the camera array. Horizontal and vertical central cross section intensity distributions are indicated by the line plots, which are normalised. The images show no significant differences between the mode shapes for the three wafers. In particular, the result for wafer P1 shown in Fig. 6.3b does not show disruption of the vertical cross section intensity distribution around the peak, which corresponds with the position of the thin 50% AlGaAs layer in the core. It is therefore concluded that the criterion for preservation of the mode profile set out in section 6.1 is met by the test wafer designs.

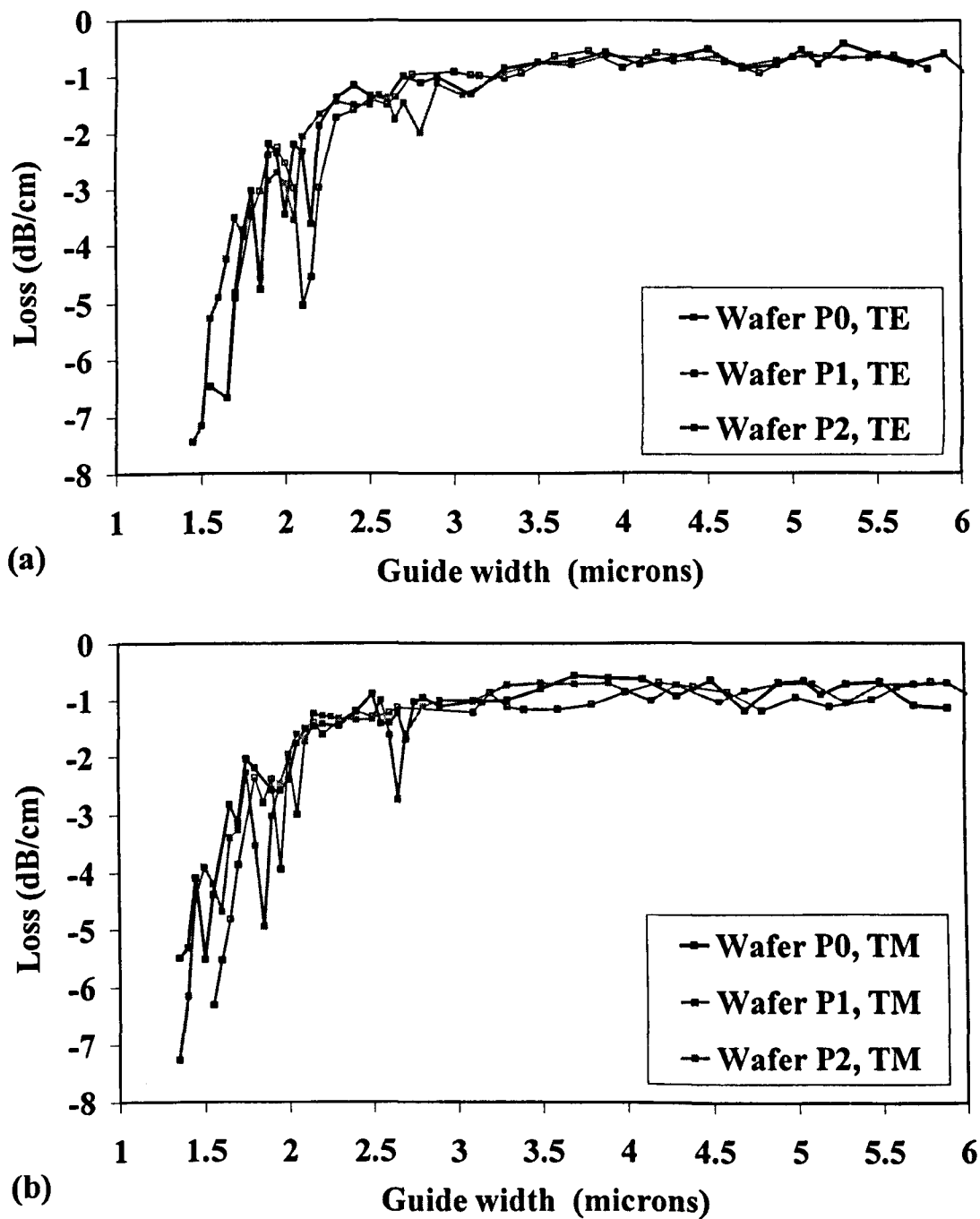


Fig 6.2: Measured optical loss versus guide width. Comparison of data for wafers P0, P1 and P2. (a) TE fundamental mode and (b) TM fundamental mode.



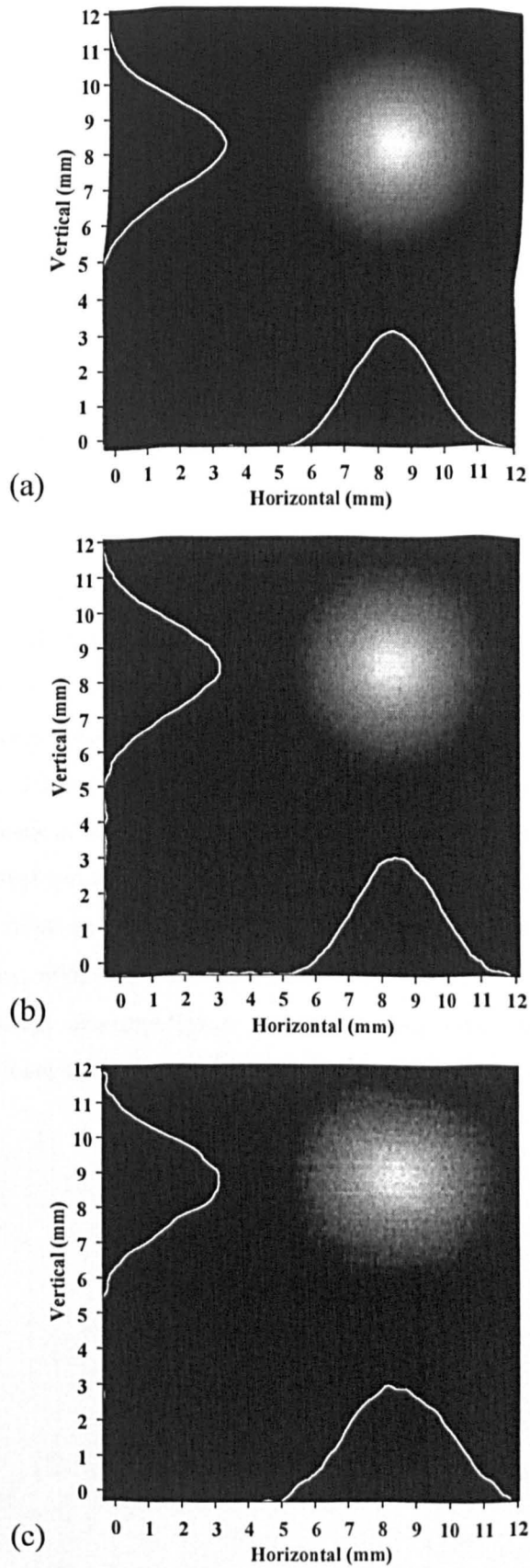


Fig. 6.3: Measured fundamental TE mode intensity profiles, nominal waveguide width  $3.0\ \mu\text{m}$ , for: (a) wafer P0, (b) wafer P1, (c) wafer P2. Normalised horizontal and vertical cross section intensity distributions are shown, which were measured through the centre of the mode. The scales show the camera array dimensions. The modes were imaged using a magnification of 2250.

### 6.4.3 Index difference results

Measured values of index difference in symmetric waveguides are plotted versus waveguide width for wafers P0, P1 and P2 in Figs. 6.4a, 6.4b and 6.4c respectively. Effective index method simulations obtained using four sets of published GaAs/AlGaAs refractive index data are included for comparison. The data in Fig. 6.4a is recalled from chapter four, but is re-plotted on the same scales as Figs. 6.4b and 6.4c for direct comparison. The measured values for wafer P2 show phase matching at a guide width of 2.7  $\mu\text{m}$ . For wafer P1,  $W_{PM}$  is measured to be 2.0  $\mu\text{m}$ . These results confirm that the wafer designs successfully demonstrate the principle of shifting  $W_{PM}$  away from the useful range of guide widths by the addition of horizontal boundaries. It is also noted that as  $W_{PM}$  shifts to narrower guides, the gradient of the index difference with respect to guide width increases.

For all three wafer designs, phase matching occurs at a narrower width than that predicted using the modified Afromowitz index data set. For wafer P2, the Gehrsitz index data provides the best match, both in terms of the prediction of  $W_{PM}$  and in the magnitude of the index difference across the full measured range. For wafer P1, none of the data sets provides a good match. Greater uncertainty is to be expected at the very narrow guide widths measured as any increment in the guide dimensions represents a larger fraction of the whole. Additionally, the narrower guides measured on wafer P1 were subject to increasingly strong mode leakage into the substrate, being below cut-off. This fact is not completely accounted for in the effective index method. For all wafers, the guide widths were measured to 0.1  $\mu\text{m}$  accuracy, while the SIMS characterisation of wafer layer thicknesses and Al fractions confirmed only insignificant deviations from the specification.

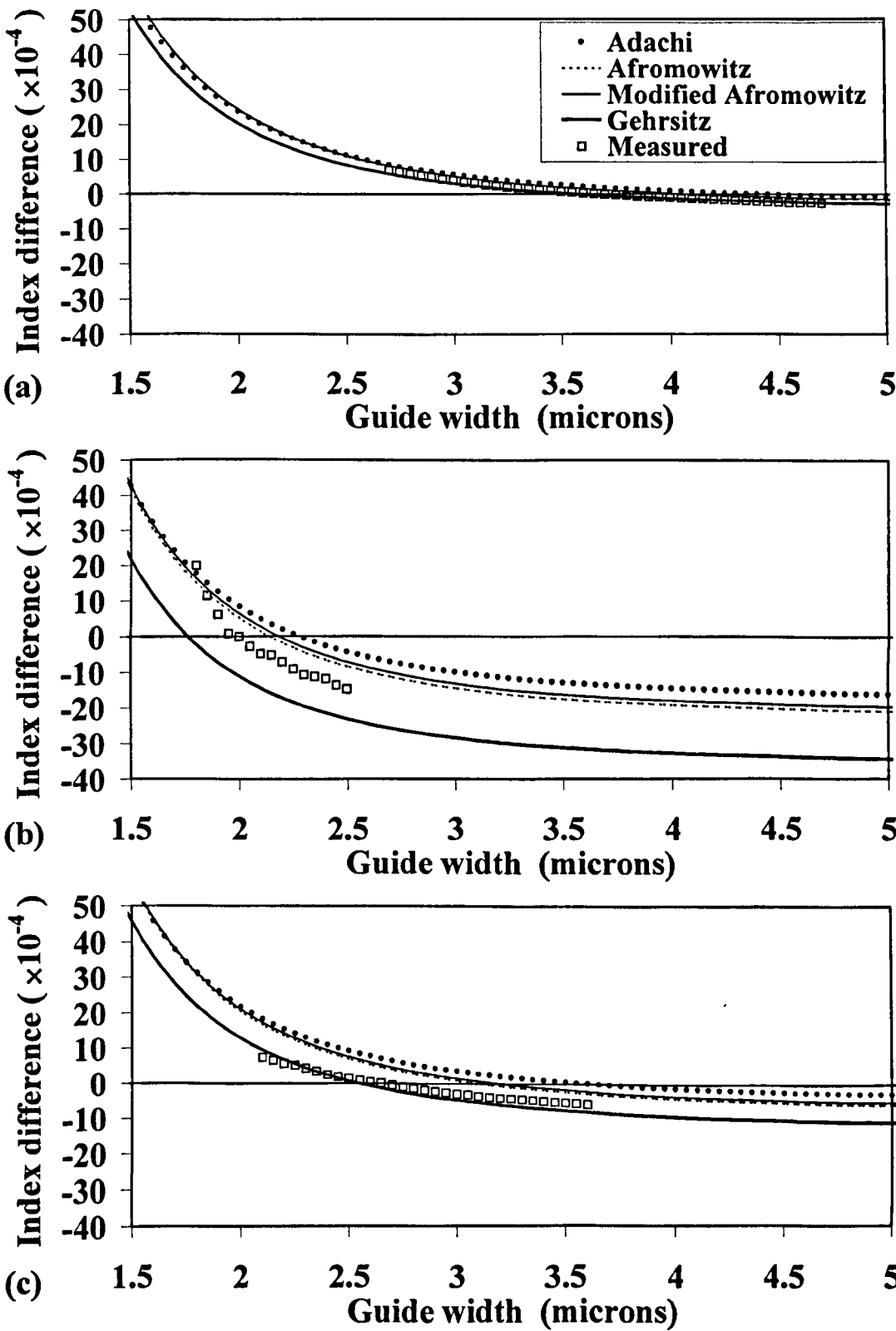


Fig. 6.4: Measured values of index difference versus waveguide width for symmetric waveguides. Comparison with effective index method simulations for several sets of published index data. (a) Wafer P0, (b) wafer P1, (c) wafer P2.

#### 6.4.4 Passive waveguide polarisation conversion results

Fig. 6.5 shows TE/TM polarisation extinction versus guide width for passive waveguides with asymmetric cross section on wafer P1. The five plots were obtained from measurements on different lengths of guide ranging from 10.0 mm to 1.25 mm. The same set of guides was used throughout, and was progressively shortened by sequential cleaving. The results have the familiar form described in detail for wafer P0 in chapter four. Strong polarisation conversion progresses at the phase-matching width, which is confirmed as  $2.0\ \mu\text{m}$ . The coupling length is approximately 3 mm, after which the light couples back to TE polarisation. Subsequent coupling to TM occurs so that in the measurement for a 10 mm length, shown in Fig. 6.5e, the majority of the power is found in the TM polarisation. The side lobes are apparent for the shorter lengths of the wider guides. Undersampling of the peaks occurs for narrower guides and for all guides longer than 5 mm, because of the rapid variation of the index difference with respect to guide width.

Despite the very strong conversion at phase matching, it is seen that for guide widths of  $2.4\ \mu\text{m}$  and wider, the TE input polarisation is preserved at the output with an extinction of greater than 20 dB for all lengths. This is a key result in the demonstration of the prevention of polarisation conversion for the useful guide width range of 3-5  $\mu\text{m}$ .

The corresponding data for wafer P2 are shown in Fig. 6.6, for propagation lengths ranging from 2.5 mm to 15.0 mm. The passive phase-matching guide width is confirmed as  $2.7\ \mu\text{m}$ . For this wafer the results indicate a coupling length of 10.5 mm. The side lobes, which are again clearly visible, are slightly asymmetric either side of phase matching because the data are plotted against guide width rather than  $\Delta\beta$ . Polarisation preservation of 20 dB or better is shown for guide widths of  $3.3\ \mu\text{m}$  and larger.

The values of passive phase-matching guide width  $W_{PM}$ , coupling length at phase matching  $z_{PM}$  and coupling constant  $\kappa$  for asymmetric passive guides on the three test wafers are summarised in Table 6-II.

Wafer	$W_{PM}$ ( $\mu\text{m}$ )	$z_{PM}$ (mm)	$\kappa$ ( $\text{m}^{-1}$ )
P0	3.63	17	93
P1	2.0	3	524
P2	2.7	10.5	150

Table 6-II: Comparison of measured polarisation conversion parameters for passive waveguides with asymmetric cross section for three test wafer designs.

There is a significant variation in the magnitude of  $\kappa$  between the three wafers. Although the side-wall slant angle could not be measured accurately, SEM observations indicated that the asymmetric cross sections were repeatably produced. The wafers had undergone identical processing. It is therefore clear that the value of  $\kappa$  is dependent on the guide width, increasing significantly as the guide width decreases. This may be understood as a result of the increased interaction between the light and the slanted side walls in narrower waveguides.

This fact presents a limitation of the coupled-mode theory in its simplest form as presented, which requires a single value of  $\kappa$  for all guide widths. It is concluded that the coupled-mode theory is only valid quantitatively for limited ranges of guide widths, with values toward the upper end of the those examined.

In principle the continuous variation of  $\kappa$  with guide width can be obtained from a single wafer by equating the expression for the coupling lengths at all guide widths for asymmetric waveguides with that provided by the coupled-mode theory. These are given by equations (6.1) and (6.2) respectively, where the subscript  $\theta$  indicates slanted side-walls and  $\perp$  denotes the assumption of TE and TM modes required by the coupled-mode theory, or symmetric waveguides. The resulting equation for  $\kappa$  as a function of the index difference in symmetric and asymmetric guides is given in equation (6.3).

$$z_c = \frac{\lambda_0}{2\Delta n_\theta}, \quad z_c = \frac{\pi}{2\sqrt{\kappa^2 + \frac{\Delta\beta_\perp^2}{4}}} \quad (6.1), (6.2)$$

$$\kappa = \sqrt{\left(\frac{\pi^2}{\lambda_0}\right)^2 (\Delta n_\theta^2 - \Delta n_\perp^2)} \quad (6.3)$$

However, the validity of this calculation is dependent on the assumption that the minimum index difference for the asymmetric waveguide occurs exactly at the phase-matching guide width of the symmetric guide. The calculation is very sensitive to deviations from this condition, which prevents meaningful results being obtained either from measured data or from FMM method simulations.

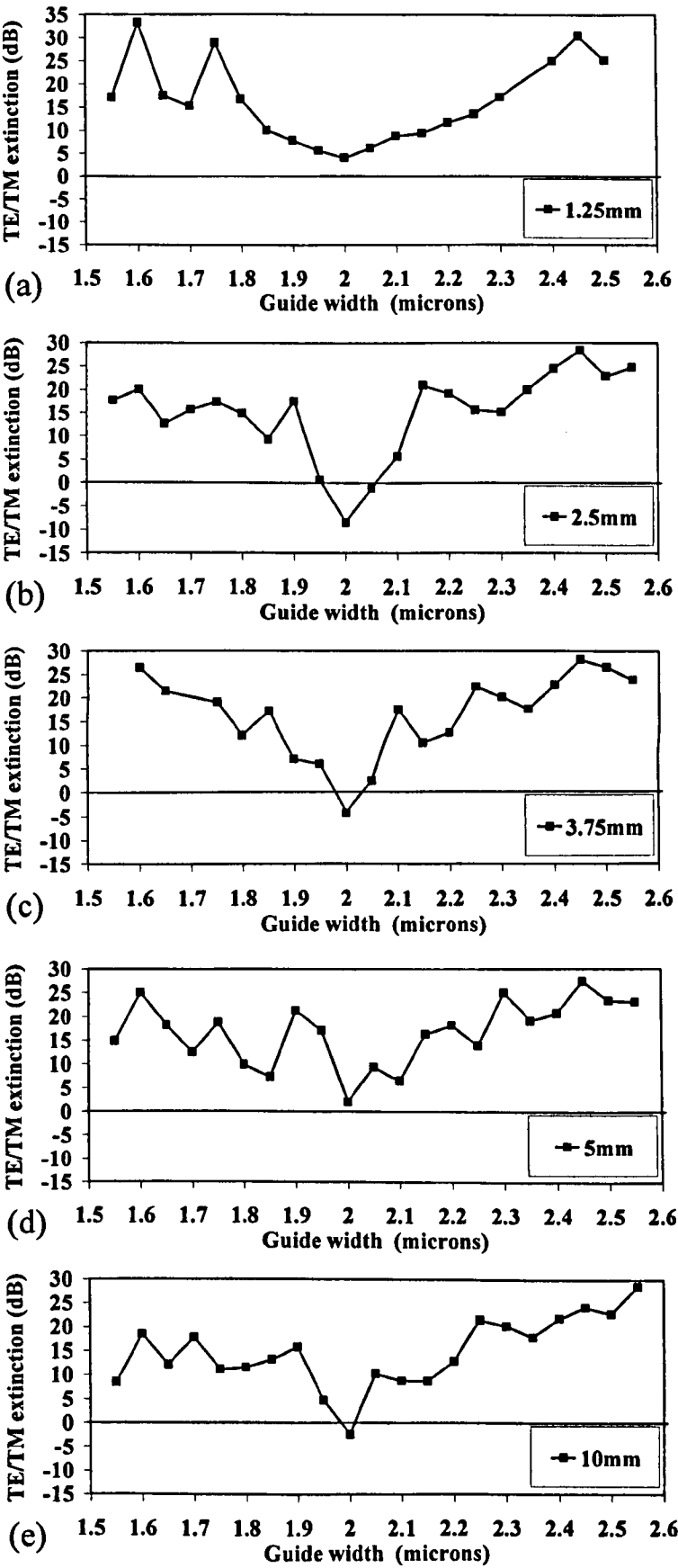


Fig. 6.5: Measured polarisation extinction versus guide width for asymmetric waveguides on wafer P1. Guide lengths: (a) 1.25 mm, (b) 2.5 mm, (c) 3.75 mm, (d): 5.0 mm, (e) 10.0 mm.

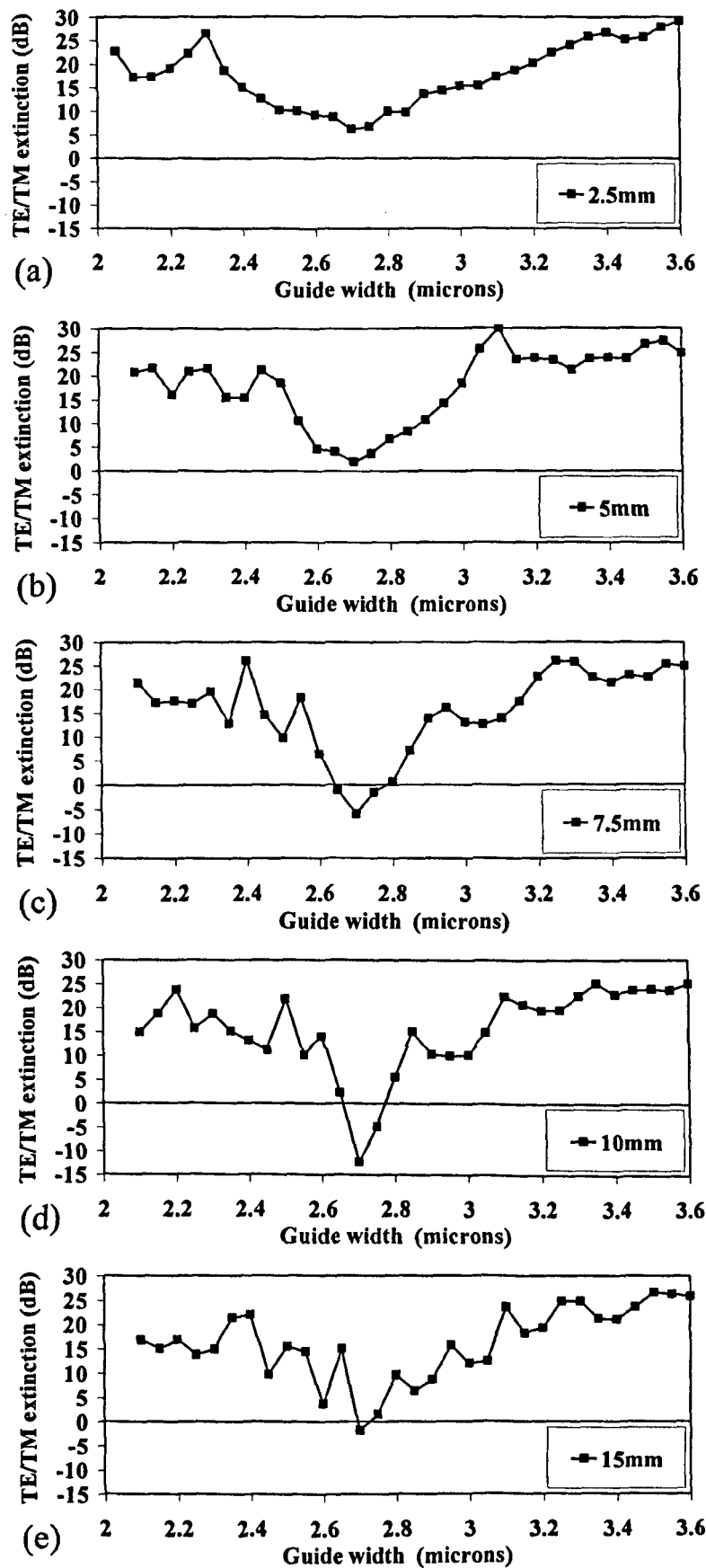


Fig. 6.6: Measured polarisation extinction versus guide width for asymmetric waveguides on wafer P2. Guide lengths: (a) 2.5 mm, (b) 5.0 mm, (c) 7.5 mm, (d) 10.0 mm, (e): 15.0 mm.

#### 6.4.5 Electrooptic waveguide results

Figs. 6.7a and 6.7b show the predicted values of  $V_{PM}$  versus guide width for wafers P1 and P2 respectively. These were calculated from equation (5.6) using the measurements of the index difference in symmetric guides and the specific electrooptic parameter, which was measured on wafer P0. This value was also used in the absence of measured values for wafers P1 and P2. Fig. 6.7b includes two data points of directly measured values of  $V_{PM}$  for wafer P2, showing quite good agreement with the predictions. No direct measurements were obtained on wafer P1 because phase matching was not observed. The value of the  $V_{PM}$  for the available guide widths far exceeded the reverse bias breakdown voltage.

The results for wafer P1 show that phase-matched polarisation conversion was prevented for the target guide width range of 3-5  $\mu\text{m}$ , regardless of propagation direction. On wafer P2,  $V_{PM}$  was greater than 30 V for all guide widths in the useful range. It was shown that if  $[0\bar{1}1]$  propagation is selected, phase-matched polarisation conversion cannot occur.

The adequacy of wafer P2 for the prevention of polarisation conversion is further demonstrated by the result shown in Fig. 6.8. Normalised output power with TE and TM polarisations is plotted versus reverse bias voltage, for an electrooptic waveguide with a measured width of 3.6  $\mu\text{m}$  and a length of 2 cm. Although more than 50 % coupling occurs at the phase-matching voltage of 69 V, the TE input polarisation is preserved at the output to greater than 23 dB for voltages smaller than 50 V. This result indicates that most of the useful guide width range is safe from unwanted polarisation conversion despite the use of the  $[011]$  propagation direction.



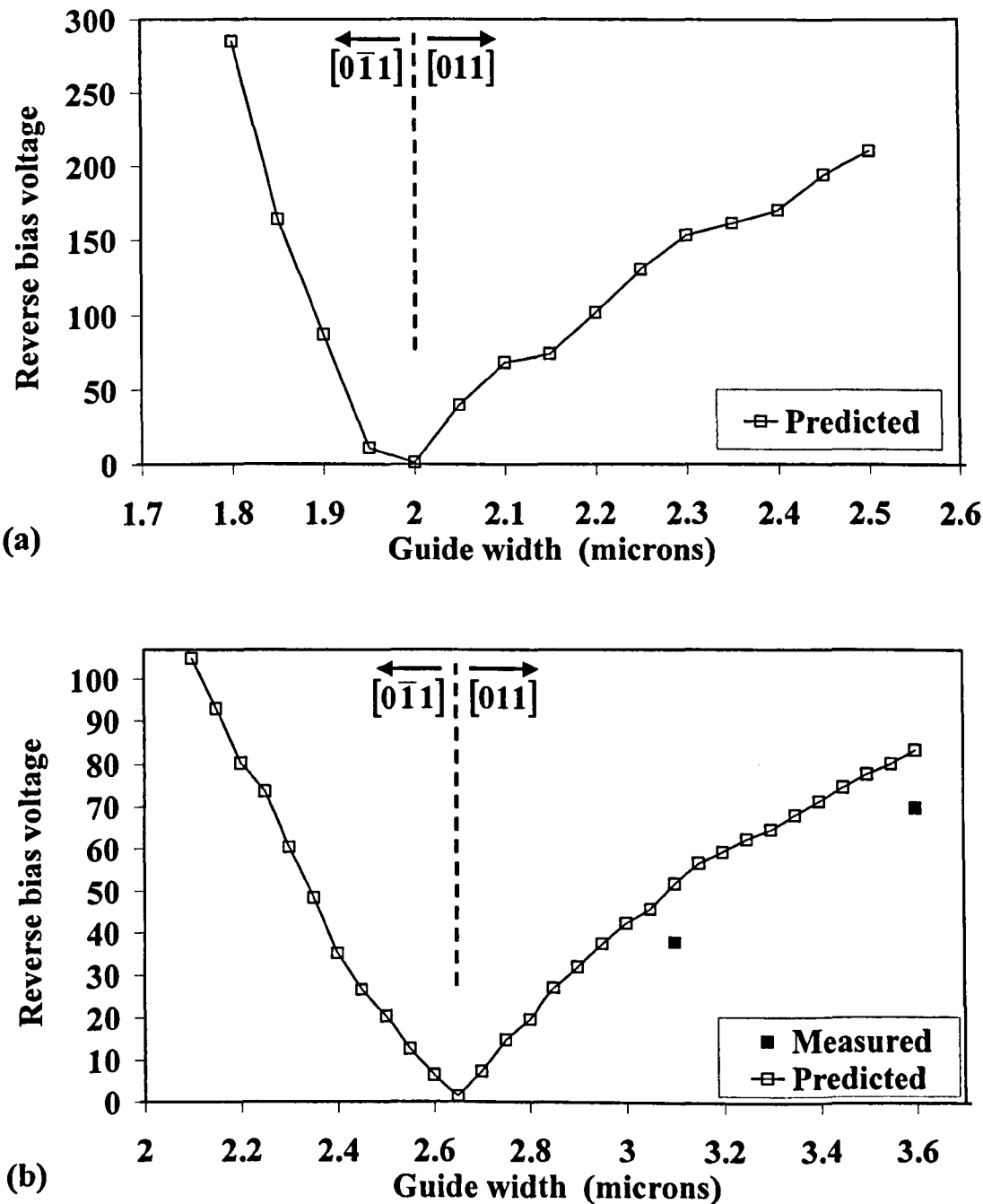


Fig. 6.7: Phase-matching voltage versus guide width. (a) Wafer P1, predicted values; (b) wafer P2, measured and predicted values. The propagation directions are indicated. The predicted values were calculated using measurements of index difference.

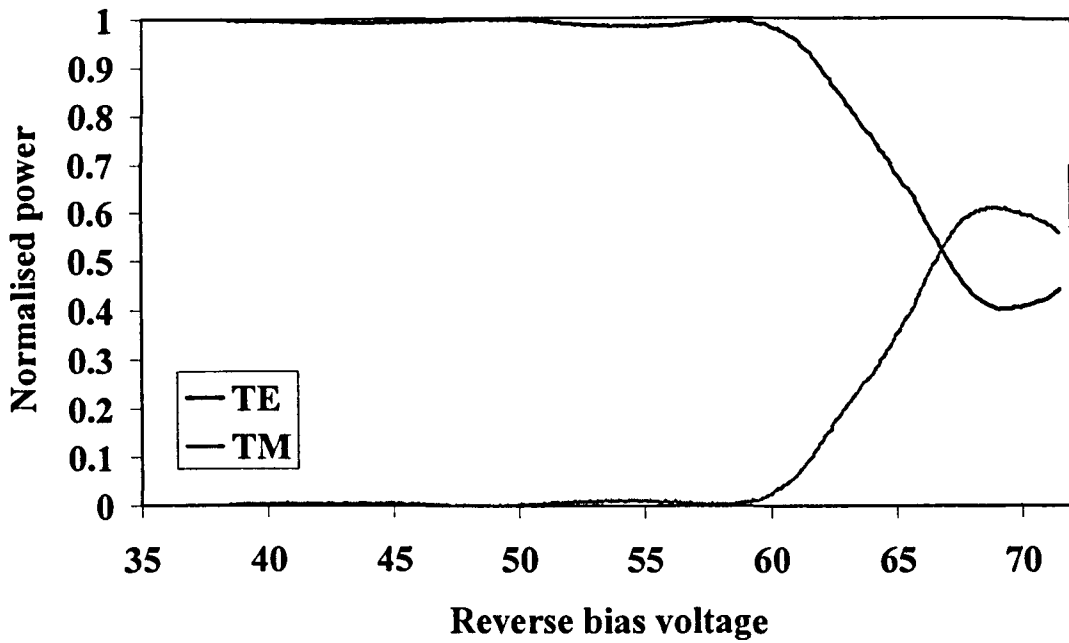


Fig. 6.8: Normalised output power with TE and TM polarisations versus reverse bias voltage, for an electrooptic waveguide on wafer P2, width  $3.6\ \mu\text{m}$ , length 2 cm. The input polarisation is preserved to greater than 23 dB for voltages less than 50 V, despite phase-matched conversion at 69 V.

## 6.5 Conclusions

A design technique for the prevention of polarisation conversion in the presence of a coupling mechanism has been demonstrated. The principle of placing additional AlGaAs layers in the waveguide core was used to move the phase-matching guide width out of the useful range. Two test wafers, P1 and P2, were fabricated which exhibited critical widths  $W_{PM}$  of  $2.0\ \mu\text{m}$  and  $2.7\ \mu\text{m}$  respectively, compared to  $\sim 3.63\ \mu\text{m}$  for the control wafer P0. In passive waveguides exhibiting slanted side walls and strong phase-matched coupling, preservation of the TE input polarisation was demonstrated in guides with a large phase mismatch. An extinction of greater than 20 dB for all lengths was observed for guide widths of  $2.4\ \mu\text{m}$  and wider on wafer P1, and  $3.3\ \mu\text{m}$  and wider on wafer P2.

The immunity of the designs to electrooptically phase-matched polarisation conversion was investigated. For waveguides with widths in the specified useful range of  $3\text{--}5\ \mu\text{m}$ , it was shown that in wafer P1 phase matching could not be induced by the linear electrooptic effect. In wafer P2 at least 30 V was required to cause phase-matched polarisation conversion, which could only occur for [011] propagation, while guides wider than  $4\ \mu\text{m}$  were not susceptible.

The designs were constrained by the requirement to be identical to the control wafer in certain parameters. The fabrication process, electrooptic depth and optical mode size were all

maintained, and conservative AlGaAs compositions were used. A maximum Al fraction of 50% was used in wafer P1, while the upper limit of 30% used in P0 was not exceeded in wafer P2. Measurements of optical loss showed very little variation of loss per unit length and fundamental mode cut-off guide width between the three designs. No significant disruption of the fundamental mode profile was observed in the test wafers.

These results show how the problem of unwanted polarisation conversion can be prevented by careful design of the wafer epitaxy without additional process development, and without compromising the main device parameters. The examples given provide experimental verification of the modelling techniques used to obtain the designs.

A limitation of the applicability of the coupled-mode theory to the problem of polarisation conversion in passive waveguides was raised by the measured variation of the coupling constant with guide width, without variation of the side-wall slant angle which provided the coupling mechanism. This coupling constant variation was particularly apparent in very narrow waveguides. The limitation is confined to the situation where the variation in  $\Delta\beta$  is controlled by the guide width, rather than by the linear electrooptic effect. It was concluded that the coupled-mode theory is only valid quantitatively over ranges of guide width that do not amount to a significant fraction of the width.

## Chapter 7: Electrooptic Polarisation Controller

This chapter describes the first experimental demonstration of a novel electrooptic waveguide arbitrary polarisation controller, which is fabricated using a standard process and can therefore be integrated with other components.

### 7.1 Device concept

It was shown in chapter five that complete polarisation conversion from TE to TM can occur in an electrooptic waveguide in which the electrode is offset with respect to the waveguide. If the electrode offset provides the only coupling mechanism, the polarisation conversion can be switched on and off, permitting voltage-controlled switching of the output state between linear horizontal and vertical states. However, this configuration does not give complete control of the polarisation because the coupling mechanism and phase relationship are both set by a single voltage. A working TE-TM switch design with this configuration would require very fine tolerances in fabrication to obtain the required coupling strength at the phase-matching voltage repeatably.

For complete control of the polarisation conversion process, it is necessary to separate the coupling mechanism from the phase relationship. This may be achieved by the independent application of the horizontal and vertical electric field components. A novel configuration that permits this control is shown in cross section in Fig. 7.1. It consists of a deep-etched waveguide as described earlier, but with two electrodes on the top surface rather than one, and a conducting region in the substrate. Two signal voltages may be applied to the two electrodes. To a first approximation, the mean of the two signal voltages defines the vertical electric field component, which controls the phase relationship; independently, the difference between the signal voltages provides the horizontal field, which controls the coupling constant. The fringing field resulting from a differential voltage applied between two conductors on a GaAs surface is shown schematically in Fig. 7.2.

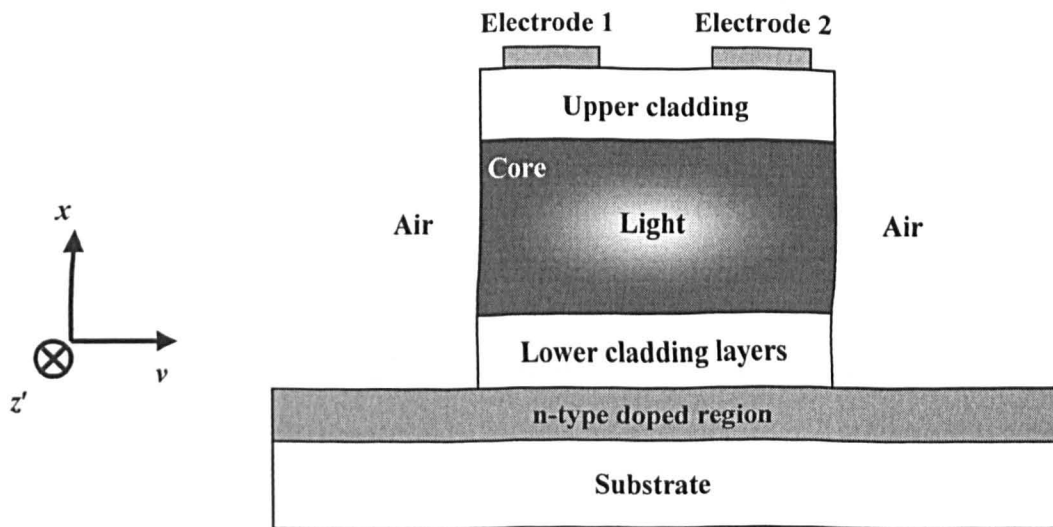


Fig. 7.1: Schematic diagram of the electrooptic waveguide polarisation controller cross section.

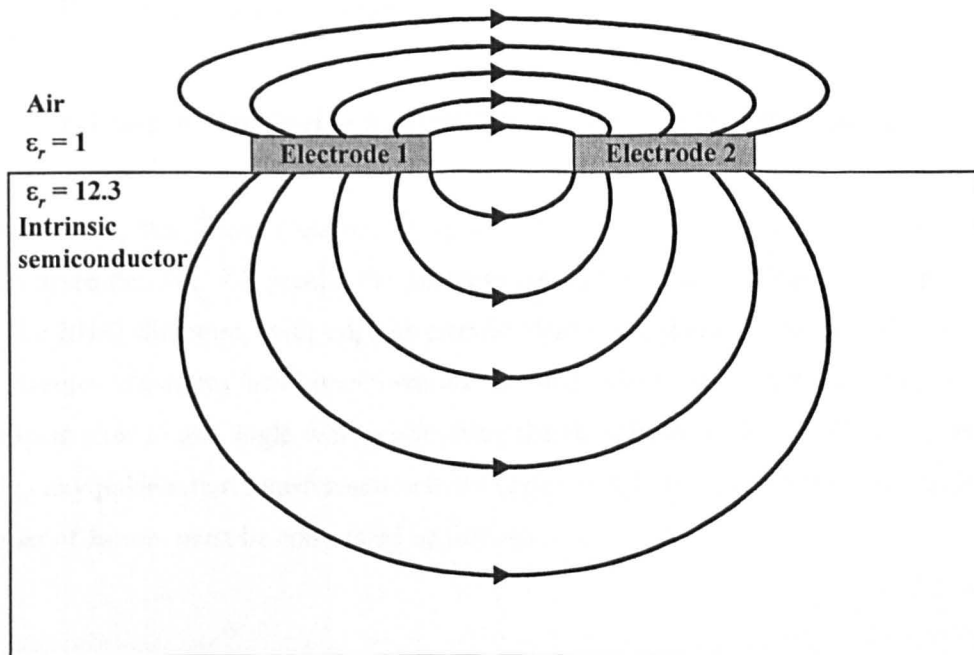


Fig. 7.2: Schematic diagram of the electric field resulting from a differential voltage applied between two conductors on a GaAs surface.

The operation of the device may be understood by considering in steps one example of the functions that it can perform. In order to convert a horizontal linearly polarised input state to a vertical linearly polarised output state, the phase-matching voltage is first applied equally to both top electrodes with respect to the substrate, thus creating a vertical electric field which alters the effective index of the TE mode to match it to that of the TM mode. The modes of the waveguide may now be considered to be polarised at angles of  $+45^\circ$  and  $-45^\circ$ . Next a differential voltage is applied between the two top electrodes, while maintaining the mean of

the voltages applied to the two electrodes at  $V_{PM}$ . This differential voltage creates a horizontal electric field component which induces a difference between the effective refractive indices of the  $\pm 45^\circ$  modes, resulting in a relative phase shift. Given a horizontal input polarisation, these modes contain equal amounts of power, which makes accurate conversion to a vertical output state possible. To do this, the differential voltage is chosen to produce a relative phase shift of  $\pi$  during propagation. The differential voltage may be switched on and off to give TE-TM switching, with the intermediate output states being a continuous set of elliptical states with constant azimuth of  $0^\circ$ . Possible output polarisations include states containing both horizontal and vertical components in any ratio. This example is not the only method of driving the device to give TE-TM switching, as will be discussed later. In general, the device may be used to perform any polarisation transformation. This is demonstrated in the following sections.

## 7.2 Theoretical analysis

### 7.2.1 Electrooptic waveguide birefringence control in two dimensions

In chapter two, the linear electrooptic effect was described for the general case of bulk gallium arsenide. Fig. 7.3 recalls the sections through the index ellipsoid for propagation along the  $[011]$  direction, with applied electric field components in the  $x$  and  $v$  directions. This diagram illustrates how combinations of field components may be used to set the birefringent axes to any angle while controlling the magnitude of the birefringence, therefore enabling any polarisation transformation to be performed. In the case of the waveguide device a number of factors must be considered as follows.

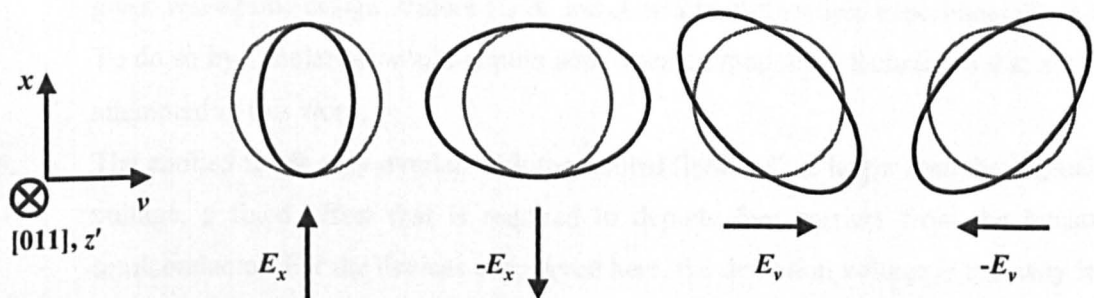


Fig. 7.3: Sections through the index ellipsoid for propagation along  $[011]$  in the presence of  $E_x$  and  $E_v$  applied field components.

1. The presence of the dielectric boundaries that form the rectangular waveguide cross section result in an effective birefringence, with modes that are polarised horizontally (TE) and vertically (TM) in the absence of an applied  $E_v$  component. It is possible to approximate the effect of the introduction of this effective birefringence by taking account of it in a modified ellipse equation for the waveguide.
2. The metal deposited on top of the waveguide forms a Schottky barrier diode, which must be reverse biased if the applied voltage is to be dropped fully across the optical region. It is therefore only possible to apply electric fields in the directions  $x$ ,  $v$ , and minus  $v$ .
3. In general, the applied field contains components in  $x$  and  $v$  that are not uniform across the waveguide cross section. It is therefore necessary to consider  $E_x$  and  $E_v$  as expressions of the mean of each respective field component throughout the waveguide cross section, weighted by the relative magnitude of the optical field at each point. The non-uniformity of the applied field does not alter the device behaviour by comparison with a hypothetical uniform-field example, because the effect of the refractive index profile on the optical mode is averaged out during propagation.
4. It is convenient to use a simplified means of defining how to calculate the effective field components from the applied voltages. We define  $V_x$  as the mean of the voltages applied to the two electrodes.  $E_x$  is then given by  $V_x/d_x$ , where  $d_x$  is a constant that expresses the electrooptic depth, equal to the separation of the metal electrode and the n-type conducting ground plane, modified slightly by the overlap of the optical field with these conducting regions.  $V_v$  is defined as the difference between the two voltages. To obtain  $E_v$ ,  $V_v$  is divided by the horizontal electrooptic width parameter,  $d_v$ , which is analogous with the electrooptic depth. This parameter takes account of the electrode separation and width, the shape of the horizontal electric field distribution and its overlap with the optical mode. It is assumed to be a constant for a given waveguide design. Values for  $d_x$  and  $d_v$  will be determined experimentally later. To do so by simulation would require sophisticated modelling techniques that are not attempted in this work.
5. The applied fields only overlap with the optical field if  $V_x$  is larger than the depletion voltage, a fixed offset that is required to deplete free carriers from the intrinsic semiconductor. For the devices considered here, the depletion voltage is typically less than 1 V, which is almost negligible. This value is typical of wafers with a GaAs core region grown by Molecular Beam Epitaxy (MBE), however it can be larger in other circumstances. The depletion voltage is neglected in the following discussion.

6. The assumption is made that the modes of the waveguide device have a polarisation which is uniform across the mode profile. Rigorous modelling shows that this is not strictly the case, but in practice the non-uniformity is small and the approximation is valid.

The ellipse equation is modified to take account of the effective birefringence of the passive waveguide by introduction of the effective indices of the TE and TM polarised fundamental modes:

$$\frac{x^2}{n_{\text{TM}}^2} + \frac{v^2}{n_{\text{TE}}^2} - r_{41} v^2 E_x - 2r_{41} x v E_v = 1 \quad (7.1)$$

This equation will now be used to derive expressions that describe polarisation control in GaAs waveguide devices, from which some design conditions will be obtained.

The directions of the electric field vectors of the two orthogonal polarised modes of the waveguide provide the effective principal dielectric axes. The device operation can be determined given these directions and the associated mode effective indices. To obtain these, the ellipse given in terms of  $x$  and  $v$  in equation (7.1) is expressed in terms of its major and minor axes, defined as the dielectric axes  $x'$  and  $y'$  (not necessarily respectively), which are inclined by an angle  $\theta$  relative to the  $x$  and  $v$  axes respectively. The ellipse equation will then have the simple form:

$$\frac{x'^2}{n_{x'}^2} + \frac{y'^2}{n_{y'}^2} = 1 \quad (7.2)$$

The axis substitution procedure is now repeated, with  $x$  and  $v$  now defined in terms of  $x'$  and  $y'$  as indicated in Fig. 7.4:

$$x = x' \cos \theta + y' \sin \theta \quad v = y' \cos \theta - x' \sin \theta \quad (7.3)$$

Substitution in the ellipse equation (7.1) gives:

$$K_1 x'^2 + K_2 y'^2 + K_3 x' y' = 1 \quad (7.4)$$

where  $K_1$ ,  $K_2$  and  $K_3$  have been defined as:

$$\begin{aligned} K_1 &= \frac{\cos^2 \theta}{n_{\text{TM}}^2} + \frac{\sin^2 \theta}{n_{\text{TE}}^2} - r_{41} E_x \sin^2 \theta + 2r_{41} E_v \cos \theta \sin \theta \\ K_2 &= \frac{\sin^2 \theta}{n_{\text{TM}}^2} + \frac{\cos^2 \theta}{n_{\text{TE}}^2} - r_{41} E_x \cos^2 \theta - 2r_{41} E_v \cos \theta \sin \theta \\ K_3 &= \frac{2 \sin \theta \cos \theta}{n_{\text{TE}}^2} - \frac{2 \sin \theta \cos \theta}{n_{\text{TM}}^2} + 2r_{41} E_x \cos \theta \sin \theta - 2r_{41} E_v (\cos^2 \theta - \sin^2 \theta) \end{aligned} \quad (7.5)$$



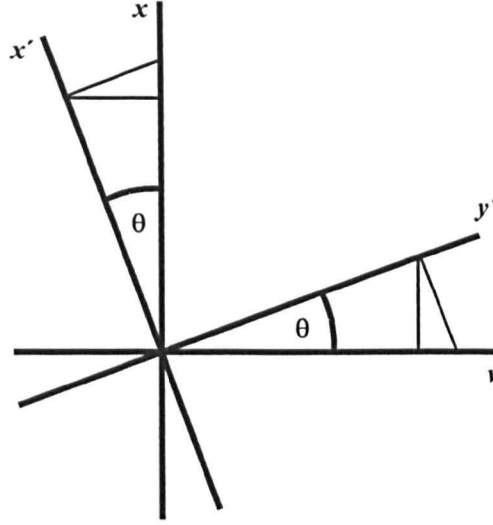


Fig. 7.4: The axis components for the coordinate transformation from the axes  $x$  and  $v$  to the new axes  $x'$  and  $y'$ .

In order for equation (7.4) to take the form of equation (7.2), the mixed term must be eliminated, for which  $\theta$  has the value such that  $K_3 = 0$ . Setting this condition and rearranging (7.5) gives:

$$\left( \frac{1}{n_{TM}^2} - \frac{1}{n_{TE}^2} + r_{41} E_x \right) \cos \theta \sin \theta = r_{41} E_v (\cos^2 \theta - \sin^2 \theta) \quad (7.6)$$

Employing the identities:

$$\sin A \cos A = \frac{\sin 2A}{2} \quad \cos^2 A - \sin^2 A = \cos 2A \quad \tan A = \frac{\sin A}{\cos A} \quad (7.7)$$

gives:

$$\theta = \frac{\tan^{-1} \left( \frac{2r_{41} E_v}{n_{TM}^{-2} - n_{TE}^{-2} + r_{41} E_x} \right)}{2} \quad (7.8)$$

while:

$$n_{x'} = \sqrt{\frac{1}{\left( \frac{\cos^2 \theta}{n_{TM}^2} + \frac{\sin^2 \theta}{n_{TE}^2} - r_{41} E_x \sin^2 \theta + 2r_{41} E_v \cos \theta \sin \theta \right)}} \quad (7.9)$$

$$n_{y'} = \sqrt{\frac{1}{\left( \frac{\sin^2 \theta}{n_{TM}^2} + \frac{\cos^2 \theta}{n_{TE}^2} - r_{41} E_x \cos^2 \theta - 2r_{41} E_v \cos \theta \sin \theta \right)}}$$

### 7.2.2 Conditions for arbitrary polarisation control

Inspection of equation (7.8) shows that the values of  $E_y$  and  $E_x$  required to obtain a given value of  $\theta$  are not restricted to a single combination. Different combinations may be used, giving a range of values of  $\Delta n$ . Thus  $\theta$  and  $\Delta n$  may be controlled independently. In order for the device to be capable of general polarisation transformations, that is the conversion of any input polarisation state to any output polarisation state, the following parameter ranges must be available with electrooptic control:

1. Mode angles  $\theta$  covering the range 0 to  $\pi/2$ .
2. Relative phase shift between the two modes of  $-\pi$  to  $\pi$  for all mode angles.

The limits could be written alternatively as  $-\pi/2$  to  $\pi/2$  and 0 to  $\pi$  respectively, with identical meaning. The range of values of  $E_x$  that may be applied is limited by the Schottky barrier diode reverse bias breakdown voltage, which is usually in the range 60 V to 80 V for a typical waveguide structure. As discussed previously, only positive values of  $E_x$  are available.  $E_y$  is limited by the breakdown voltage between the two electrodes on top of the waveguide. This has not been characterised fully, but the demonstrated device withstood differential voltages of greater than  $\pm 25$  V.

The condition for satisfaction of criterion 1 is obtained from equation (7.8):

$$0 \leq \left( \frac{2r_{41}E_y}{n_{TM}^{-2} - n_{TE}^{-2} + r_{41}E_x} \right) \leq \infty \quad (7.10)$$

$E_y$  can take positive and negative values regardless of device design details. To reach the limits, the denominator is required to cover a range which includes zero. Given the constraint that  $E_x$  can only take positive values, and recalling that  $r_{41}$  is negative in GaAs, the waveguide must be designed so that:

$$n_{TM}^{-2} - n_{TE}^{-2} > 0 \quad \text{i.e.} \quad n_{TE} > n_{TM} \quad (7.11)$$

The opposite condition applies in the case of propagation along the perpendicular crystal direction  $[0\bar{1}1]$ . This design condition is not sufficient to satisfy criterion 2. Further consideration is required. The phase difference is given by:

$$\Delta\phi_{x'y'} = \frac{2\pi L(n_{x'} - n_{y'})}{\lambda_0} \quad (7.12)$$

where  $L$  is the device length. Small index differences may be approximated by the relation:

$$n_{x'} - n_{y'} \approx -\frac{n_{\text{eff}}^3}{2} \left( \frac{1}{n_{x'}^2} - \frac{1}{n_{y'}^2} \right) \quad (7.13)$$

which is obtained from the differential relation  $dn = -(n^3/2)d(n^{-2})$ . The effective index  $n_{\text{eff}}$  is approximately equal to  $n_{x'}$  and  $n_{y'}$ . The index terms given in equation (7.9) may now be substituted in equation (7.13), which in turn is substituted in (7.12) whilst employing the identities given in (7.7) to give:

$$\Delta\phi_{x'y'} = \frac{-\pi L n_{\text{eff}}^3}{\lambda_0} \left( \left( \frac{1}{n_{\text{TM}}^2} - \frac{1}{n_{\text{TE}}^2} + r_{41} E_x \right) (\cos 2\theta) + 2r_{41} E_y (\sin 2\theta) \right) \quad (7.14)$$

Rearranging equation (7.10):

$$\sin 2\theta (n_{\text{TM}}^{-2} - n_{\text{TE}}^{-2} + r_{41} E_x) - \cos 2\theta (2r_{41} E_y) = 0 \quad (7.15)$$

Equations (7.14) and (7.15) form two simultaneous equations, which reduce to eliminate  $\theta$ :

$$(\Delta\phi_{x'y'})^2 = \left( \frac{-\pi L n_{\text{eff}}^3}{\lambda_0} \right)^2 \left( \left( \frac{1}{n_{\text{TM}}^2} - \frac{1}{n_{\text{TE}}^2} + r_{41} E_x \right)^2 + (2r_{41} E_y)^2 \right) \quad (7.16)$$

Recalling that the phase difference is required to take values in the range  $-\pi$  to  $\pi$  for all  $\theta$ :

$$-\frac{\lambda_0}{L n_{\text{eff}}^3} \leq \sqrt{\left( \left( \frac{1}{n_{\text{TM}}^2} - \frac{1}{n_{\text{TE}}^2} + r_{41} E_x \right)^2 + (2r_{41} E_y)^2 \right)} \leq \frac{\lambda_0}{L n_{\text{eff}}^3} \quad (7.17)$$

This gives the required parameter ranges, which can also be obtained by inspection of equation (7.14) as indicated in Table 7-I:

$\theta$	$2\theta$	$\sin 2\theta$	$\cos 2\theta$	Condition
0	0	0	1	$-\frac{\lambda_0}{L n_{\text{eff}}^3} \leq \left( \frac{1}{n_{\text{TM}}^2} - \frac{1}{n_{\text{TE}}^2} + r_{41} E_x \right) \leq \frac{\lambda_0}{L n_{\text{eff}}^3}$
$\pi/4$	$\pi/2$	1	0	$-\frac{\lambda_0}{L n_{\text{eff}}^3} \leq (2r_{41} E_y) \leq \frac{\lambda_0}{L n_{\text{eff}}^3}$
$\pi/2$	$\pi$	0	-1	$-\frac{\lambda_0}{L n_{\text{eff}}^3} \leq \left( \frac{1}{n_{\text{TM}}^2} - \frac{1}{n_{\text{TE}}^2} + r_{41} E_x \right) \leq \frac{\lambda_0}{L n_{\text{eff}}^3}$

Table 7-I: Parameter ranges required for arbitrary polarisation control.

Once again recalling that  $r_{41}$  is negative, the parameter values required for universal polarisation control (for [011] propagation) are:

$$\frac{1}{n_{\text{TM}}^2} - \frac{1}{n_{\text{TE}}^2} \geq \frac{\lambda_0}{L n_{\text{eff}}^3} \quad (7.18)$$

$$E_{xmin} = \frac{V_{xmin}}{d_x} = - \left( \frac{n_{TM}^{-2} - n_{TE}^{-2}}{r_{41}} - \frac{\lambda_0}{r_{41} L n_{eff}^3} \right)$$

$$E_{xmax} = \frac{V_{xmax}}{d_x} = - \left( \frac{n_{TM}^{-2} - n_{TE}^{-2}}{r_{41}} + \frac{\lambda_0}{r_{41} L n_{eff}^3} \right) \quad (7.19)$$

$$E_{vmin} = \frac{V_{vmin}}{d_v} = \frac{\lambda_0}{2r_{41} L n_{eff}^3} \quad E_{vmax} = \frac{V_{vmax}}{d_v} = - \frac{\lambda_0}{2r_{41} L n_{eff}^3} \quad (7.20)$$

### 7.2.3 Transformation matrices

#### 1. General polarisation controller

The description of a general polarisation converter involves the following stages: coordinate transformation of the input state, expressed in terms of vertical and horizontal optical field components  $A_x$  and  $A_v$ , to the new axes  $A_{x'}$  and  $A_{y'}$  coinciding with the modes of the device; propagation of the modes of the device, with phase difference accumulated due to the different effective indices of the modes; coordinate transformation to express the output state in terms of  $A_x$  and  $A_v$ . Multiplying the  $2 \times 2$  matrices corresponding to these three stages given in chapter two gives the following transformation matrix for the general polarisation controller, in which the subscript has been omitted from  $\Delta\phi_{x'y'}$ :

$$T_G = \begin{bmatrix} \cos^2 \theta e^{i\Delta\phi} + \sin^2 \theta & \cos \theta \sin \theta (e^{i\Delta\phi} - 1) \\ \cos \theta \sin \theta (e^{i\Delta\phi} - 1) & \sin^2 \theta e^{i\Delta\phi} + \cos^2 \theta \end{bmatrix} \quad (7.21)$$

The phase difference is given by equations (7.12) and (7.14).

#### 2. Phase-matched polarisation converter

The transformation matrix for a phase-matched polarisation converter may be obtained from equation (7.21). If the applied vertical field is such that the difference between the effective indices of the TE and TM modes of the passive waveguide is eliminated, then  $\theta = 45^\circ$ . The transformation is then given by:

$$T_{PM} = \begin{bmatrix} \cos(\Delta\phi_{x'y'}) & i \sin(\Delta\phi_{x'y'}) \\ i \sin(\Delta\phi_{x'y'}) & \cos(\Delta\phi_{x'y'}) \end{bmatrix} \quad (7.22)$$

where equation (7.14) yields:

$$\Delta\phi_{x'y'} = - \frac{2\pi L r_{41} n_0^3 E_v}{\lambda_0} \quad (7.23)$$

### 7.2.4 TE-TM switching

An important mode of operation for the polarisation controller is TE/TM switching with a TE input state, with applications such as Polarisation Shift Keying in optical telecommunications. To obtain the TM output state, there is only one relevant solution for the applied fields, such that  $n_{\text{TM}}^{-2} - n_{\text{TE}}^{-2} + r_{41} E_x = 0$  so that  $\theta = \pm 45^\circ$ , and  $\Delta\phi = \pi$ . There is, however, more than one convenient way of obtaining the TE output state. Two examples are:

1. Maintaining the value of  $E_x$  while altering  $E_v$ .
2. Maintaining  $E_v$  while altering  $E_x$ .

In general, to obtain a TE output state from a TE input state for any angle  $\theta$  requires  $\Delta\phi = 2\pi m$ , where  $m$  is an integer. Recalling equation (7.16) yields:

$$\left( \left( \frac{1}{n_{\text{TM}}^2} - \frac{1}{n_{\text{TE}}^2} + r_{41} E_x \right)^2 + (2r_{41} E_v)^2 \right) = \left( \frac{-2\lambda_0 m}{Ln_{\text{eff}}^3} \right)^2 \quad (7.24)$$

The first method can involve the first two terms in equation (7.24) being set to zero, and therefore  $m = 0$ , so that the TE state is maintained throughout propagation. Alternatively,  $E_v$  can be doubled to produce coupling to TM and back to TE during propagation, and  $m = 1$ . In either case the voltage swing required to switch between the two output states alters the difference between the voltages applied to the two electrodes. Other values of  $m$  require larger voltage swings and are of less interest. The change in  $V_v$  is given by the maximum required magnitude of  $E_v$  as given in equation (7.20), which is required to give TM output from TE input, multiplied by  $d_v$ :

$$\Delta V_v = \pm \frac{\lambda_0 d_v}{2r_{41} Ln_{\text{eff}}^3} \quad (7.25)$$

In the second method  $E_v$  remains fixed to its maximum required magnitude. This is substituted into equation (7.24) to give the values of  $E_x$  which produce TE output, with  $m \neq 0$ :

$$\frac{1}{n_{\text{TM}}^2} - \frac{1}{n_{\text{TE}}^2} + r_{41} E_x = \left( \pm \sqrt{4m^2 - 1} \right) \left( \frac{\lambda_0}{Ln_{\text{eff}}^3} \right) \quad (7.26)$$

The required change in  $V_x$  is applied to both electrodes, and is given by:

$$\Delta V_x = \left( \pm \sqrt{4m^2 - 1} \right) \left( \frac{\lambda_0 d_x}{r_{41} Ln_{\text{eff}}^3} \right) \quad (7.27)$$

The smallest available integer value,  $m = \pm 1$ , gives the only important case, since larger values correspond to larger voltage swings. In this case, the switching voltages required in the two methods may be compared thus:



$$\frac{\Delta V_x}{\Delta V_v} = 2\sqrt{3} \frac{d_x}{d_v} \quad (7.28)$$

It is therefore concluded that if complete overlap between both components of the applied field and the optical field could be obtained then the first method described, involving the switching of  $V_v$ , would require a smaller voltage swing than the second method by a factor of 3.46.

## 7.3 Experiments

### 7.3.1 Low frequency arbitrary polarisation state synthesiser design

The design of the twin-electrode electrooptic polarisation controller is constrained by two main factors. Using the standard UV photolithographic process described in chapter three, the minimum electrode width that can be defined is 1.0  $\mu\text{m}$ , while the gap between the electrodes can be realised repeatably if greater than around 3.0  $\mu\text{m}$ . The minimum guide width is therefore 5.0  $\mu\text{m}$ . It may be possible to fabricate this device with smaller guide widths, but that would require the development of a new process. The second factor is the value of the phase-matching voltage  $V_{PM}$  at the design guide width, which is determined by the index difference of the passive waveguide, the electrooptic depth and the overlap of the vertical applied field component with the optical field. As discussed in section 7.2, it must be possible to match the TE and TM effective indices with a voltage that is smaller than the reverse bias breakdown voltage. A further issue is the need for single mode operation; however, if the electrooptic waveguide is too wide for this, a tapered passive section can be added to carry out the mode filtering function.

The timescales covered by this work did not permit the dedicated design and fabrication of a wafer optimised for this device. Wafer P0a was identified as the most suitable existing design, having the smallest measured value of  $V_{PM}$  of around 40 V for guide widths in the range 5 to 6  $\mu\text{m}$ . Devices were fabricated on a wafer with epitaxy design P0a with various combinations of electrode width and electrode pitch, on waveguides with nominal widths in the range 5 to 8  $\mu\text{m}$ . On waveguides narrower than 5.5  $\mu\text{m}$ , the electrode metallisation was used to self-align the waveguide. Propagation along the [011] direction was selected. The device length was 3 cm. An optical micrograph of a section of one device is shown in Fig. 7.5. The electrooptic waveguide is indicated, and its two electrodes are visible. In the example shown, each electrode is periodically connected to a wider feed line to ensure electrical connection to the entire length in the event of small breaks in the narrow electrodes. One such connection is visible. To the left is a large area ground pad.

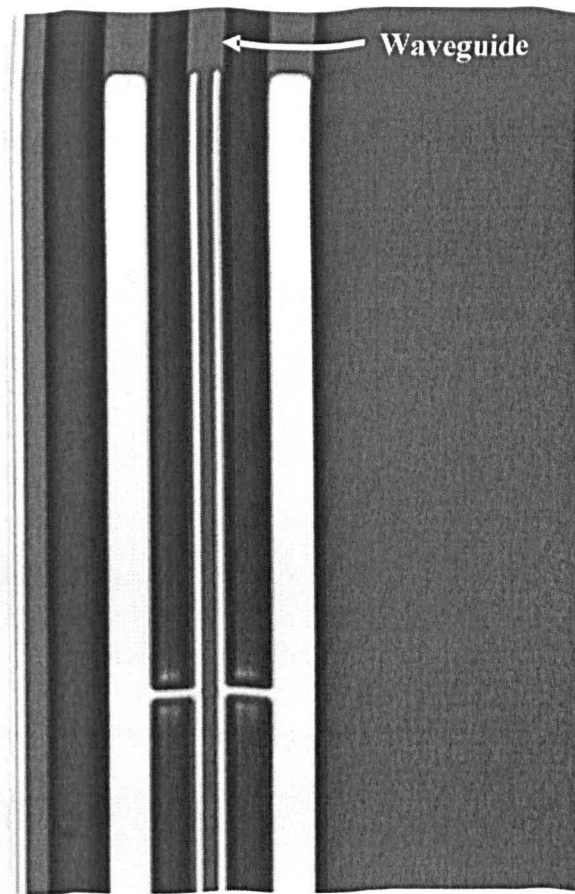


Fig. 7.5: Optical micrograph showing a section of a twin-electrode electrooptic waveguide arbitrary polarisation controller.

### 7.3.2 Experimental methods

Waveguide devices were characterised using the experimental setups and techniques given in the previous chapters, with the following modifications and details. Measurements were made to demonstrate the generation of linear output polarisations throughout the  $180^\circ$  range of angles in steps of  $15^\circ$ . This was carried out for input polarisations of  $0^\circ$  (TE),  $45^\circ$  and  $90^\circ$ . This selection of polarisation transformations was chosen partly for ease of measurement, but also because it requires the setting of mode angles throughout the full range, while also requiring the largest phase shift for each mode angle. The pairs of signal voltages required to obtain each output polarisation were recorded, and the extinction of each output state was measured. It was convenient to apply a low-frequency sawtooth signal to one electrode and an adjustable fixed voltage to the other. The transmission through the output polariser was observed as a time series triggered by the sawtooth voltage. The output polariser was set orthogonal to the required linear output state, which was obtained by adjustment of the variable d.c. voltage to optimise a null in the transmission. A null would be available provided that the sawtooth voltage range was set to include the required value. These measurements

were obtained using a device with an electrode width of 1.0  $\mu\text{m}$ , an electrode gap of 3.25  $\mu\text{m}$ , a guide width of 5.25  $\mu\text{m}$  and a length of 3 cm.

A single measurement was made to demonstrate phase-matched TE-TM switching. This mode of operation was achieved by the application of two sawtooth voltages in antiphase, such that the mean of their values remained constantly equal to the phase-matching voltage. The device used for this demonstration was almost identical to that described above, but with an electrode gap of 3.0  $\mu\text{m}$  and a guide width of 5.0  $\mu\text{m}$ .

7.4 Results and comparison with theory

7.4.1 Arbitrary polarisation control

The voltages required to generate linear output polarisation states throughout the 180° range of angles with 15° intervals, from three linear input states, are given in Table 7-I. The measured extinction value for each transformation is included. Only one of the possible combinations of voltages was measured for each state. The data were obtained using the device that had a guide width of 5.25  $\mu\text{m}$ .

Output state (deg)	0° input state			45° input state			90° input state		
	$V_1$	$V_2$	Extinction (dB)	$V_1$	$V_2$	Extinction (dB)	$V_1$	$V_2$	Extinction (dB)
0	38.5	49.4	20.2	37.3	55.2	17.6	42.9	46.2	16.1
15	39.9	52.6	19.5	40.0	45.6	15.5	43.1	46.9	16.1
30	38.8	54.3	17.3	39.9	46.4	14.7	43.2	48.0	15.4
45	38.0	55.1	14.8	49.7	45.1	15.4	43.0	49.2	15.7
60	41.2	43.9	15.0	45.7	46.8	17.4	42.4	50.5	17.1
75	42.4	44.3	15.4	44.2	48.3	17.3	42.2	51.9	18.6
90	43.5	45.2	15.5	43.4	49.4	16.4	38.6	51.0	18.8
105	43.6	46.9	15.0	42.8	51.0	15.2	38.7	52.9	17.9
120	43.7	48.0	14.6	42.1	52.5	14.5	38.2	53.5	16.7
135	43.7	49.3	15.2	40.4	53.1	14.7	37.3	54.5	16.0
150	43.2	50.6	16.7	40.1	54.3	14.9	41.2	44.6	14.9
165	42.5	51.8	18.6	38.3	54.7	16.2	43.2	45.8	16.2

Table 7-I: Signal voltages and measured extinction values for a selection of polarisation transformations.



The vertical and horizontal applied electric field components required to produce the selection of polarisation transformations obtained experimentally were calculated from equation (7.21). These are plotted in Figs. 7.6 to 7.8. The corresponding experimental data are plotted against a second vertical axis. The mean of  $V_1$  and  $V_2$ ,  $V_x$ , is plotted alongside theoretical  $E_x$ , giving good agreement.  $V_y$ , given by the difference  $V_1 - V_2$ , is plotted alongside theoretical  $E_y$ . This comparison also shows good agreement, with the exception that zero voltage difference does not coincide with zero theoretical  $E_y$ . There are a number of possible explanations for this, such as the presence of an asymmetry in the waveguide cross section, or an offset of both electrodes relative to the waveguide. The functionality of the device is not compromised. It is also noted that some  $V_x$  data points do not fit the theoretical curves. In all such cases the input polarisation state was the same as the output state. For the  $0^\circ$  and  $90^\circ$  input polarisations  $V_x$  is not required to take a specific value provided that  $E_y = 0$ , which was the case in practice, since  $V_y$  was equal to the offset mentioned above. For the  $45^\circ$  input polarisation, neither data point fits the theoretical curves displayed on the plots, but a calculation has shown that the measured voltages provide an alternative solution that does match the theory. It should be noted that the experimental measurements were made before the theoretical analysis was carried out. The voltages required to optimise a given polarisation state were measured, rather than the polarisation state being measured for pre-defined voltages. Only one set of voltages was recorded for each polarisation transformation, although it was apparent during the experiment that other combinations could be used.

The measured polarisation extinction values are shown in Fig. 7.9 versus output polarisation for the three input states. The extinction varied between 14.5 dB and 20 dB.

#### 7.4.2 TE-TM switching

Fig. 7.10 is an oscilloscope trace showing phase-matched TE-TM switching of the output polarisation, measured on the  $5.0\ \mu\text{m}$  device. The two linear ramp voltages with opposite gradients were applied to the two electrodes such that their mean,  $V_x$ , was constantly equal to the phase-matching voltage, which was 39 V for this device. The voltages are plotted at 10 V/division. The TE and TM output signal levels are shown, indicating the switch from TM output to TE output, which required an 8 V change in  $V_y$ . The expected sinusoidal variation of transmission through the output polariser as a function of  $V_y$  is apparent. At the TE peak, the TE/TM extinction ratio was 20 dB. At the TM peak the TM/TE extinction ratio was 13 dB.

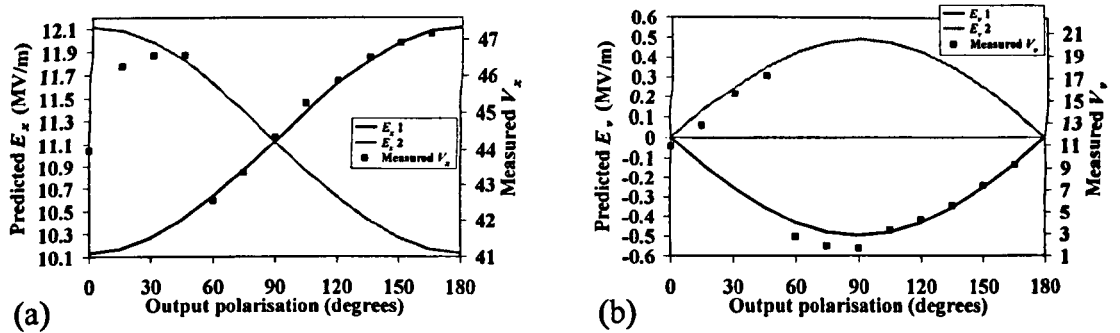


Fig. 7.6: Linear horizontal input polarisation.

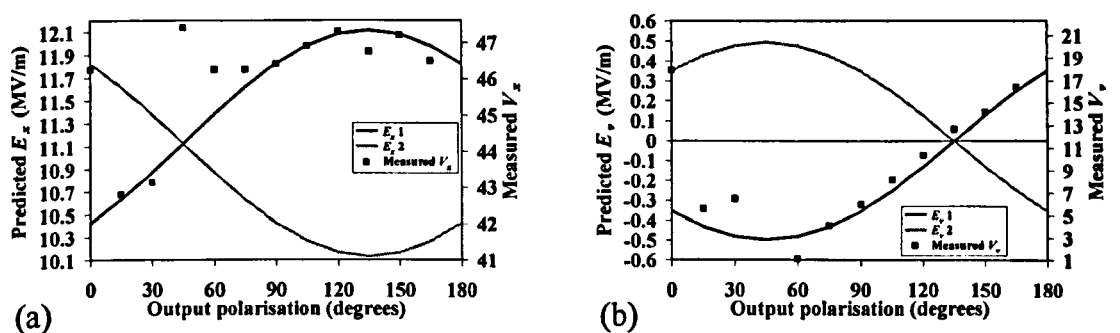


Fig. 7.7: Linear 45° input polarisation.

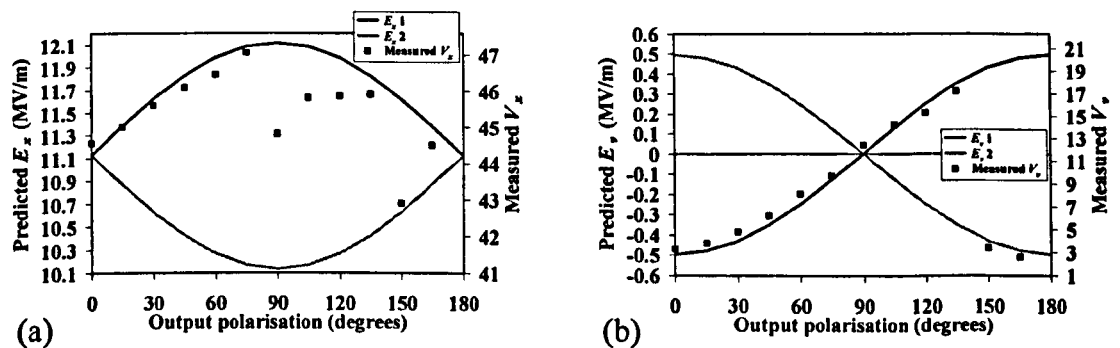


Fig. 7.8: Linear vertical input polarisation.

Figs. 7.6 to 7.8: Results for a polarisation controller device with a guide length of 3 cm, operating at a wavelength of 1550 nm. Comparison of experimental data with theoretical predictions for three input polarisations as indicated. (a) Theoretical vertical applied electric field component versus output polarisation, with experimental  $V_x$  plotted on the second vertical axis. (b) Theoretical horizontal applied electric field component versus output polarisation, with experimental  $V_y$  plotted on the second vertical axis.

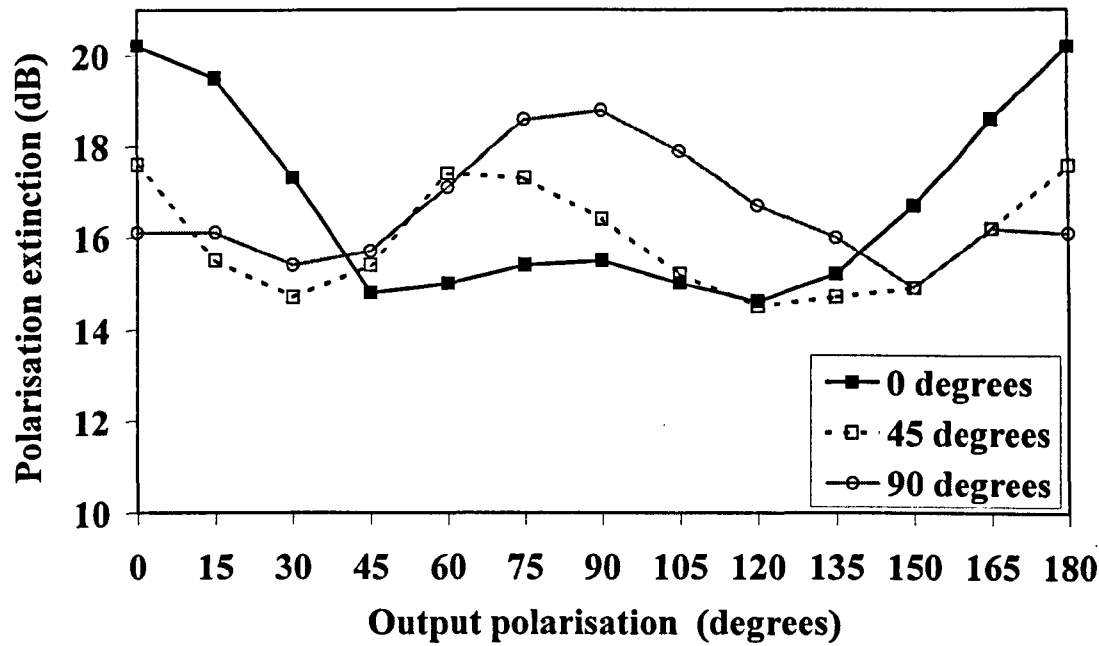


Fig. 7.9: Polarisation extinction versus linear output polarisation angle for three input states.

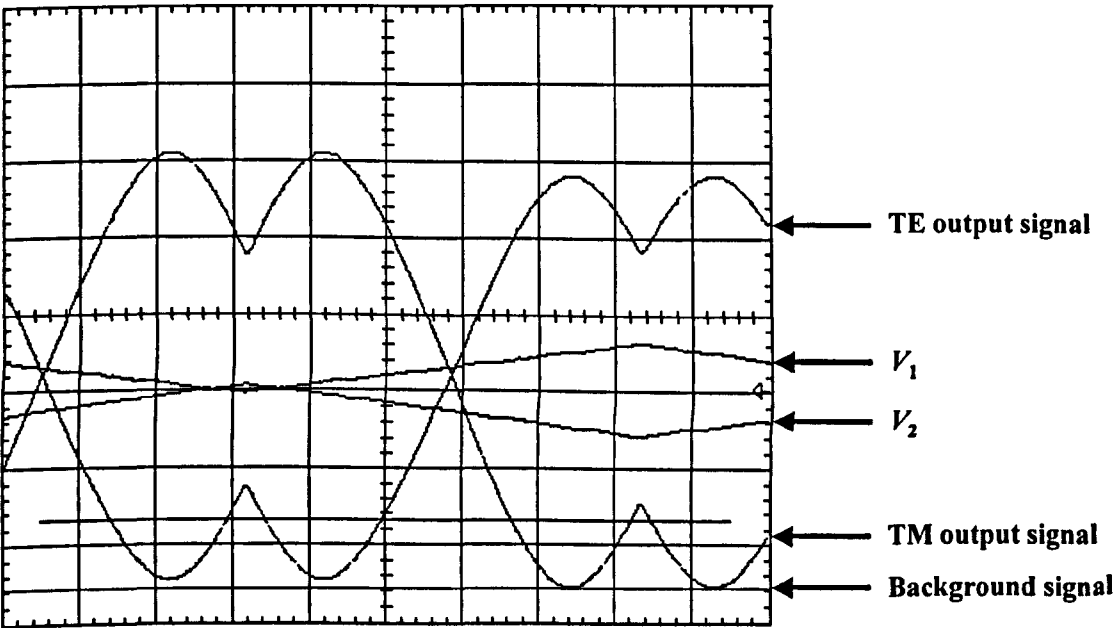


Fig. 7.10: Oscilloscope trace showing a demonstration of phase-matched TE-TM switching.

### 7.4.3 Field overlap and coupling constant calculations

The parameters  $d_x$  and  $d_v$  were defined in section 7.2, to express the overlap of the optical field and  $x$  and  $v$  components of the applied electric field respectively. Each represents an equivalent length relating the equivalent electric fields  $E_x$  and  $E_v$  that would be required to produce the measured electrooptic response from the applied voltages  $V_x$  and  $V_v$  respectively, given perfect field overlap. It was shown in section 7.2 that the device can be driven in such a way that TE-TM switching is performed by changing either  $V_x$  or  $V_v$  alone. Isolation of each field component in the operation of the device permits the parameters  $d_x$  and  $d_v$  to be measured.

In order to gauge the efficiency of the novel electrode arrangement, it is instructive to make the comparison with an alternative configuration published in the literature. The device presented by Grossard et al. [87], which operates at a wavelength of 1.3  $\mu\text{m}$ , is shown in Fig. 7.11a. It features a shallow-etched waveguide, the etched surface of which is positioned to be approximately co-planar with the centre of the optical mode. An electrode is placed on the etched surface either side of the waveguide, to permit the application of horizontal fields. Another electrode is placed on top of the waveguide to allow the independent application of vertical fields. This electrode arrangement precludes the use of an in-grown doped ground plane, so a semi-insulating structure is used, while the lateral ground electrode also provides the ground for the upper electrode. In principle, the Grossard device offers similar functionality to the device presented in this work, but uses a fundamentally different electrode structure. The horizontal and vertical applied field components produced by the two different electrode configurations are shown schematically for comparison in Figs. 7.11a and 7.11b.

If complete overlap between the applied field and the optical field could be obtained, then TE-TM switching performed by switching  $V_v$  would result in a smaller switching voltage by a factor of 3.46. However, for the field overlap values measured in the 5.25  $\mu\text{m}$  guide width experimental example, the values are 8.83 V for  $\Delta V_v$  and 6.87 V for  $\Delta V_x$ , giving a ratio  $\Delta V_x/\Delta V_v = 0.78$ . This indicates that the horizontal field overlap is inferior to the vertical field overlap by a factor of more than four.

Calculation of  $d_x$  and  $d_v$  requires knowledge of the effective index and the linear electrooptic coefficient. However, the values of these parameters are not known accurately, as discussed earlier. The parameters are therefore presented in Table 7-II with the divisor  $n_{\text{eff}}^3 r_{41}$ . For indication, values of  $d_x$  and  $d_v$  are calculated using the values  $r_{41} = -1.36 \times 10^{-12} \text{ mV}^{-1}$  and  $n_{\text{eff}} = 3.4$ . Equivalent parameters for the Grossard device are included for comparison.

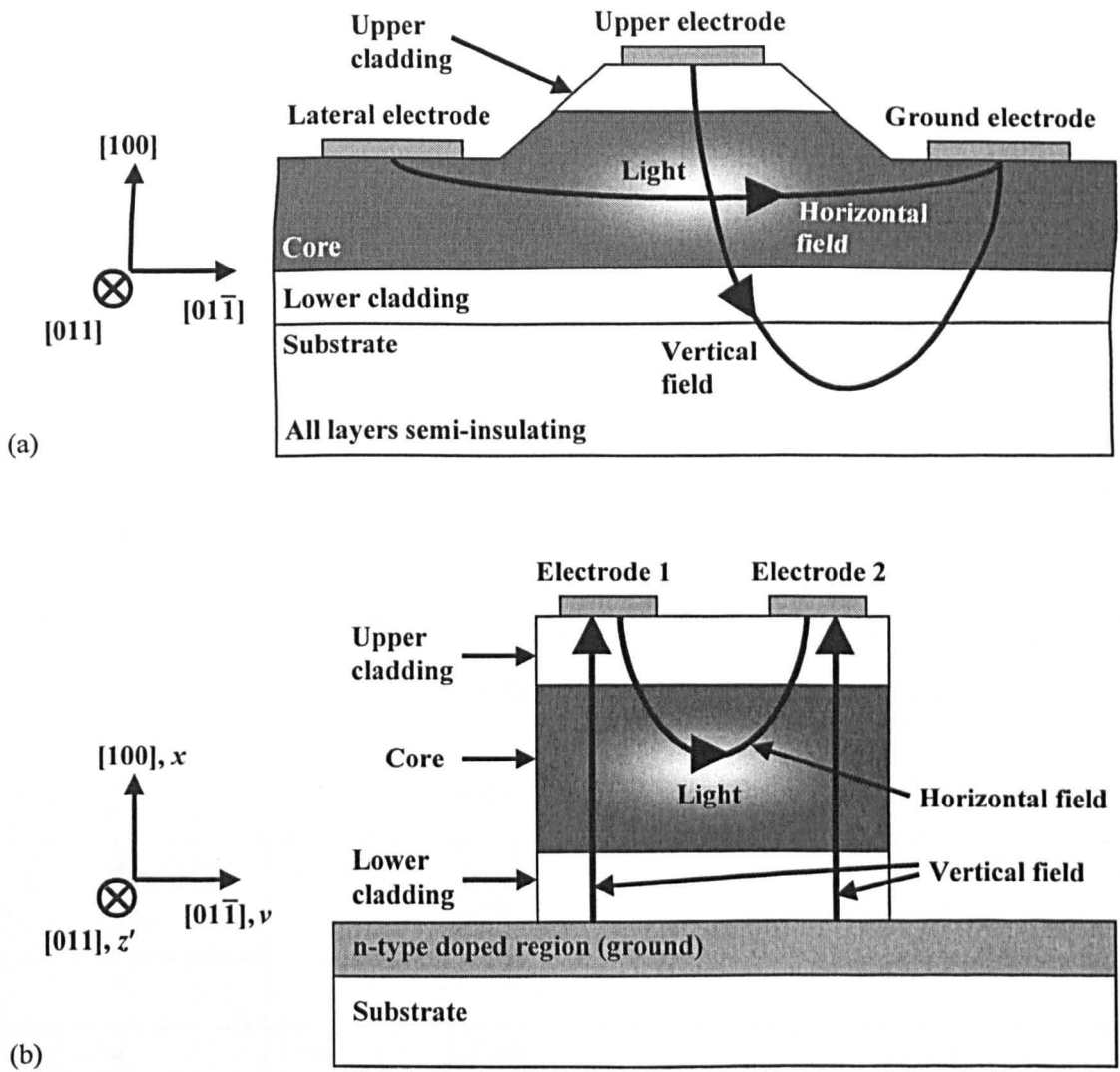


Fig. 7.11: Schematic diagrams of the cross sections of two types of electrooptic polarisation controller device, with horizontal and vertical applied field components indicated. (a) The device reported by Grossard et al. [87], (b) the novel twin-electrode device.

Under conditions of phase matching, the coupling constant is given by:

$$\kappa = \frac{\pi}{2z_c} \quad (7.29)$$

where  $z_c$  is the propagation length over which complete coupling from TE to TM occurs. The parameter values for the demonstrated polarisation converter return a value of  $\kappa = 52.3 \text{ m}^{-1}$ , for an offset-corrected voltage difference value  $V_v = 8.83 \text{ V}$ . The specific value of the coupling constant is therefore  $\kappa/V_v = 5.9 \text{ m}^{-1}\text{V}^{-1}$ .

The parameter summary given in Table 7-II shows that the novel twin-electrode arrangement gives a horizontal field overlap that is comparable with that of the Grossard device: indeed it is slightly superior. The specific coupling constant of the Grossard device is slightly larger due to the shorter wavelength of operation used. However, the twin-electrode

device displays a far superior vertical field overlap, nearly three times better than that of the Grossard device. This superiority is due to the use of an in-grown doped ground plane, which permits a near-perfect overlap, and cannot be used in the Grossard arrangement. It is clear that there is potential in both designs for iterative improvements to be made.

For use as a discrete component for TE-TM switching, there is little to choose between the two devices in terms of performance. Their fabrication also requires a similar level of complexity. However, the novel device presented in this work has a clear advantage when used as an arbitrary polarisation controller because of its superior vertical field overlap. This feature also makes it more suitable for integration with other electrooptic waveguide components which require only a vertical field, such as Mach-Zehnder interferometer intensity modulators and phase modulators.

Parameter	Twin-electrode device, 5.25 μm guide width	Grossard et al. [87]
$\frac{d_v}{n_{\text{eff}}^3 r_{41}}$	$3.4 \times 10^5 \text{ V}$	$4.0 \times 10^5 \text{ V}$
$\frac{d_x}{n_{\text{eff}}^3 r_{41}}$	$7.7 \times 10^4 \text{ V}$	$2.2 \times 10^5 \text{ V}$
$d_v$	18.3 μm	21.3 μm
$d_x$	4.1 μm	11.7 μm
$\frac{\kappa}{V_v}$	$5.9 \text{ m}^{-1} \text{ V}^{-1}$	$6.1 \text{ m}^{-1} \text{ V}^{-1}$

Table 7-II: Comparison of field overlap parameters for the twin-electrode device with an alternative presented in the literature.

## 7.5 Device variants

### 7.5.1 Travelling-wave device

The frequency response of the device described above is limited by the length of its electrodes, which are not designed to carry microwave signals and are therefore referred to as “lumped”. The radio frequency (RF) limit for such a structure corresponds with an RF wavelength approximately one order of magnitude longer than the electrodes. For a practical waveguide device with an electrode length of typically one centimetre or greater, this corresponds to switching at frequencies of up to around 1 GHz. For switching frequencies faster than this the electrical aspects of the device must be designed for RF operation. The twin-electrode structure is compatible with travelling wave electrode structures, which have been demonstrated in waveguide devices including Mach-Zehnder interferometer intensity modulators, phase modulators, and polarisation modulators [17]-[18], [30]-[31] [88], [131], [153]. In these structures, the electrodes on the waveguides are incorporated into an RF transmission line which is designed such that the RF velocity is matched to the optical velocity, so that the optical group is subject to the same refractive index distribution throughout its transit along the waveguide. Additionally the transmission line is designed with a characteristic impedance which matches that of the RF signal source and termination. This is often 50  $\Omega$ . A travelling wave structure would offer the potential to extend the bandwidth of the device to 40 GHz or more, thus making it compatible with 10 Gbit/s and 40 Gbit/s optical communications applications.

### 7.5.2 Multiple stage devices

A number of multiple-stage device configurations including the twin-electrode device are envisaged. These have the purpose of permitting the twin-electrode device to be operated in a restricted mode, requiring the application of only one time-varying voltage signal. Such operation may be convenient in certain circumstances, including operation of a travelling-wave configuration at RF switching speeds. Many potential applications of the device do not require full arbitrary polarisation control functionality, for example fast TE-TM polarisation conversion has applications in optical telecommunications, and this would only require the application of one RF signal. Other applications would use a fixed input polarisation, for example, from a laser mounted immediately before the device input. Various configurations are discussed below.

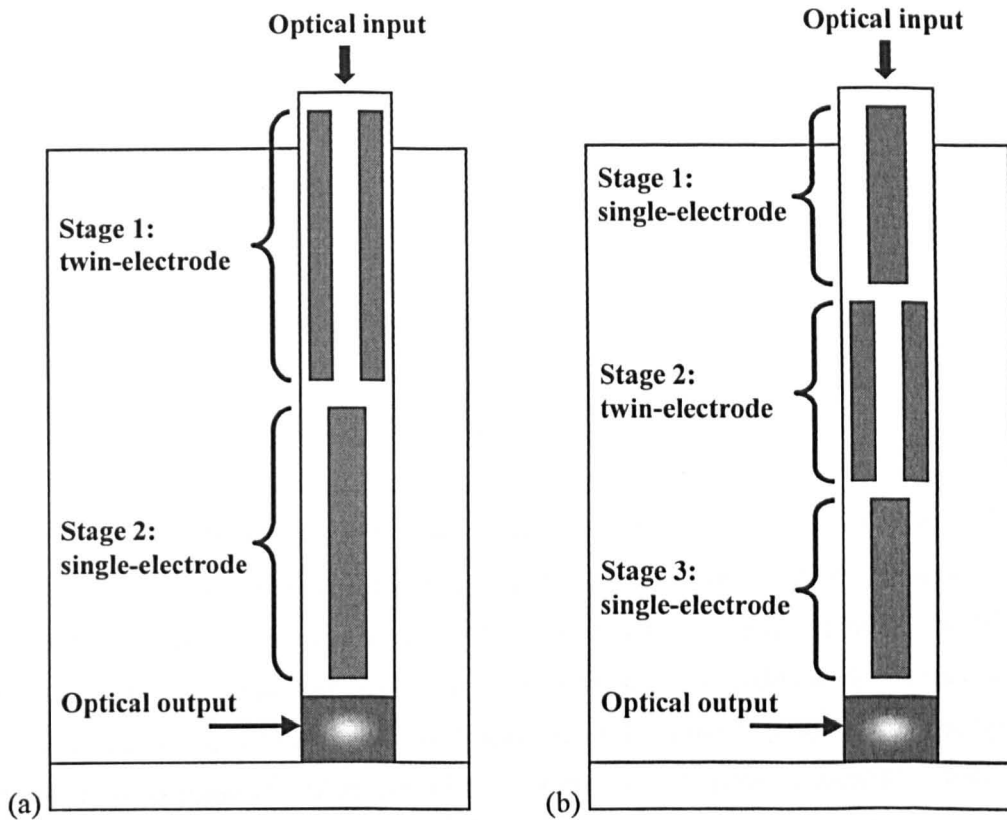


Fig. 7.12: Schematic diagrams of multiple-stage electrooptic waveguide polarisation controllers containing the twin-electrode device. (a) Two-stage device, (b) three-stage device.

### 1. Two-stage device

This device would consist of a twin-electrode stage followed by a single-electrode stage, as shown in Fig. 7.12a. It is capable of providing any output polarisation state from a fixed input state. For the example of a horizontal linear input polarisation, the twin-electrode stage would be operated with  $E_x$  fixed to provide TE-TM phase matching, while  $E_y$  would be varied to rotate the azimuth of the polarisation state to any angle. This operation could be carried out at RF switching speeds. The single-electrode stage would then be used to alter the phase of the horizontal component relative to the vertical component, which could also be carried out at RF switching speeds. This example is of relevance to applications where the device is to be used immediately after a laser source.

### 2. Three-stage device

If the input state is not fixed, and the twin-electrode stage is to be operated in restricted mode, then an additional single-electrode stage is required before the twin-electrode stage for all output states to be available. This three-stage configuration is shown in Fig. 7.12b. The first single-electrode stage would be required to shift the TE phase to  $\pm\pi/2$  relative to the TM



component. The second and third stages of the device would then operate as for the two-stage device. The polarisation functions involved and the reasons why they are required in this three-stage device are detailed in reference [84], for an implementation of the functions in an alternative technology.

The functionality of the two and three stage devices is confirmed by multiplication of the relevant transformation matrices for individual functions, which yields the transformation matrix for universal polarisation control given in equation (7.21).

### 7.5.3 Integration of additional functions

The twin-electrode device may be integrated monolithically with other electrooptic devices that require a TE polarisation and that may be fabricated using the same standard process. These include phase modulators and Mach-Zehnder interferometer intensity modulators, which may be implemented with travelling-wave or lumped electrode configurations. In each case the polarisation controller would be placed last in the train. *The integration of multiple functions such as these offers possibilities for reduced-cost devices.* Examples include an integrated high-speed polarisation modulator plus a variable optical attenuator. A device comprising a high-speed phase modulator plus a polarisation modulator could be used to combine the telecommunications formats of Phase Shift Keying (PSK) and Polarisation Shift Keying (PolSK). A system using discrete components to combine these functions has been proposed [83] for simultaneous transmission of the data payload and label.

Excessive chip length need not present a concern for the concept of multiple-stage devices because the deep-etched structure is compatible with small-radius bends, allowing the implementation of folded structures. In waveguides of the kind described, bends with radii smaller than 200  $\mu\text{m}$  have been demonstrated with almost negligible excess loss and good fundamental mode preservation. This radius is small in the context of the overall dimensions of the device that has been demonstrated.

Integration of the functions described is not possible with the conventional single-electrode polarisation modulator [5]-[7] on its own, because it is not compatible with a horizontal polarisation state. These devices require an input polarisation state that contains equal horizontal and vertical components. The linear electrooptic effect is used to modulate the phase of the horizontal component, resulting in output polarisation states that are limited to  $+45^\circ$ ,  $-45^\circ$ , right hand circular, left hand circular, and the intermediate elliptical states. Linear horizontal or vertical output states cannot be obtained.

Further possibilities for the monolithic integration of functions may be identified if the constraint of the use of the standard process described is removed. In particular, the

integration of a laser would enable simpler packaging of compact transmitters. Alternatively, the integration of semiconductor optical amplifier (SOA) stages would permit the use of the device in very complex optical circuits, in which some allowance must be made for a large optical loss or a large splitting ratio of the optical source. In order to fabricate these components with the polarisation controller on a single substrate, a selective area re-growth process would normally be required, because of the two different material composition requirements [154]. For operation at the important telecommunications wavelength of 1550 nm, there are two options for the gain medium: the development of suitable “dilute nitride” GaInNAs material for integration on a GaAs substrate [155], and the re-design of the polarisation controller for realisation in indium phosphide, for compatibility with mature InGaAsP laser technology. Although dilute nitride lasers have been developed for operation at telecommunications wavelengths [156], [157], and the integration of GaInNAs semiconductor optical amplifiers with GaAs waveguides has been demonstrated [158], this technology remains relatively immature. Alternatively, InP offers a substitute material to GaAs for fabrication of the polarisation controller, with similar fabrication considerations and optical parameters. The linear electrooptic coefficient [138] and refractive index values [159] for InGaAsP alloys are comparable with those of AlGaAs. Transfer to this material would require modelling and evaluation of test structures and device designs to achieve single-mode operation with suitable drive voltages. Some degradation in the optical loss due to absorption and an increase in photocurrent generation would be expected due to the close proximity of the absorption edge.

## 7.6 Conclusions

A novel electrode arrangement has been proposed for an electrooptic waveguide polarisation controller, in which a pair of electrodes are positioned on top of the waveguide, out of the plane of the optical mode, and with a doped ground plane beneath the waveguide. Theoretical analysis has identified that the device is capable of arbitrary polarisation transformations by independent control of horizontal and vertical applied electric field components. A set of design requirements has been defined. Two similar designs have been specified, fabricated and successfully demonstrated with an operating wavelength of 1550 nm. The generation of linear output polarisations covering all azimuth angles has been performed for three different linear input polarisations, with an output polarisation extinction of between 14 dB and 21 dB. The data were compared with theoretical predictions of the switching voltages, which were prepared using some measured parameters. A good agreement was shown, confirming the validity of the assumptions that the mean of the voltages applied to the two electrodes

provides the vertical field component, and the difference between the voltages provides the horizontal field component. Phase-matched TE-TM switching has been demonstrated, requiring a fixed phase-matching voltage of 39 V and a switching voltage of 8 V. The twin-electrode arrangement was shown to withstand differential voltages several times larger than the switching voltage. Several multiple-stage device configurations were proposed, to enable the use of a simplified voltage drive for the twin-electrode stage.

The twin-electrode design has been compared with alternative configurations. The following advantages and key features were identified:

1. The device may be fabricated using a standard process without any additional stages.
2. The fringing field from two electrodes on top of the waveguide was found to give an overlap of the horizontal component with the optical field that was comparable with that of an alternative configuration published in the literature in which two electrodes were positioned coplanar with the optical mode. The vertical field overlap was shown to be substantially superior to that of the alternative because of the use of an in-grown doped ground plane.
3. The device may be integrated with other waveguide structures including devices that require a horizontal polarisation state, such as Mach-Zehnder interferometer intensity modulators or phase modulators. The deep-etched waveguide structure is compatible with small-radius bends, enabling the folding of long integrated devices.
4. The device is compatible with a travelling-wave electrode configuration for fast switching.
5. The device is not subject to prohibitive fabrication tolerances, due to the level of electrooptic control offered by its electrode arrangement.
6. One device design may be used over a range of wavelengths, for example in Dense Wavelength Division Multiplexing (DWDM).
7. The device was designed and demonstrated with an operating wavelength of 1.55  $\mu\text{m}$ .
8. Alternative designs may be obtained for other wavelengths of operation, including 0.8-12  $\mu\text{m}$  in the GaAs/AlGaAs material system.
9. The device may be realised in other materials systems, including indium phosphide.

## Chapter 8: Summary and Conclusions

The research described in this thesis was motivated by the need to address problems and exploit opportunities arising from observations of polarisation conversion effects in gallium arsenide optical waveguide devices. The first priority of the work was to obtain an understanding of the causes of unwanted polarisation conversion, which degrades the performance of waveguide devices such as electrooptic intensity modulators. The required outcome of this part of the work was the ability to predict and prevent unwanted effects. A second aspect of the research sought to apply the electrooptic polarisation conversion effects observed to create a device that provides a new function in integrated optics: a fully integrable electrooptic polarisation controller.

The approach taken to the work placed an emphasis on making experimental demonstrations of theoretical concepts and principles. Where possible, the observed behaviour was described using existing readily-available simulation techniques. Simple theoretical models were sought that would provide the device designer with the means to understand and incorporate the lessons learned with speed and convenience.

Unwanted changes in the polarisation state of light propagating in passive deep-etched waveguides were investigated. Experimental results were presented to demonstrate an effect that was attributed to asymmetry in the waveguide cross-section geometry resulting from non-vertical etching. Strong polarisation conversion was observed at a critical guide width, termed the “phase-matching” width, corresponding to the closest approach of the effective indices of the polarised modes. A simplified account of the behaviour was provided using a coupled-mode formulation. The validity of this approach for use in the prediction of the effect was confirmed. Quantitative agreement was shown between the measured data and simulations of polarisation coupling strength made using established techniques. The experimental examples presented provide quantitative benchmarks. For example, results indicated that light propagating in a typical waveguide with a parallel side-wall slant angle of  $5^\circ$  and a critical width of  $3.63\text{ }\mu\text{m}$  will undergo complete polarisation conversion from TE to TM in a length of 17 mm.

Details of the nature of the optical modes predicted by rigorous numerical simulations were reproduced accurately by the experimental results. Specifically, the polarisation angles of hybrid waveguide modes were measured, and a novel technique was presented for the measurement of the difference between the effective indices of orthogonally polarised modes. The measurements obtained were used to form the basis for an analysis of the evolution of elliptical polarisation states during propagation, and to verify the account of the physical origin of the polarisation conversion provided by the theory.

The study of polarisation conversion was extended to include effects that occur in electrooptic waveguides. The influence of the linear electrooptic effect (*Pockels effect*) on polarisation conversion by modification of the modal index relationship was investigated. It was demonstrated experimentally that for a simple epitaxy design, designated P0, alteration of the TE effective index relative to the TM index by the application of a vertical electric field could cause phase-matched polarisation conversion in waveguides with a range of widths. The propagation directions relative to the GaAs crystal required to cause or prevent electrooptic phase matching for a given guide width were identified. The effective strength of the linear electrooptic effect was measured for the specific wafer design P0, and the value was used with measurements of the passive guide index difference to predict the phase-matching voltage as a function of guide width. Good agreement with directly measured data was shown. The suitability of the coupled-mode theory for the prediction of the behaviour of electrooptic guides with a known index relationship was demonstrated.

An electrooptic coupling mechanism was identified whereby an offset of the electrode with respect to the waveguide results in a nett horizontal component in the applied electric field. Consequently, birefringence is induced that alters the principal polarisation angles of the waveguide modes. Experimental results were obtained to quantify the coupling constant due to this mechanism as a function of electrode offset, for one example of wafer design and guide width. For wafer design P0a, with a guide width of  $5.2\ \mu\text{m}$  and a phase-matching voltage of  $\sim 35\ \text{V}$ , the strength of the polarisation coupling mechanism resulting from an electrode offset of  $0.5\ \mu\text{m}$  was shown to be comparable with that resulting from a parallel side-wall slant of  $5^\circ$ .

These investigations of unwanted polarisation conversion provide important information for use in the design and fabrication of waveguide devices. The need to predict and avoid the phase-matching guide width is emphasised, while the consequences of process-dependent asymmetry in the waveguide cross section and a lateral offset of the electrode are shown. For electrooptic waveguides, the propagation direction should be chosen so that the application of a voltage causes the index difference to increase rather than decrease. The wafer should be designed with a large index difference for the range of guide widths intended for use. In pursuit of this goal, a technique for waveguide design was demonstrated that prevented unintended polarisation conversion in the presence of the identified coupling mechanisms, while maintaining the main waveguide parameters of material composition, optical mode size and shape, electrooptic performance and fabrication process. The principle of placing additional AlGaAs layer boundaries in the waveguide core was used in two test wafer designs to move the phase-matching guide width out of the useful range. In passive waveguides exhibiting slanted side walls and a strong coupling mechanism, preservation of the TE input

polarisation was demonstrated in guides with a large phase mismatch. The immunity of the designs to electrooptically phase-matched polarisation conversion was investigated. An important result was obtained from the less-radical of the two test designs, wafer P2. For an electrooptic waveguide of width  $3.6\text{ }\mu\text{m}$  and length 2 cm, the input TE polarisation was preserved to greater than 23 dB for voltages smaller than 50 V, despite phase-matched conversion at 69 V. At least 30 V was required to cause phase-matched polarisation conversion for any guide width in the specified useful range of 3-5  $\mu\text{m}$ , which could only occur for [011] propagation, while guides wider than 4  $\mu\text{m}$  were not susceptible at all. These results showed how the problem of unwanted polarisation conversion could be prevented by careful design of the wafer epitaxy without additional process development, and without compromising the main device parameters.

The understanding of the influence of the electrooptic effect gained in the study of unwanted polarisation conversion was applied to the design of a waveguide device for electrooptic control and switching of the polarisation state. A novel electrode arrangement was proposed, in which a pair of electrodes is positioned on top of the waveguide with a doped ground plane beneath the waveguide, enabling the independent application of electric field components directed horizontally and vertically through the waveguide cross section. A theoretical analysis was presented, which showed the device to be capable of converting any input polarisation state into an arbitrary output state using the linear electrooptic effect. A working design was obtained, operating at the optical telecommunications wavelength of 1550 nm. The fabrication of devices has been described and experimental results have been presented that demonstrate the generation of linear output polarisations covering all azimuth angles, for three different linear input polarisations, with an output polarisation extinction of between 14.5 dB and 20 dB. The design was compared to alternatives presented in the literature and several advantages were identified, including ease of fabrication using a standard process and the potential for integration with other waveguide components. Aspects of the performance of the device were found to compare favourably with the alternatives.

Many of the principles identified in the investigation of unwanted polarisation conversion are generic and are therefore applicable to other kinds of optical waveguides, such as photonic wires. However, the experimental benchmarks obtained are specific to the type of waveguide investigated. Similar measurements and simulations would be required to provide the designer of other kinds of waveguides with equivalent information.

The priority for further work related to the studies presented in this thesis is the development of the electrooptic polarisation controller, for which a number of possible further developments and variants were proposed in chapter seven. Although the device has broad applicability, the application in optical data transmission is identified in particular as having

the strong potential to adopt the technology. Consequently, it is recommended that the development of a travelling-wave version of the device is undertaken, with the potential for switching speeds at frequencies of tens of GHz, for use in Polarisation Shift Keying. This work should include the development of the device package, including optical and RF interfaces. Additionally, a demonstration should be pursued of an integrated device including the polarisation controller and another component, such as a Mach-Zehnder interferometer intensity modulator. Through these proposed developments, there is the potential for commercial deployment of this integrated optical technology.

## References

- [1] E. D. Finlayson, J. M. Heaton, B. M. A. Rahman and S. S. A. Obayya, "Polarization Conversion in Passive Deep-Etched GaAs/AlGaAs Waveguides," *J. Lightwave Technol.*, vol. 24, no. 3, pp. 1425-1432, 2006.
- [2] "Electro-optic Polarisation Controller", United Kingdom Patent Application, No. 0617899.0, September 2006 (awaiting publication).
- [3] A. Yariv and R. C. C. Leite, "Dielectric-Waveguide Mode of Light Propagation in p-n Junctions," *Appl. Phys. Lett.*, vol. 2, pp. 55-57, 1963 (erratum: vol. 2, p. 161).
- [4] W. L. Bond, B. G. Cohen, R. C. C. Leite, and A. Yariv, "Observation of the Dielectric-Waveguide Mode of Light Propagation in p-n Junctions," *Appl. Phys. Lett.*, vol. 2, pp. 57-59, 1963.
- [5] D. F. Nelson and F. K. Reinhart, "Light Modulation by the Electro-Optic Effect in Reverse-Biased GaP p-n Junctions," *Appl. Phys. Lett.*, vol. 5, pp. 148-150, 1964.
- [6] F. K. Reinhart, D. F. Nelson, and J. McKenna, "Electro-optic and Waveguide Properties of Reverse-Biased Gallium Phosphide p-n Junctions," *Appl. Phys. Lett.*, vol. 177, pp. 1208-1221, 1968.
- [7] D. Hall, A. Yariv, and E. Garmire, "Optical Guiding and Electro-Optic Modulation in GaAs Epitaxial Layers," *Opt. Commun.*, vol. 1, pp. 403-405, 1970.
- [8] J. P. van der Ziel, "Phase-Matched Harmonic Generation in a Laminar Structure with Wave Propagation in the Plane of the Layers," *Appl. Phys. Lett.*, vol. 26, pp. 60-61, 1975.
- [9] V. Evtuhov and A. Yariv, "GaAs and GaAlAs Devices for Integrated Optics," *IEEE Trans. Microwave Theory & Techniques.*, vol. MTT-23, pp. 44-57, 1975.
- [10] I. P. Kaminow, "Optical Waveguide Modulators," *IEEE Trans. Microwave Theory & Techniques.*, vol. MTT-23, pp. 57-70, 1975.
- [11] A. Yariv, C. A. Mead, and J. V. Parker, "GaAs as an Electrooptic Modulator at 10.6 Microns," *IEEE J. Quant. Electron.*, vol. QE-2, pp. 243-245, 1966.
- [12] W. L. Walters, "Electro-Optic Effect in Reverse-Biased GaAs p-n Junctions," *J. Appl. Phys.*, vol. 37, p. 916, 1966.
- [13] P. Buchmann, H. Kaufmann, H. Melchior, and G. Guekos, "Broadband Y-Branch Electro-Optic GaAs Waveguide Interferometer for 1.3  $\mu\text{m}$ ," *Appl. Phys. Lett.*, vol. 46, pp. 462-464, 1985.
- [14] J. P. Donnelly, N. L. DeMeo, G. A. Ferrante, K. B. Nichols, and F. J. O'Donnell, "Optical Guided-Wave Gallium Arsenide Monolithic Interferometer," *Appl. Phys. Lett.*, vol. 45, pp. 360-362, 1984.



- [15] F. J. Leonberger and C. O. Bozler, "GaAs Directional-Coupler Switch With Stepped  $\Delta\beta$  Reversal," *Appl. Phys. Lett.*, vol. 31, pp. 223-226, 1977.
- [16] R. C. Alferness, "Waveguide Electrooptic Modulators," *IEEE Trans. Microwave Theory & Techniques*, vol. MTT-30, pp. 1121-1137, 1982 (erratum: vol. MTT-31, p. 315, 1983).
- [17] S. Y. Wang and S. H. Lin, "High Speed III-V Electrooptic Waveguide Modulators at  $\lambda = 1.3 \mu\text{m}$ ," *J. Lightwave Technol.*, vol. 6, pp. 758-771, 1988.
- [18] R. G. Walker, "High Speed III-V Semiconductor Intensity Modulators," *IEEE J. Quant. Electron.*, vol. 27, pp. 654-667, 1991.
- [19] A. Alping and L. A. Coldren, "Electrorefraction in GaAs and InGaAsP and Its Application to Phase Modulators," *J. Appl. Phys.*, vol. 61, pp. 2430-2433, 1987.
- [20] J. E. Zucker, T. L. Hendrickson, and C. A. Burrus, "Low-Voltage Phase Modulation in GaAs/AlGaAs Quantum Well Optical Waveguides," *Electron. Lett.*, vol. 24, pp. 112-113, 1988.
- [21] L. Tsang and S. L. Chuang, "Coupled GaAs Multiple-Quantum Well Channel Waveguides Including Quadratic Electrooptic Effect," *IEEE J. Lightwave Technol.*, vol. 6, pp. 832-836, 1988.
- [22] A. Jennings, C. D. W. Wilkinson and J. S. Roberts, "Spectral Characterization of the Linear and Quadratic Electro-Optic Effects in GaAs/AlGaAs Multiple Quantum Well Waveguides," *Semicond. Sci. Technol.*, vol. 7, pp. 60-65, 1992.
- [23] M. Glick, F. K. Reinhart, and D. Martin, "Linear Electro-Optic Effect: Comparison of GaAs/AlGaAs Multi-Quantum-Well Heterostructures with an AlGaAs Solid Solution at  $1.1523 \mu\text{m}$ ," *J. Appl. Phys.*, vol. 63, pp. 5877-5879, 1988.
- [24] G. Bastard and J. A. Brum, "Electronic States in Semiconductor Heterostructures," *IEEE J. Quant. Electron.*, vol. QE-22, pp. 1625-1644, 1986.
- [25] D. R. Wight, J. M. Heaton, B. T. Hughes, J. C. H. Birbeck, K. P. Hilton, and D. J. Taylor, "Novel Phased Array Optical Scanning Device Implemented Using GaAs/AlGaAs Technology," *Appl. Phys. Lett.*, vol. 59, pp. 899-901, 1991.
- [26] J. M. Heaton, D. R. Wight, J. T. Parker, B. T. Hughes, J. C. H. Birbeck, and K. P. Hilton, "A Phased Array Optical Scanning (PHAROS) Device Used as a 1-to-9 Way Switch," *IEEE J. Quant. Electron.*, vol. 28, pp. 678-685, 1992.
- [27] R. M. Jenkins, J. M. Heaton, D. R. Wight, J. T. Parker, B. T. Hughes, J. C. H. Birbeck, G. W. Smith, and K. P. Hilton, "Novel  $1 \times N$  and  $N \times N$  Integrated Optical Switches Using Self-Imaging Multimode GaAs/AlGaAs Waveguides," *Appl. Phys. Lett.*, vol. 64, pp. 684-686, 1994.

- [28] J. M. Heaton, C. D. Watson, S. B. Jones, M. M. Bourke, C. M. Boyne, G. W. Smith, and D. R. Wight, "Sixteen Channel (1 to 16 GHz) Microwave Spectrum Analyser Device Based on a Phased-Array of GaAs/AlGaAs Electro-Optic Waveguide Delay Lines," *SPIE Optoelectronics and High-Power Lasers & Applications*, 1998.
- [29] "Apparatus for Generating Electrical Signals with Ultra-Wide Band Arbitrary Wave-Forms", International Patent, No. WO 02/054204 A2, 2002.
- [30] R. G. Walker and C. Edge, "A Folded-Path GaAs Travelling-Wave Modulator for Phased-Array Receivers," *Proc. Microwave Photonics*, pp. 113-116, 2000.
- [31] J. M. Heaton, S. B. Jones, M. M. Bourke, K. P. Hilton, J. C. H. Birbeck and D. R. Wight, "MMIC Compatible GaAs/AlGaAs Electro-Optic Waveguide Modulators and Switches for Microwave Applications," *Int. J. Optoelectron.*, vol. 10, pp. 479-488, 1995.
- [32] J. M. Heaton, M. M. Bourke, S. B. Jones, K. P. Hilton, and D. R. Wight, "Low-Loss GaAs/AlGaAs Waveguide Corners for Compact Optical Delay Lines," *Proc. IPR*, pp. 510-513, 1996.
- [33] R. L. Espinola, R. U. Ahmad, M. J. Steel and R. M. Osgood Jr., "A Study of High-Index-Contrast 90° Waveguide Bend Structures," *Opt. Express*, vol. 8, pp. 517-528, 2001.
- [34] V. Van, P. P. Absil, J. V. Hryniewicz, and P.-T. Ho, "Propagation Loss in Single-Mode GaAs-AlGaAs Microring Resonators: Measurement and Models," *IEEE J. Lightwave Technol.*, vol. 19, pp. 1734-1739, 2001.
- [35] L. B. Soldano and E. C. M. Pennings, "Optical Multimode Interference Devices Based on Self-Imaging: Principles and Applications," *IEEE J. Lightwave Technol.*, vol. 13, pp. 615-627, 1995.
- [36] J. M. Heaton and R. M. Jenkins, "General Matrix Theory of Self-Imaging in Multimode Interference (MMI) Couplers," *IEEE Photon. Technol. Lett.*, vol. 11, pp. 212-214, 1999.
- [37] H. Benisty, C. Weisbuch, D. Labilloy, M. Rattier, C. J. M. Smith, T. F. Krauss, R. M. De La Rue, R. Houdré, U. Oesterle, C. Jouanin, and D. Cassagne, "Optical and Confinement Properties of Two-Dimensional Photonic Crystals," *IEEE J. Lightwave Technol.*, vol. 17, pp. 2063-2077, 1999.
- [38] T. F. Krauss, B. Vögele, C. R. Stanley, and R. M. De La Rue, "Waveguide Microcavity Based on Photonic Microstructures," *IEEE Photon. Technol. Lett.*, vol. 9, pp. 176-178, 1997.
- [39] C. Ciminelli, F. Peluso, M. N. Armenise, and R. M. De La Rue, "Variable Oblique Incidence for Tunability in a Two-Dimensional Photonic-Crystal Guided-Wave Filter," *IEEE J. Lightwave Technol.*, vol. 24, pp. 470-476, 2006.

- [40] J. Zimmerman, M. Kamp, R. Schwertberger, J. P. Reithmaier, A. Forschel and R. März, "Efficient Light Transmission Through InP-Based Photonic Crystal Waveguides," *Electron. Lett.*, vol. 38, pp. 178-180, 2002.
- [41] A. Talneau, L. le Gouezigou, N. Bouadma, M. Kafesaki, C. M. Soukoulis, and M. Agio, "Photonic-Crystal Ultrashort Bends With Improved Transmission and Low Reflection at 1.55  $\mu\text{m}$ ," *Appl. Phys. Lett.*, vol. 80, pp. 547-549, 2002.
- [42] V. N. Astratov, R. M. Stevenson, I. S. Culshaw, D. M. Whittaker, M. S. Skolnick, T. F. Krauss and R. M. De La Rue, "Heavy Photon Dispersions in Photonic Crystal Waveguides," *Appl. Phys. Lett.* vol. 77, pp. 178-180, 2000.
- [43] C. J. M. Smith, H. Benisty, S. Olivier, M. Rattier, C. Weisbuch, T. F. Krauss, R. M. De La Rue, R. Houdré, U. Oesterle, "Low-Loss Channel Waveguides with Two-Dimensional Photonic Crystal Boundaries," *Appl. Phys. Lett.* vol. 77, pp. 2813-2815, 2000.
- [44] C. J. M. Smith, R. M. De La Rue, M. Rattier, S. Olivier, H. Benisty, C. Weisbuch, T. F. Krauss, R. Houdré, U. Oesterle, "Coupled Guide and Cavity in a Two-Dimensional Photonic Crystal Boundaries," *Appl. Phys. Lett.* vol. 78, pp. 1487-1489, 2001.
- [45] Y. A. Vlasov and S. J. McNab, "Losses in Single-Mode Silicon-On-Insulator Strip Waveguides and Bends," *Opt. Express*, vol. 12, pp. 1622-1631, 2004.
- [46] C. Angulo Barrios, V. R. de Almeida, and M. Lipson, "Low-Power-Consumption Short-Length and High-Modulation-Depth Silicon Electrooptic Modulator," *IEEE J. Lightwave Technol.*, vol. 21, pp. 1089-1098, 2003.
- [47] C. Angulo Barrios, V. R. Almeida, R. Panepucci, and M. Lipson, "Electrooptic Modulation of Silicon-on-Insulator Submicrometer-Size Waveguide Devices," *IEEE J. Lightwave Technol.*, vol. 21, pp. 2332-2339, 2003.
- [48] M. Lipson, "Guiding, Modulating and Emitting Light on Silicon – Challenges and Opportunities," *IEEE J. Lightwave Technol.*, vol. 23, pp. 4222-4238, 2005.
- [49] C. Manolatau and M. Lipson, "All-Optical Silicon Modulators Based on Carrier Injection by Two-Photon Absorption," *IEEE J. Lightwave Technol.*, vol. 24, pp. 1433-1439, 2006.
- [50] P. Dumon, W. Bogaerts, V. Wiaux, J. Wouters, S. Beckx, J. van Campenhout, D. Taillert, B. Luyssaert, P. Bienstman, D. van Thourhout, and R. Baets, "Low-Loss SOI Photonic Wires and Ring Resonators Fabricated With Deep UV Lithography," *IEEE Photon. Technol. Lett.*, vol. 16, pp. 1328-1330, 2004.
- [51] D. Marris, L. Vivien, D. Pascal, M. Rouvière, E. Cassan, A. Lupu, S. Laval, J. M. Fédéli, and L. El Melhaoui, "Ultralow Loss Successive Divisions Using Silicon-On-Insulator Microwaveguides," *Appl. Phys. Lett.*, vol. 87, pp. 211102:1-211102:3, 2005.

- [52] D. van Thourhout, P. Dumon, W. Bogaerts, G. Roelkens, D. Taillert, G. Priem, and R. Baets, "Recent Progress in SOI Nanophotonic Waveguides," *Proc. ECOC 2005.*, vol. 2, pp. 241-244, 2005.
- [53] R. S. Jacobsen, K. N. Andersen, P. I Borel, J. Fage-Pedersen, L. H. Frandsen, O. Hansen, M. Kristensen, A. V. Lavrinenko, G. Moulin, H. Ou, C. Peucheret, B. Zsigri and A. Bjarklev, "Strained Silicon as a New Electro-Optic Material, *Nature*, vol. 441, pp. 199-202, 2006.
- [54] R. A. Soref and B. R. Bennett, "Electrooptical Effects in Silicon," *IEEE J. Quant. Electron.*, vol. QE-23, pp. 123-129, 1987.
- [55] V. P. Tzolov and M. Fontaine, "A Passive Polarisation Converter Free of Longitudinally-Periodic Structure," *Opt. Comm.*, vol. 127, pp. 7-13, 1996.
- [56] J. Z. Huang, R Scarmozzino, G. Nagy, M.J. Steel and R. M. Osgood Jr., "Realization of a Compact and Single-Mode Optical Passive Polarization Converter," *IEEE Photon. Technol. Lett.*, vol. 12, pp. 317-319, 2000.
- [57] Y. Shani, R. Alferness, T. Koch, U. Koren, M. Oron, B. I. Miller and M. G. Young, "Polarization Rotation in Asymmetric Periodic Loaded Rib Waveguides," *Appl. Phys. Lett.* Vol. 59, pp. 1278-1280, 1991.
- [58] H. Heidrich, P. Albrecht, M. Hamacher, H.-P. Nolting, H. Schroeter-Janßen and C. M. Weinert, "Passive Mode Converter with a Periodically Tilted InP/GaInAsP Rib Waveguide," *IEEE Photon. Technol. Lett.*, vol. 4, pp. 34-36, 1992.
- [59] J. J. G. M. van der Tol, F. Hakimzadeh, J. W. Pedersen, D. Li, and H. van Brug, "A New Short and Low-Loss Passive Polarization Converter on InP," *IEEE Photon. Technol. Lett.*, vol. 7, pp. 32-34, 1995.
- [60] J. J. G. M. van der Tol, J. W. Pedersen, E. G. Metaal, F. Hakimzadeh, Y. S. Oei, F. H. Groen and I. Moerman, "Realization of a Short Integrated Optic Passive Polarization Converter," *IEEE Photon. Technol. Lett.*, vol. 7, pp. 893-895, 1995.
- [61] N. Somasiri, B. M. A. Rahman and S. S. A. Obayya, "Fabrication Tolerance Study of a Compact Passive Polarization Rotator," *IEEE J. Lightwave Technol.*, vol. 20, pp. 751-757, 2002.
- [62] J. W. Pedersen, J. J. G. M. van der Tol, F. Hakimzadeh, E. G. Metaal, J. J. W. van Gaalen, Y. S. Oei, and F. H. Groen, "Wavelength Insensitive Compact Bimodal Polarisation Converter on InP," *Proc. ECOC 97.*, pp. 281-284, 1997.
- [63] J. J. G. M. van der Tol, J. W. Pedersen, F. Hakimzadeh, E. G. Metaal, J. J. W. van Gaalen, Y. S. Oei, and F. H. Groen, "New Approach to Polarization-Independent Optical Circuits: the Bimodal Polarisation Converter," *Proc. OFC '97.*, TuC5, pp. 9-11, 1997.
- [64] M. Fontaine and V. P. Tzolov, "Modeling of a Passive Polarization Converter Free of Longitudinally-Periodic Structure," *Proc. IPR*, pp. 193-196, 1996.

- [65] C. van Dam, L. H. Spiekman, F. P. G. M. van Ham, F. H. Groen, J. J. G. M. van der Tol, I. Moerman, W. W. Pascher, M. Hamacher, H. Heidrich, C. M. Weinert and M. K. Smit, "Novel Compact Polarization Converters Based on Ultra Short Bends," *IEEE Photon. Technol. Lett.*, vol. 8, pp. 1346-1348, 1996.
- [66] W. W. Lui, T. Hirono, K. Yokoyama and W-P Huang, "Polarization Rotation in Semiconductor Bending Waveguides: A Coupled-Mode Theory Formulation," *IEEE J. Lightwave Technol.*, vol. 16, pp. 929-936, 1998.
- [67] S. S. A. Obayya, B. M. A. Rahman, K. T. V. Grattan and H. A. El-Mikati, "Beam Propagation Modeling of Polarization Rotation in Deeply Etched Semiconductor Bent Waveguides," *IEEE Photon. Technol. Lett.*, vol. 13, pp. 681-683, 2001.
- [68] K. Yamanouchi, K. Wakazono, and K. Shibayama, "Optical Surface Mode Converters and Modulators Utilizing Static Strain-Optic Effects," *IEEE J. Quant. Electron.*, vol. QE-16, pp. 628-634, 1980.
- [69] K. Takada and S. Mitachi, "Polarization Crosstalk Dependence on Length in Silica-Based Waveguides Measured by Using Optical Low Coherence Interference," *IEEE J. Lightwave Technol.*, vol. 16, pp. 1413-1422, 1998.
- [70] K. Takada, Y. Hida and S. Mitachi, "Growth of Polarization Crosstalk along a Silica-Based Optical Waveguide," *Electron. Lett.*, vol. 34, pp. 176-178, 1998.
- [71] K. Takada and S. Mitachi, "Measurement of Depolarization Ratio and Ultimate Limit of Polarization Crosstalk in Silica-Based Waveguides by Using a POLCR," *IEEE J. Lightwave Technol.*, vol. 16, pp. 639-645, 1998.
- [72] B. M. A. Rahman, S. S. A. Obayya and H. A. El-Mikati, "Minimisation of Modal Birefringence in Semiconductor Optical Guided-Wave Devices," *IEE Proc.-Optoelectron.*, vol. 147, pp. 151-156, 2000.
- [73] X. Zhao, C. Li and Y. Z. Xu, "Stress-Induced Birefringence Control in Optical Planar Waveguides," *Opt. Lett.*, vol. 28, pp. 564-566, 2003.
- [74] J. Buus, J. Haes, and R. Baets, "Analytical Study of Birefringence in Slab Waveguides," *Proc. IPR*, pp. 418-421, 1996.
- [75] B. M. A. Rahman, N. Somasiri, and M. Windmann, "Polarization Crosstalk in High Index Contrast Planar Silica Waveguides," *IEEE Photon. Technol. Lett.*, vol. 14, pp. 1109-1111, 2002.
- [76] N. Somasiri and B. M. A. Rahman, "Polarization Crosstalk in High Index Contrast Planar Silica Waveguides with Slanted Sidewalls," *IEEE J. Lightwave Technol.*, vol. 21, pp. 54-60, 2003.
- [77] A. R. Vellekoop and M. K. Smit, "Low-Loss Planar Optical Polarisation Splitter with Small Dimensions," *Electron. Lett.*, vol. 25, pp. 946-947, 1989.

- [78] L. B. Soldano, A. H. de Vreede, M. K. Smit, B. H. Verbeek, E. G. Metaal and F. H. Groen, "Mach-Zehnder Interferometer Polarization Splitter in InGaAsP/InP," *IEEE Photon. Technol. Lett.*, vol. 6, pp. 402-405, 1994.
- [79] M. H. Hu, J. Z. Huang, R. Scarmozzino, M. Levy and R. M. Osgood, Jr., "Tunable Mach-Zehnder Polarisation Splitter Using Height-Tapered Y-Branched," *IEEE Photon. Technol. Lett.*, vol. 9, pp. 773-775, 1997.
- [80] H. Yanagawa, H. Mak, Y. Kamata, and K Ueki, "High Extinction Guided-Wave Optical Polarization Splitter," *IEEE Photon. Technol. Lett.*, vol. 3, pp. 17-18, 1991.
- [81] M. Levy, R. M. Osgood, Jr., H. Hegde, F. J. Cadieu, R. Wolfe and V. J. Fratello, "Integrated Optical Isolators with Sputter Deposited Thin-Film Magnets," *IEEE Photon. Technol. Lett.*, vol. 8, pp. 903-905, 1996.
- [82] B. M. A. Rahman, S. S. A. Obayya, W. Boothittanont, and J. M. Heaton, "Novel Polarization-Maintaining Semiconductor Waveguide," *IEEE Photon. Technol. Lett.*, vol. 16, pp. 807-809, 2004.
- [83] N. Chi, S. Yu, L. Xu, and P. Jappesen, "Generation of a Polarization Shift Keying Signal and Its Application in Optical Labelling," *Proc. ECOC 2005.*, vol. 1, pp. 101-102, 2005.
- [84] R. C. Alferness, "Electrooptic Guided-Wave Device for General Polarization Transformations," *IEEE J. Quant. Electron.*, vol. QE-17, pp. 965-969, 1981.
- [85] N. Yu. Gordeev, K. J. Gordon, and G. S. Buller, "Tunable Electro-Optic Polarization Modulator for Quantum Key Distribution Applications," *Opt. Commun.*, vol. 234, pp. 203-210, 2004.
- [86] M. Schlak, C. M. Weinert, P. Albrecht, and H. -P. Nolting, "Tunable TE/TM-Mode Converter on (001)-InP-Substrate," *IEEE Photon. Technol. Lett.*, vol. 3, pp. 15-16, 1991.
- [87] N. Grossard, H. Porte, J.-P. Vilcot, Bruno Béche and J.-P. Goedgebuer, "AlGaAs-GaAs Polarization Converter with Phase Mismatch Control," *IEEE Photon. Technol. Lett.*, vol. 13, pp. 830-832, 2001.
- [88] F. Rahmatian, N. A. F. Jaeger, R. James, and E. Berolo, "An Ultrahigh-Speed Polarization Converter Using Slow-Wave Coplanar Electrodes," *IEEE Photon. Technol. Lett.*, vol. 10, pp. 675-677, 1998.
- [89] R. Spickermann, M. G. Peters and N. Dagli, "A Polarization Independent GaAs-AlGaAs Electrooptic Modulator," *IEEE J. Quant. Electron.*, vol. 32, pp. 764-769, 1996.
- [90] R. Hooke, "Micrographia," Royal Society, 1665 (Project Gutenberg, 2005).
- [91] C. Huygens, "Treatise on Light," 1690 (Project Gutenberg 2005).
- [92] R. M. A. Azzam and N. M. Bashara, "Ellipsometry and Polarized Light," 5<sup>th</sup> impression, Elsevier North Holland, 2003.
- [93] M. Born and E. Wolf, "Principles of Optics," 6<sup>th</sup> edition, Pergamon Press, 1980.

- [94] After J. H. Poincaré, "Théorie Mathématique de la Lumière," vol. II, Gauthiers-Villars, 1892, in Azzam and Bashara [92].
- [95] After J. Kepler, "Dioptrice," 1611, in Hecht [96].
- [96] E. Hecht, "Optics," 2<sup>nd</sup> edition, Addison Wesley, 1987.
- [97] A. Yariv, "Optical Electronics in Modern Communications," 5<sup>th</sup> edition, Oxford University Press, 1997.
- [98] A. B. Buckman, "Guided-Wave Photonics," Saunders College Publishing, 1992.
- [99] K. Okamoto, "Fundamentals of Optical Waveguides," Academic Press, 2000.
- [100] W. J. Duffin, "Electricity and Magnetism," 4<sup>th</sup> edition, McGraw-Hill, 1990.
- [101] K. S. Chiang, "Review of Numerical and Approximate Methods for the Modal Analysis of General Optical Dielectric Waveguides," *Opt. Quantum. Electron.*, vol. 26, pp. S113-S134, 1994.
- [102] M. A. Afromowitz, "Refractive Index of  $\text{Ga}_{1-x}\text{Al}_x\text{As}$ ," *Solid State Commun.* vol. 15, pp. 59-63, 1974.
- [103] S. Adachi, "GaAs, AlAs and  $\text{Al}_x\text{Ga}_{1-x}\text{As}$ : Material Parameters For Use in Research and Device Applications," *J. Appl. Phys.* vol. 58, pp. R1-R29, 1985.
- [104] S. Adachi, "Optical Properties of  $\text{Al}_x\text{Ga}_{1-x}\text{As}$  Alloys," *Phys Rev. B.* vol. 38, pp. 12345-12352, 1988.
- [105] S. Gehrsitz, F. K. Reinhart, C. Gourgon, N. Herres, A. Volanthen and H. Sigg, "The Refractive Index of  $\text{Al}_x\text{Ga}_{1-x}\text{As}$  Below the Band Gap: Accurate Determination and Empirical Modelling," *J. Appl. Phys.*, vol. 87, pp. 7825-7837, 2000.
- [106] "Properties of Gallium Arsenide," 2<sup>nd</sup> edition, Inspec, 1990.
- [107] J. M. Heaton, M. M. Bourke, S. B. Jones, B. H. Smith, K. P. Hilton, G. W. Smith, J. C. H. Birbeck, G. Berry, S. V. Dewar and D. R. Wight, "Optimisation of Deep-Etched, Single-Mode GaAs/AlGaAs Optical Waveguides Using Controlled Leakage into the Substrate," *J. Lightwave Technol.*, vol. 17, pp. 267-281, 1999.
- [108] M. Heiblum, W. I. Wang, L. E. Osterling, and V. Deline, "Heavy Doping of GaAs and AlGaAs with Silicon by Molecular Beam Epitaxy," *J. Appl. Phys.*, vol. 54, pp. 6751-6753, 1983.
- [109] B. J. Baliga, R. Ehle, A. Sears, P. Campbell, W. Garwacki, and W. Katz, "Breakdown Stability of Gold, Aluminium, and Tungsten Schottky Barriers on Gallium Arsenide," *IEEE Electron Device. Lett.*, vol. EDL-3, pp. 177-179, 1982.
- [110] Working Group I, COST 216, "Comparison of Different Modelling Techniques for Longitudinally Invariant Integrated Optical Waveguides," *IEE Proc.*, vol. 136, Pt. J, pp. 273-280, 1989.
- [111] M. W. Austin, "Theoretical and Experimental Investigation of GaAs/AlGaAs and  $n/n^+$  GaAs Rib Waveguides," *IEEE J. Lightwave Technol.*, vol. LT-2, pp. 688-692, 1984.

- [112] A. Kumar, D. F. Clark, and B. Culshaw, "Explanation of Errors Inherent in the Effective-Index Method for Analyzing Rectangular-Core Waveguides," *Opt. Lett.*, vol. 13, pp. 1129-1131, 1988.
- [113] P. W. A. McIlroy, M. S. Stern and P. C. Kendall, "Spectral Index Method for Polarized Modes in Semiconductor Rib Waveguides," *J. Lightwave Technol.*, vol. 8, pp. 113-117, 1990.
- [114] G. M. Berry, S. V. Burke, J. M. Heaton and D. R. Wight, "Analysis of Multilayer Semiconductor Rib Waveguides With High Refractive Index Substrates," *Electron. Lett.*, vol. 29, pp. 1941-1942, 1993.
- [115] A. S. Sudbø, "Improved Formulation of the Film Mode Matching Method for Mode Field Calculations in Dielectric Waveguides," *Pure Appl. Opt.*, vol. 3, pp. 381-388, 1994.
- [116] B. M. A. Rahman and J. B. Davies, "Finite-Element Solution of Integrated Optical Waveguides," *J. Lightwave Technol.*, vol. LT-2, pp. 682-688, 1984.
- [117] S. S. A. Obayya, B. M. A. Rahman, K. T. V. Grattan and H. A. El-Mikati, "Full Vectorial Finite-Element-Based Imaginary Distance Beam Propagation Solution of Complex Modes in Optical Waveguides," *IEEE J. Lightwave Technol.*, vol. 20, pp. 1054-1060, 2002.
- [118] F. A. Katsriku, B. M. A. Rahman, and K. T. V. Grattan, "Finite-Element Analysis of Second-Harmonic Generation in AlGaAs Waveguides," *IEEE J. Quant. Electron.*, vol. 36, pp. 282-289, 2000.
- [119] A. Yariv, "Coupled-Mode Theory for Guided-Wave Optics," *IEEE J. Quant. Electron.*, vol. QE9, pp. 919-933, 1973.
- [120] J. F. Nye, "Physical Properties of Crystals," Oxford University Press, 1957.
- [121] E. A. Wood, "Crystal Orientation Manual," Columbia University Press, 1963.
- [122] A. Y. Cho, "Film Deposition by Molecular-Beam Techniques," *J. Vac. Sci. Technol.*, vol. 8, pp. S31-S38, 1971.
- [123] A. Y. Cho, "Recent Developments in Molecular Beam Epitaxy," *J. Vac. Sci. Technol.*, vol. 16, pp. 275-284, 1979.
- [124] T. J. Drummond, W. G. Lyons, R. Fischer, R. E. Thorne, H. Morkoç, C. G. Hopkins, and C. A. Evans Jr., "Si Incorporation in  $\text{Al}_x\text{Ga}_{1-x}\text{As}$  Grown by Molecular Beam Epitaxy," *J. Vac. Sci. Technol.*, vol. 21, pp. 957-960, 1982.
- [125] R. F. K. Herzog and F. P. Viehböck, "Ion Source for Mass Spectrography," *Phys. Rev.* vol. 76, pp. 855-856, 1949.
- [126] W. K. Huber, H. Selhofer and A. Benninghoven, "An Analytical System for Secondary Ion Mass Spectrometry in Ultra High Vacuum," *J. Vac. Sci. Technol.*, vol. 9, pp. 482-486, 1972.



- [127] Y. Homma and Y. Ishii, "Surface Sputtering Rate Reduction and its Effect on SIMS Depth Profiling in Cesium-Ion-Bombarded GaAs," *J. Vac. Sci. Technol. A*, vol. 3, pp. 351-355, 1985.
- [128] V. R. Deline, W. Katz, C. A. Evans, Jr., and P. Williams, "Mechanism of the SIMS Matrix Effect," *Appl. Phys. Lett.*, vol. 33, pp. 832-835, 1978.
- [129] A. J. Simons, private communication.
- [130] R. G. Walker, "Simple and accurate loss measurement technique for semiconductor optical waveguides," *Electron. Lett.*, vol. 21, pp. 581-583, 1985 (erratum: vol. 21, pp. 714).
- [131] A. Kuver, J. M. Heaton, A. Miller, G. Murdoch, Y. Zhou, P. Jiang, and D. R. Wight, "Development of GaAs Electro-Optic Modulators with Improved Linearity," *Proc. EMRS DTC Tech. Conf.*, A22, 2005.
- [132] F. R. Laughton, PhD Thesis, 1991.
- [133] F. Heismann, D. A. Gray, B. H. Lee, and R. W. Smith, "Electrooptic Polarization Scramblers for Optically Amplified Long-Haul Transmission Systems," *IEEE Photon. Technol. Lett.*, vol. 6, pp. 1156-1158, 1994.
- [134] J. P. van der Ziel and A. C. Gossard, "Absorption, Refractive Index, and Birefringence of AlAs-GaAs Monolayers," *J. Appl. Phys.*, vol. 48, pp. 3018-3023, 1977.
- [135] J. B. D. Soole, C. Caneau, H. P. LeBlanc, N. C. Andreakis, A. Rajhel, C. Youtsey, and I. Adesida, "Suppression of Modal Birefringence in InP-InGaAsP Waveguides Through Use of Compensated Tensile Strain," *IEEE Photon. Technol. Lett.*, vol. 9, pp. 61-63, 1997.
- [136] J. Faist, F.-K. Reinhart, D. Martin, and E. Tuncel, "Orientation Dependence of the Phase Modulation in a p-n Junction GaAs/Al<sub>x</sub>Ga<sub>1-x</sub>As Waveguide," *Appl. Phys. Lett.*, vol. 50, pp. 68-70, 1987.
- [137] A. Hernández-Cabrera, C. Tejedor, and F. Meseguer, "Linear Electro-Optic Effects in Zinc Blende Semiconductors," *J. Appl. Phys.*, vol. 58, pp. 4666-4669, 1985.
- [138] S. Adachi and K. Oe, "Linear Electro-Optic Effects in Zincblende-Type Semiconductors: Key Properties of InGaAsP Relevant to Device Design," *J. Appl. Phys.*, vol. 56, pp. 74-80, 1984.
- [139] C.-A. Berseth, C. Wuethrich, and F. K. Reinhart, "The Electro-Optic Coefficients of GaAs: Measurements at 1.32 and 1.52  $\mu\text{m}$  and Study of their Dispersion Between 0.9 and 10  $\mu\text{m}$ ," *J. Appl. Phys.*, vol. 71, pp. 2821-2825, 1992.
- [140] N. Suzuki and K. Tada, "Elastooptic and Electrooptic Properties of GaAs," *Jpn. J. Appl. Phys.*, vol. 23, pp. 1011-1016, 1984.
- [141] M. Sugie and K. Tada, "Measurements of the Linear Electrooptic Coefficients and Analysis of the Nonlinear Susceptibilities in Cubic GaAs and Hexagonal CdS," *Jpn. J. Appl. Phys.*, vol. 15, pp. 421-431, 1976.

- [142] J. Faist and F.-K. Reinhart, "Phase Modulation in GaAs/AlGaAs Double Heterostructures. I. Theory," *J. Appl. Phys.*, vol. 67, pp. 6998-7005, 1990.
- [143] J. Faist and F.-K. Reinhart, "Phase Modulation in GaAs/AlGaAs Double Heterostructures. II. Experiment," *J. Appl. Phys.*, vol. 67, pp. 7006-7012, 1990.
- [144] S. Adachi, "Dispersion of the Linear Electro-Optic Coefficients in GaAs," *J. Appl. Phys.*, vol. 72, pp. 3702-3704, 1992.
- [145] M. P. van Exter, A. K. Jansen van Doorn and J. P. Woerdman, "Electro-Optic Effect and Birefringence in Semiconductor Vertical-Cavity Lasers," *Phys. Rev. A*, vol. 56, pp. 845-853, 1997.
- [146] J. G. Mendoza-Alvarez, L. A. Coldren, A. Alping, R. H. Yan, T. Hausken, K. Lee, and K. Pedrotti, "Analysis of Depletion Edge Translation Lightwave Modulators," *IEEE J. Lightwave Technol.*, vol. 6, pp. 793-808, 1988.
- [147] N. Chand, T. D. Harris, S. N. G. Chu, E. E. Becker, A. M. Sergent, M. Schnoes and D. V. Lang, "Variation of Impurities in  $\text{Al}_x\text{Ga}_{1-x}\text{As}$  ( $0.3 \leq x \leq 0.4$ ) With Growth Temperature: Implications for Device Leakage Current and Surface/Heterointerface Roughness," *J. Crystal Growth*, vol. 111, pp. 20-25, 1991.
- [148] S. S. Lee, R. V. Ramaswamy, and V. S. Sundaram, "Analysis and Design of High-Speed High-Efficiency GaAs-AlGaAs Double-Heterostructure Waveguide Phase Modulator," *IEEE J. Quant. Electron.*, vol. 27, pp. 726-736, 1991.
- [149] J. P. van der Ziel, M. Ilegems, and R. M. Mikulyak, "Optical Birefringence of Thin GaAs-AlAs Multilayer Films," *Appl. Phys. Lett.*, vol. 28, pp. 735-737, 1976.
- [150] P. Yeh, A. Yariv, and C.-S. Hong, "Electromagnetic Propagation in Periodic Stratified Media. I. General Theory," *J. Opt. Soc. Am.*, vol. 67, pp. 423-438, 1977.
- [151] A. Yariv and P. Yeh, "Electromagnetic Propagation in Periodic Stratified Media. II. Birefringence, Phase Matching, and X-ray Lasers," *J. Opt. Soc. Am.*, vol. 67, pp. 438-448, 1977.
- [152] M. Kumar, J. T. Boyd, H. E. Jackson, and B. L. Weiss, "Birefringent Properties of GaAlAs Multiple Quantum Well Planar Optical Waveguides," *IEEE J. Quant. Electron.*, vol. 28, pp. 1678-1688, 1997.
- [153] H. R. Khazaei, E. Berolo, and F. Ghannouchi, "High-Speed Slow-Wave Coplanar Strip GaAs/AlGaAs Electro-Optic Laser Modulator," *Microwave Opt. Technol. Lett.*, vol. 19, pp. 184-186, 1998.
- [154] S. Lovisa, N. Bouché, H. Helmers, Y. Heymes, F. Brillouet, Y. Gottesman, and K. Rao, "Integrated Laser Mach-Zehnder Modulator on Indium Phosphide Free of Modulated-Feedback," *IEEE Photon. Technol. Lett.*, vol. 13, pp. 1295-1297, 2001.

- [155] M. Kondow, T. Kitatani, S. Nakatsuka, M. C. Larson, K. Nakahara, Y. Yazawa, M. Okai, and K. Uomi, "GaInNAs : A Novel Material for Long-Wavelength Semiconductor Lasers," *IEEE J. Select. Topics Quant. Electron.*, vol. 3, pp. 719-730, 1997.
- [156] M. Fischer, D. Gollub, M. Reinhardt, and A. Forschel, "GaInAsN Based Lasers for the 1.3 and 1.5  $\mu\text{m}$  Wavelength Range," *Proc. IPRM*, pp. 101-104, 2001.
- [157] J. Kontinnen, P. Tuomisto, M. Guina, and M. Pessa, "Recent Progress in Development of GaInNAs-Based Photonic Devices," *Proc. ICTON*, pp. 189-192, 2006.
- [158] K. Koyama, J. Hashimoto, Y. Tsuji, T. Katsuyama, and A. Ishida, "1.3  $\mu\text{m}$  Optical Encoder/Correlators on GaAs-based Photonic Integrated Circuits," *Proc. ECOC 2005*, vol. 2, pp. 235-236, 2005.
- [159] C. H. Henry, L. F. Johnson, R. A. Logan, and D. P. Clarke, "Determination of the Refractive Index of InGaAsP Layers by Mode Line Luminescence Spectroscopy," *IEEE J. Quant. Electron.*, vol. QE-21, pp. 1887-1892, 1985.

